Mathematical Modeling of Regulatory Mechanisms in Cell Differentiation, Signaling, and Tumor Progression Across Biological Systems

A Dissertation Presented for the

Doctor of Philosophy

Degree

The University of Tennessee, Knoxville

Ziyi Liu

December 2024

DEDICATION

To my cute and loving parents, Weihong Lu and Wenbin Liu, and my dear grandfather, Xinyou Liu.

ACKNOWLEDGEMENTS

First and foremost, I would like to thank my advisor, Dr. Tian Hong, for his invaluable mentorship, encouragement, and guidance throughout my research journey. I am also deeply grateful to the members of my thesis committee, Dr. Maitreyi Das, Dr. Hong Guo, and Dr. Tarek Hewezi, for their constructive feedback and support, which greatly enriched this work.

I would like to express my heartfelt appreciation to everyone who contributed, directly or indirectly, to the successful completion of my PhD journey and this thesis.

ABSTRACT

Gene, protein and their regulators govern cellular and organismal responses to internal and external signals, coordinating essential processes that drive growth, differentiation, and adaptation. By mapping interactions among genes, regulatory networks provide a structured framework to simplify complex biological systems, enabling the analysis and prediction of cellular behaviors across diverse domains, revealing potential underlying principles common across different systems. This thesis employs regulatory network models to investigate fundamental mechanisms in three biological contexts. Although the core genes and molecules differ across each biological system, they are simplified to ‘nodes’ and ‘interactions among nodes’ within the regulatory network, whose dynamics can be calculated through differential equations. These node dynamics, linked to real biological insights and experimental approaches, reveal hidden mechanisms beyond what is directly observable.

In the shoot apical meristem (SAM) project (Chapter II), we developed a mathematical model to examine the regulatory network controlling stem cell populations, focusing on the interaction between WUSCHEL (WUS) and CLAVATA3 (CLV3), with modulation by Epidermal Patterning Factor-Like (EPFL) proteins. The model reveals that EPFL and HAIRY MERISTEM signals synergize to stabilize WUS expression under perturbations, providing insight into the SAM's apical-basal and lateral axis patterning.

In fission yeast project (Chapter III), we investigated Cdc42-mediated polarized growth, showing how alternating positive and negative feedbacks regulate growth cycles. Through experimental and modeling approaches, we found that endocytosis-dependent removal of Pak1 kinase is essential for Cdc42 reactivation, revealing a novel feedback mechanism involving branched actin-mediated endocytosis in the maintenance of cell polarity.

In small cell lung cancer (SCLC) project (Chapter IV), we used an ordinary differential equation framework to model the dynamics among key subtypes defined by ASCL1, NEUROD1, and YAP1. Our model captures subtype-specific expression patterns and predicts stable intermediate states, consistent with transcriptome data. This work provides a map of SCLC subtype dynamics, offering insights into the mechanisms driving tumor heterogeneity and progression.

Together, these studies highlight the utility of regulatory networks and dynamic modeling help to understand phenomena in complex biological systems.

TABLE OF CONTENTS

LIST OF TABLES

LIST OF FIGURES

INTRODUCTION

Understanding cellular behaviors and organismal functions requires more than examining individual genes or proteins in isolation; it involves studying interactions among these elements in both temporal and spatial dimensions within complex systems[1,2]. This led to the development of regulatory networks—frameworks that map these interactions to capture the collective dynamics of biological systems[3,4]. By organizing molecular interactions into networks, researchers can model how cellular processes such as growth, differentiation and boundary formation, and adaptation emerge from coordinated responses[5,6]. Regulatory networks have become essential tools in systems biology to simplify complex biological systems by linking mathematical frameworks with intrinsic features, they enable summarization and prediction in biological contexts under various conditions, including those that cannot yet be replicated experimentally, while allowing for the exclusion of certain details[7,8]. A vast unknown space exists regarding the connection between mathematical frameworks and biological processes, sparking my interest in exploring the depth and utility of this connection in understanding the mechanisms underlying various phenomena, as well as any potential limitations of these tools. Regulatory networks represent biological elements as nodes connected by edges (**Fig. 1**). These interactions may be promotive, enhancing the activity of downstream elements, or repressive, reducing or inhibiting their function. This balance of promotion and repression allows networks to maintain cellular stability and adapt to changes. Ordinary differential equations (ODE), partial differential equations (PDE), and Boolean modeling are applied based on regulatory network. Here, we focus on using ODE and PDE models to conduct temporal and spatial analyses of biological systems[9].

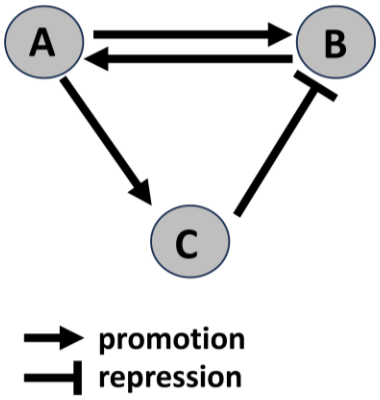

$$\frac{dA}{dt} = k_A \frac{B}{K_{BA} + B} - \delta_A A$$

$$\frac{dB}{dt} = k_B \frac{A}{K_{AB} + A} \frac{K_{CB}}{K_{CB} + C} - \delta_B B$$

$$\frac{dC}{dt} = k_C \frac{A}{K_{AC} + A} - \delta_C C$$

Figure 1.A simple regulatory network
Nodes A, B, and C represent genes, proteins, RNAs, or other regulatory elements, with the binding process details among these elements omitted. The ordinary differential equations on the right of the network depict interactions without cooperativity. k_A, k_B, k_C: maximum production rate coefficient, K_{BA}, K_{AB}, K_{CB} and K_{AC}: concentration producing half occupation, δ_A, δ_B, and δ_C: degradation rate coefficient.

One prominent example is pattern formation, as seen in the development of Turing patterns[10], where reaction-diffusion systems modeled by PDEs reveal how spatial patterns, such as stripes or spots, can emerge from simple regulatory interactions. These models are also applied in agent-based models to simulate cell populations and spatial interactions[11], enabling predictions of emergent patterns in tissue development. Another key application is in modeling oscillatory dynamics. Complex cellular processes, such as circadian rhythms or cell cycle regulation, often exhibit oscillations that arise from nonlinear interactions, time delays, and sometimes noise-induced fluctuations[12]. Using models based on the networks of core genes constructed from biological systems, researchers can analyze how feedback loops in regulatory networks produce sustained oscillations, and the conditions for certain dynamics on period and spatial aspects, providing insights into the stability and robustness of these cycles under various conditions. Nongenetic heterogeneity and cell fate decisions are fundamental phenomena in biology[13], seen

in processes like cell differentiation and cancer progression[14]. Despite their diversity, they are connected to inherent features of ODEs, such as multi-stability[15], where cells can maintain multiple stable fates through feedback loops and nonlinear interactions. While modeling provides a structured approach to distill core phenomena from biological data, revealing potential mechanisms and enabling predictions, much remains unknown about how complex interactions drive diverse cellular behaviors, especially in response to untested, unobservable, or dynamic conditions. Here, we built models on three specific biological systems, each serving as an example of pattern formation in tissue development, oscillatory systems, and nongenetic heterogeneity.

Pattern formation in tissue development

Pattern formation is a process in developmental biology, referring to the emergence of ordered structures and spatial organization within tissues from initially uniform or undifferentiated cell populations[16]. Patterns in biological systems can be periodic structures, gradients, or regions with distinct cellular identities and functions. This spatial organization is critical for tissue function and integrity, as seen in the arrangement of hair follicles, leaf veins, or cellular layers in organs. In developmental systems, pattern formation is often driven by regulatory networks that process biochemical signals, providing cells with positional information[17]. A key theoretical framework explaining these phenomena is Turing's reaction-diffusion model, which posits that interacting molecules, known as morphogens, can create stable spatial patterns through combinations of local activation and long-range inhibition[10,18]. These patterns arise from simple regulatory interactions and can drive complex, self-organizing behaviors in cells and tissues, forming distinct zones of high and low concentrations that define spatial structures. Example includes the stripes in zebra, round dots and lines with different colors on butterfly wings, and the finger

formation in an embryo. Additionally, agent-based models provide insights at the cellular level, simulating individual cells and whole populations by applying regulatory networks to calculate protein and RNA levels in each cell.

A notable instance of pattern formation in plants occurs within the shoot apical meristem (SAM), a stem cell niche responsible for generating new tissues such as flowers and leaves in the shoot[19]. The SAM's organized structure is maintained through a regulatory network involving feedback interactions between key genes, such as WUSCHEL (WUS) and CLAVATA3 (CLV3), The interaction between them that WUS promotes the CLV3 expression and CLV3 repress WUS expression balances stem cell renewal and differentiation[20]. WUS which repress the differentiation of the stem cells is localized in the organizing zone, and CLV3 which is a ligand and important in the cell-cell communication even in long distance, is localized in the central zone. However, it's not enough to understand the SAM pattern formation because the WUS-CLV3 is contributed vertically but the peripheral direction isn't regulated. ERECTA family (ERf) are receptors for leaf initiation and it was found repressing the WUS and CLV3 expressions to restrict the SAM size in the peripheral direction[21]. Mathematical models have provided quantitative insights into gene activity dynamics, deepening our understanding of the complex molecular and cellular networks that regulate SAM patterning [22-33]. These models have highlighted the importance of negative feedback in sustaining homeostasis and clarified the mechanisms that separate CLV3 and WUS expression domains. However, its not clear how SAM integrates information from the apical-basal direction with that from the lateral direction. In Chapter II, we present a 2D computational model reveals how different signals contribute to the SAM pattern and predict the SAM pattern in mutants.

Oscillatory systems

Oscillatory systems govern a wide range of population, cellular, and physiological processes in biology, all of which rely on precise temporal dynamics. These rhythmic behaviors emerge from tightly regulated networks of interacting individuals or components, often sustained through feedback loops that drive regular cycles of activation and repression[34]. While the underlying reasons and advantages of these rhythmic behaviors are not fully understood, such dynamics enable cells and organisms to respond to environmental cues, synchronize complex behaviors, and control timing-sensitive events, such as cell division, circadian rhythms, and developmental processes[35]. For example, in the cell cycle, certain proteins like cyclins oscillate in a regular pattern, controlling cell growth and division by guiding the cell through each stage in the correct order[36]. At the population level, predator-prey interactions represent another form of oscillation, where species interactions lead to cyclical fluctuations in their populations, often modeled with differential equations like the Lotka-Volterra equations[37]. These oscillations stem from intrinsic properties of differential equations in mathematical modeling, where nonlinear interactions and feedback loops generate sustained cycles essential to understanding complex biological behaviors.

At the cellular level, a significant challenge in studying oscillatory systems is understanding how rhythmic cellular behaviors are sustained and regulated across varying conditions. In many biological contexts, it remains unclear how sensitive these oscillations are to perturbations such as temperature and the structural integrity of actin, which can disrupt processes like cell cycle progression or cellular polarization[38]. Using fission yeast as a model provides an advantage in addressing these challenges, as its simpler, well-characterized regulatory networks allow researchers to systematically explore the mechanics of oscillation with fewer confounding

factors[39]. Fission yeast grows in a bipolar manner, with the major regulator of cell polarization, the GTPase Cdc42, showing anti-correlated activity levels between the two cell tips[40]. This bipolar dynamic is disrupted when F-actin is disrupted in Latrunculin A (Lat-A) condition[41]. The activation of Cdc42 is mediated by the guanine nucleotide exchange factor (GEF) Scd1 and its scaffold protein Scd2, while Pak1 kinase mediates the repression of active Cdc42 at the tips[40,42,43]. However, it remains unclear how Cdc42 activation cycles back to the cell ends. Therefore, in Chapter III, we develop a PDE model to simulate the dynamics of active Cdc42 and its regulators, incorporating actin patch interruptions, in collaboration with experimental data from our collaborators.

Nongenetic heterogeneity

Nongenetic heterogeneity refers to the diversity of cellular behaviors and characteristics within a genetically identical population, arising from factors like fluctuations in gene expression, protein levels, and local environmental conditions rather than genetic differences[13]. This variability enables cells to adopt distinct phenotypes, allowing populations to better adapt to dynamic environments[44]. For example, in cancer, nongenetic heterogeneity permits subpopulations of tumor cells to survive treatments, contributing to drug resistance and relapse[45,46]. In microbial populations, it enables survival under stress, where certain cells can enter a dormant state to endure adverse conditions[47]. However, a key challenge in studying nongenetic heterogeneity is understanding how stable yet flexible cellular states are maintained without genetic variation, especially as cells respond to changing environments. Capturing the complex interplay of molecular interactions and feedback loops that sustain these variable states, often through mathematical modeling, is difficult due to transient and unpredictable cellular behaviors. To address these challenges, advanced single-cell techniques, such as single-cell RNA sequencing

and live-cell imaging, have been developed to observe and quantify nongenetic variability in real time[48,49].

In small cell lung cancer (SCLC), nongenetic heterogeneity is particularly prominent and contributes to the aggressive nature and poor prognosis of the disease[50]. SCLC tumors display a mix of cell states, it characterized by significant heterogeneity marked by ASCL1, NEUROD1, POU2F3, and YAP1, including neuroendocrine (NE) and non-neuroendocrine (non-NE) phenotypes, which coexist within the same tumor[51-53]. This heterogeneity is thought to drive therapy resistance, as certain subpopulations may survive initial treatment and lead to relapse[54]. Despite advances in identifying NE and non-NE markers, key questions remain about the mechanisms underlying the maintenance of these phenotypic states and their transitions. It is unclear how SCLC cells dynamically switch between NE and non-NE states or how external signals, like therapeutic pressure, influence this plasticity. Additionally, the roles of regulatory networks and feedback loops in maintaining such heterogeneity within SCLC tumors are not fully understood. Boolean and ordinary differential equation (ODE) models built to explain heterogeneity often use highly complex networks with numerous nodes and signaling pathways, making them challenging to apply at a practical level[53,55,56] . Therefore, in Chapter IV, we simplified the regulatory network of SCLC and built ODE models to simulate the subtypes and their coexistence, integrating analyses of single-cell RNA sequencing (scRNA-seq) data[56].

References

1 Graur, D. *et al.* On the immortality of television sets: "function" in the human genome according to the evolution-free gospel of ENCODE. *Genome Biol Evol* **5**, 578-590 (2013). https://doi.org/10.1093/gbe/evt028

2 Pevsner, J. *Bioinformatics and functional genomics*. (Wiley-Blackwell, 2009).

3 Licatalosi, D. D. & Darnell, R. B. RNA processing and its regulation: global insights into biological networks. *Nat Rev Genet* **11**, 75-87 (2010). https://doi.org/10.1038/nrg2673

4 Barabasi, A. L. & Oltvai, Z. N. Network biology: understanding the cell's functional organization. *Nat Rev Genet* **5**, 101-113 (2004). https://doi.org/10.1038/nrg1272

5 Vercruysse, J., Baekelandt, A., Gonzalez, N. & Inze, D. Molecular networks regulating cell division during Arabidopsis leaf growth. *J Exp Bot* **71**, 2365-2378 (2020). https://doi.org/10.1093/jxb/erz522

6 Li, C. J. *et al.* MicroRNA governs bistable cell differentiation and lineage segregation via a noncanonical feedback. *Mol Syst Biol* **17**, e9945 (2021). https://doi.org/10.15252/msb.20209945

7 Milo, R. *et al.* Network motifs: simple building blocks of complex networks. *Science* **298**, 824-827 (2002). https://doi.org/10.1126/science.298.5594.824

8 Murray, J. D. Vignettes from the field of mathematical biology: the application of mathematics to biology and medicine. *Interface Focus* **2**, 397-406 (2012). https://doi.org/10.1098/rsfs.2011.0102

9 Ingalls, B. P. *Mathematical modeling in systems biology: an introduction*. (MIT press, 2013).

10 Turing, A. M. The chemical basis of morphogenesis. 1953. *Bull Math Biol* **52**, 153-197; discussion 119-152 (1990). https://doi.org/10.1007/BF02459572

11 Zhang, B. & DeAngelis, D. L. An overview of agent-based models in plant biology and ecology. *Ann Bot* **126**, 539-557 (2020). https://doi.org/10.1093/aob/mcaa043

12 Glass, L. & Pasternack, J. S. Stable oscillations in mathematical models of biological control systems. *Journal of Mathematical Biology* **6**, 207-223 (1978).

13 Huang, S. Non-genetic heterogeneity of cells in development: more than just noise. *Development* **136**, 3853-3862 (2009). https://doi.org/10.1242/dev.035139

14 Brock, A., Chang, H. & Huang, S. Non-genetic heterogeneity--a mutation-independent driving force for the somatic evolution of tumours. *Nat Rev Genet* **10**, 336-342 (2009). https://doi.org/10.1038/nrg2556

15 Laurent, M. & Kellershohn, N. Multistability: a major means of differentiation and evolution in biological systems. *Trends Biochem Sci* **24**, 418-422 (1999). https://doi.org/10.1016/s0968-0004(99)01473-5

16 Koch, A. J. & Meinhardt, H. Biological pattern formation: from basic mechanisms to complex structures. *Reviews of Modern Physics* **66**, 1481 (1994).

17 Jin, Y., Guo, H. & Meng, Y. A hierarchical gene regulatory network for adaptive multirobot pattern formation. *IEEE Trans Syst Man Cybern B Cybern* **42**, 805-816 (2012). https://doi.org/10.1109/TSMCB.2011.2178021

18 Gierer, A. & Meinhardt, H. A theory of biological pattern formation. *Kybernetik* **12**, 30-39 (1972). https://doi.org/10.1007/BF00289234

19 Carles, C. C. & Fletcher, J. C. Shoot apical meristem maintenance: the art of a dynamic balance. *Trends Plant Sci* **8**, 394-401 (2003). https://doi.org/10.1016/S1360-1385(03)00164-X

20 Barton, M. K. Twenty years on: the inner workings of the shoot apical meristem, a developmental dynamo. *Dev Biol* **341**, 95-113 (2010). https://doi.org/10.1016/j.ydbio.2009.11.029

21 Zhang, L., DeGennaro, D., Lin, G., Chai, J. & Shpak, E. D. ERECTA family signaling constrains CLAVATA3 and WUSCHEL to the center of the shoot apical meristem. *Development* **148** (2021). https://doi.org/10.1242/dev.189753

22 Yadav, R. K. *et al.* WUSCHEL protein movement mediates stem cell homeostasis in the Arabidopsis shoot apex. *Genes Dev* **25**, 2025-2030 (2011). https://doi.org/10.1101/gad.17258511

23 Zhou, Y. *et al.* HAIRY MERISTEM with WUSCHEL confines CLAVATA3 expression to the outer apical meristem layers. *Science* **361**, 502-506 (2018). https://doi.org/10.1126/science.aar8638

24 Jonsson, H. *et al.* Modeling the organization of the WUSCHEL expression domain in the shoot apical meristem. *Bioinformatics* **21 Suppl 1**, i232-240 (2005). https://doi.org/10.1093/bioinformatics/bti1036

25 Nikolaev, S. V., Penenko, A. V., Lavreha, V. V., Mjolsness, E. D. & Kolchanov, N. A. A model study of the role of proteins CLV1, CLV2, CLV3, and WUS in regulation of the structure of the shoot apical meristem. *Russian Journal of Developmental Biology* **38**, 383-388 (2007).

26 Hohm, T., Zitzler, E. & Simon, R. A dynamic model for stem cell homeostasis and patterning in Arabidopsis meristems. *PLoS One* **5**, e9189 (2010). https://doi.org/10.1371/journal.pone.0009189

27 Fujita, H., Toyokura, K., Okada, K. & Kawaguchi, M. Reaction-diffusion pattern in shoot apical meristem of plants. *PLoS One* **6**, e18243 (2011). https://doi.org/10.1371/journal.pone.0018243

28 Adibi, M., Yoshida, S., Weijers, D. & Fleck, C. Centering the Organizing Center in the Arabidopsis thaliana Shoot Apical Meristem by a Combination of Cytokinin Signaling and Self-Organization. *PLoS One* **11**, e0147830 (2016). https://doi.org/10.1371/journal.pone.0147830

29 Gruel, J. *et al.* An epidermis-driven mechanism positions and scales stem cell niches in plants. *Sci Adv* **2**, e1500989 (2016). https://doi.org/10.1126/sciadv.1500989

30 Gruel, J., Deichmann, J., Landrein, B., Hitchcock, T. & Jonsson, H. The interaction of transcription factors controls the spatial layout of plant aerial stem cell niches. *NPJ Syst Biol Appl* **4**, 36 (2018). https://doi.org/10.1038/s41540-018-0072-1

31 Banwarth-Kuhn, M. *et al.* Cell-Based Model of the Generation and Maintenance of the Shape and Structure of the Multilayered Shoot Apical Meristem of Arabidopsis thaliana. *Bull Math Biol* **81**, 3245-3281 (2019). https://doi.org/10.1007/s11538-018-00547-z

32 Klawe, F. Z. *et al.* Mathematical modeling of plant cell fate transitions controlled by hormonal signals. *PLoS Comput Biol* **16**, e1007523 (2020). https://doi.org/10.1371/journal.pcbi.1007523

33 Chickarmane, V. S., Gordon, S. P., Tarr, P. T., Heisler, M. G. & Meyerowitz, E. M. Cytokinin signaling as a positional cue for patterning the apical–basal axis of the growing

Arabidopsis shoot meristem. *Proceedings of the National Academy of Sciences* **109**, 4002-4007 (2012).

34 Tsai, T. Y. *et al.* Robust, tunable biological oscillations from interlinked positive and negative feedback loops. *Science* **321**, 126-129 (2008). https://doi.org/10.1126/science.1156951

35 Kruse, K. & Julicher, F. Oscillations in cell biology. *Curr Opin Cell Biol* **17**, 20-26 (2005). https://doi.org/10.1016/j.ceb.2004.12.007

36 Ferrell, J. E., Jr., Tsai, T. Y. & Yang, Q. Modeling the cell cycle: why do certain circuits oscillate? *Cell* **144**, 874-885 (2011). https://doi.org/10.1016/j.cell.2011.03.006

37 Berryman, A. A. The origins and evolution of predator-prey theory. *Ecology* **73**, 1530-1535 (1992).

38 Waliser, D. E., Lau, K. M. & Kim, J. H. The influence of coupled sea surface temperatures on the Madden–Julian oscillation: A model perturbation experiment. *Journal of the Atmospheric Sciences* **56**, 333-358 (1999).

39 Hayles, J. & Nurse, P. Introduction to Fission Yeast as a Model System. *Cold Spring Harb Protoc* **2018** (2018). https://doi.org/10.1101/pdb.top079749

40 Das, M. *et al.* Oscillatory dynamics of Cdc42 GTPase in the control of polarized growth. *Science* **337**, 239-243 (2012). https://doi.org/10.1126/science.1218377

41 Mutavchiev, D. R., Leda, M. & Sawin, K. E. Remodeling of the Fission Yeast Cdc42 Cell-Polarity Module via the Sty1 p38 Stress-Activated Protein Kinase Pathway. *Curr Biol* **26**, 2921-2928 (2016). https://doi.org/10.1016/j.cub.2016.08.048

42 Das, M. & Verde, F. Role of Cdc42 dynamics in the control of fission yeast cell polarization. *Biochem Soc Trans* **41**, 1745-1749 (2013). https://doi.org/10.1042/BST20130241

43 Howell, A. S. *et al.* Negative feedback enhances robustness in the yeast polarity establishment circuit. *Cell* **149**, 322-333 (2012). https://doi.org/10.1016/j.cell.2012.03.012

44 Loewer, A. & Lahav, G. We are all individuals: causes and consequences of non-genetic heterogeneity in mammalian cells. *Curr Opin Genet Dev* **21**, 753-758 (2011). https://doi.org/10.1016/j.gde.2011.09.010

45 Inde, Z. & Dixon, S. J. The impact of non-genetic heterogeneity on cancer cell death. *Crit Rev Biochem Mol Biol* **53**, 99-114 (2018). https://doi.org/10.1080/10409238.2017.1412395

46 Reiter, J. G. *et al.* An analysis of genetic heterogeneity in untreated cancers. *Nat Rev Cancer* **19**, 639-650 (2019). https://doi.org/10.1038/s41568-019-0185-x

47 Avery, S. V. Microbial cell individuality and the underlying sources of heterogeneity. *Nat Rev Microbiol* **4**, 577-587 (2006). https://doi.org/10.1038/nrmicro1460

48 Kolodziejczyk, A. A., Kim, J. K., Svensson, V., Marioni, J. C. & Teichmann, S. A. The technology and biology of single-cell RNA sequencing. *Mol Cell* **58**, 610-620 (2015). https://doi.org/10.1016/j.molcel.2015.04.005

49 Tanimura, A., Nezu, A. & Morita, T. [Light microscopy techniques for live cell and animal imaging using fluorescent proteins]. *Nihon Yakurigaku Zasshi* **141**, 262-267 (2013). https://doi.org/10.1254/fpj.141.262

50 Rudin, C. M., Brambilla, E., Faivre-Finn, C. & Sage, J. Small-cell lung cancer. *Nat Rev Dis Primers* **7**, 3 (2021). https://doi.org/10.1038/s41572-020-00235-0

51 Schwendenwein, A. *et al.* Molecular profiles of small cell lung cancer subtypes: Therapeutic implications. *Molecular Therapy - Oncolytics* **20**, 470-483 (2021). https://doi.org/10.1016/j.omto.2021.02.004

52 Rudin, C. M. *et al.* Molecular subtypes of small cell lung cancer: a synthesis of human and mouse model data. *Nat Rev Cancer* **19**, 289-297 (2019). https://doi.org/10.1038/s41568-019-0133-9

53 Wooten, D. J. *et al.* Systems-level network modeling of Small Cell Lung Cancer subtypes identifies master regulators and destabilizers. *PLoS Comput Biol* **15**, e1007343 (2019). https://doi.org/10.1371/journal.pcbi.1007343

54 Sabari, J. K., Lok, B. H., Laird, J. H., Poirier, J. T. & Rudin, C. M. Unravelling the biology of SCLC: implications for therapy. *Nat Rev Clin Oncol* **14**, 549-561 (2017). https://doi.org/10.1038/nrclinonc.2017.71

55 Chauhan, L., Ram, U., Hari, K. & Jolly, M. K. Topological signatures in regulatory network enable phenotypic heterogeneity in small cell lung cancer. *Elife* **10** (2021). https://doi.org/10.7554/eLife.64522

56 Ireland, A. S. *et al.* MYC Drives Temporal Evolution of Small Cell Lung Cancer Subtypes by Reprogramming Neuroendocrine Fate. *Cancer Cell* **38**, 60-78 e12 (2020). https://doi.org/10.1016/j.ccell.2020.05.001

CHAPTER II

A MATHEMATICL MODEL FOR UNDERSTANDING SYNERGISTIC REGULATIONS AND PARADOXICAL FEEDBACKS IN THE SHOOT APICAL MERISTEM

This chapter is based on the article published below:

Liu Z, Shpak ED, Hong T. A mathematical model for understanding synergistic regulations and paradoxical feedbacks in the shoot apical meristem. *Comput Struct Biotechnol J* 2020, 18:1878. The full text is available at https://www.csbj.org/article/S2001-0370(20)30484-0/fulltext.

I conducted the investigation, developed the methodology, created visualizations, and was responsible for writing the original draft as well as reviewing and editing the manuscript.

Abstract

The shoot apical meristem (SAM) is the primary stem cell niche in plant shoots. Stem cells in the SAM are controlled by an intricate regulatory network, including negative feedback between WUSCHEL (WUS) and CLAVATA3 (CLV3). Recently, we identified a group of signals, Epidermal Patterning Factor-Like (EPFL) proteins, that are produced at the peripheral region and are important for SAM homeostasis. Here, we present a mathematical model for the SAM regulatory network. The model revealed that the SAM uses EPFL and signals such as HAIRY MERISTEM from the middle in a synergistic manner to constrain both *WUS* and *CLV3*. We found that interconnected negative and positive feedbacks between WUS and CLV3 ensure stable *WUS* expression in the SAM when facing perturbations, and the positive feedback loop also maintains distinct cell populations containing WUS^{on} and $CLV3^{on}$ cells in the apical-basal direction. Furthermore, systematic perturbations of the parameters revealed a tradeoff between optimizations of multiple patterning features. Our results provide a holistic view of the regulation of SAM patterning in multiple dimensions. They give insights into how *Arabidopsis* integrates signals from lateral and apical-basal axes to control the SAM patterning, and they shed light into design principles that may be widely useful for understanding regulatory networks of stem cell niche.

Introduction

Spatiotemporal regulation of cell populations in stem cell niches is critical for plants and animals during developmental and homeostatic conditions [1-5]. The shoot apical meristem (SAM) of Arabidopsis thaliana is one of the most extensively studied model systems for understanding stem cell niches in plants. The dome-shaped SAM harbors stem cells that are located in the epidermal and subepidermal layers. Under normal conditions these cells are characterized by the high expression of CLAVATA3 (CLV3), which encodes a secreted peptide that can diffuse to neighboring cells and regulate their gene expression [6]. The patterning and size of the SAM remain stable in mature plants, suggesting tight regulation of stem cell populations. Previous studies have revealed crucial mechanisms for regulating these cells in the apical-basal axis of the SAM. Particularly, the number of stem cells is maintained by WUSCHEL (WUS), which is expressed in cells of the organizing center below the subepidermal layers of the SAM [7]. WUS protein moves to the upper layers and activates CLV3 expression, whereas the diffusible CLV3 peptide suppresses the expression of WUS [8-10]. This negative feedback loop is considered the core circuit controlling the size of the SAM and the number of stem cells in this region [9,11,12]. More recent discoveries show that the separation of WUS and CLV3 expressing regions is driven by additional signals originating from the basal zones of the SAM, such as high concentrations of WUS and/or HAIRY MERISTEM (HAM) [12-14], and these signals prevent CLV3 expression below the subepidermal layer. Mathematical models have been used in numerous studies to describe the dynamics of gene activities in the SAM quantitatively, and have improved our understanding of the complex molecular and cellular networks controlling SAM patterning [12,15-24]. These models have revealed the key role of negative feedback in maintaining homeostasis, as well as the mechanisms underlying the separation between CLV3 and WUS expressing domains.

While these experimental and computational studies provided ample information about regulatory networks along the apical-basal axis, regulatory mechanisms in the lateral direction of the SAM remain unclear. the organizing center below the subepidermal layers of the SAM [7,25]. WUS protein moves to the upper layers and activates CLV3 expression, whereas the diffusible CLV3 peptide suppresses the expression of WUS [8-10]. This negative feedback loop is considered the core circuit controlling the size of the SAM and the number of stem cells in this region [8,9,11]. More recent discoveries show that the separation of WUS and CLV3 expressing regions is driven by additional signals originating from the basal zones of the SAM, such as high concentrations of WUS and/or HAIRY MERISTEM (HAM) [12-14], and these signals prevent CLV3 expression below the subepidermal layer. Mathematical models have been used in numerous studies to describe the dynamics of gene activities in the SAM quantitatively, and have improved our understanding of the complex molecular and cellular networks controlling SAM patterning [10,12,16-20,22-24,26,27]. These models have revealed the key role of negative feedback in maintaining homeostasis, as well as the mechanisms underlying the separation between CLV3 and WUS expressing domains. While these experimental and computational studies provided ample information about regulatory networks along the apical-basal axis, regulatory mechanisms in the lateral direction of the SAM remain unclear.

Recently, we have identified a group of potent signals, Epidermal Patterning Factor-Like (EPFL) proteins, that originate from the peripheral zone of SAM and inhibit CLV3 and WUS expression [22,28,29]. EPFL signals are communicated by four diffusive ligands: EPFL1, EPFL2, EPFL4, and EPFL6 [28]. The loss of these ligands caused the upregulation of both WUS and CLV3 and increased the size of the SAM, suggesting that these signals play an essential role in maintaining the stem cell population in the SAM, and their perturbation can override the negative feedback

loop [29]. However, it is unclear how the SAM integrates information from the apical-basal direction with that from the lateral direction, and how multiple signals synergistically control SAM patterning.

To obtain insights into these questions, we built a mathematical model describing the intracellular and intercellular regulatory networks in the meristem. We perturbed the model to examine the key regulatory elements (e.g. EPFL and HAM) controlling the gene expression patterns in the middle and peripheral regions of the SAM, and to unravel the roles of interconnected negative and positive feedbacks between WUS and CLV3 in SAM patterning. We further used three new metrics of patterning to explore functional objectives that may constraint the kinetic rate constants underlying regulations of key genes: 1) downregulation of WUS expression in the lateral region of the SAM; 2) stability of total WUS concentration in the SAM in the presence of perturbations; and 3) diverse cell populations that highly express either WUS or CLV3 in the middle of the SAM. These analyses provide a holistic view of the principles governing the SAM patterning.

Results

A mathematical model recapitulates known phenotypes of SAM patterning under normal and perturbed conditions

Previous mathematical models of SAM patterning have been focused on the negative feedback between WUS and CLV3, as well as other factors controlling their expressions along the apical-basal axis [10,12,16-19,22-24,26,27]. Here, we built a two-dimensional model incorporating elements of these previous models with the potent lateral regulator EPFL that was recently characterized (**Fig. 2A**) [28,29]. We considered 51 cells (a minimum number of cells that reflects multilayer patterning of the SAM in terms of key factors [12]) organized in a dome-shaped structure. This

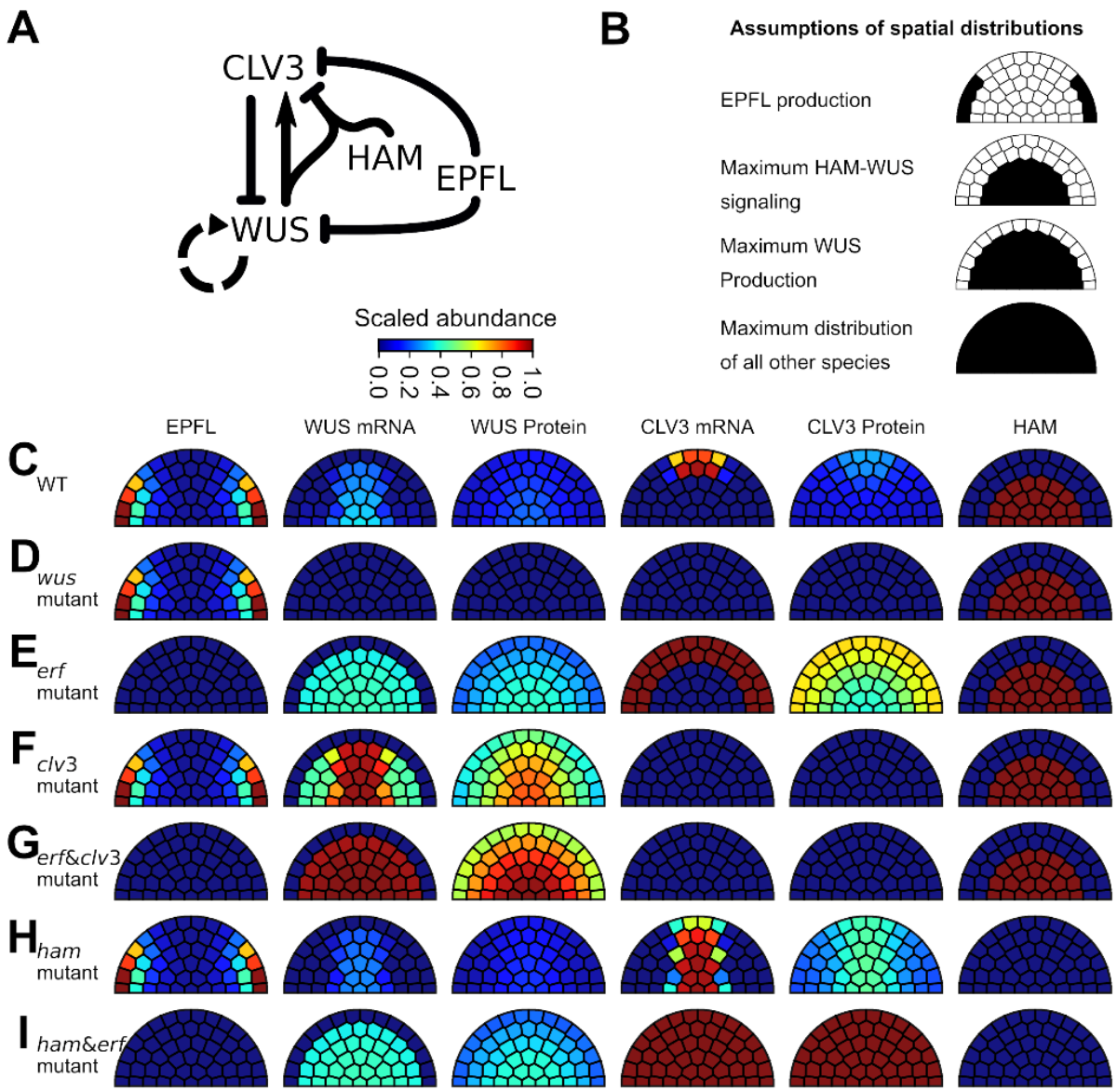

Figure 2. A mathematical model of SAM captures roles of key regulators of SAM patterning. A. Influence diagram for key molecules regulating SAM patterning. ARR and cytokinin were implicitly modeled (WUS activates itself in the model). A single variable was used to describe the combined signaling of WUS and HAM. Arrows indicate experimentally supported regulations (Table 1). B. Key assumptions about spatial distribution of SAM regulators. Black regions highlight cells that were assumed to have the capacity to produce the denoted molecules. Maximum signaling/distribution/production refers to the distributions of denoted production or signaling in the absence of inhibitors and in the presence of activators. EPFL, CLV3 and WUS proteins were allowed to move between neighboring cells. C-J. Steady state distributions of SAM regulators under various conditions. All mutants were simulated by removing the production of the denoted molecules. All simulations were performed under initial conditions with low amount (=0) of all molecules across SAM.

structure contains six layers of cells (L1-L6) for which gene expression patterning is critical for development [12,13]. In each cell, concentrations of six interacting molecules were described with ordinary differential equations (ODEs) based on the gene regulatory network shown in **Fig. 1A** (see Methods for details). Key assumptions about the regions producing the regulatory molecules are illustrated in **Fig. 1B** (See Methods and **Table 1** for details). Our assumptions also include diffusion/movement of EPFL, WUS and CLV3 in all directions. We sought to obtain a comprehensive view of gene regulation in SAM patterning by simulating and analyzing this model under various conditions.

We first fit our model to SAM patterning under normal conditions (wild type, WT) as well as several phenotypes in terms of distributions of key molecules due to genetic perturbations of several regulators. We identified a representative parameter set that allows the model to reproduce experimentally observed phenotypes (**Fig. 2C–I**, **Table 2**).

In the simulated wild type, WUS and CLV3 were expressed in confined regions near the central axis of the SAM, while their proteins diffused (CLV3) or moved (WUS) broadly to other regions (**Fig. 2C**). Along the apical-basal axis, a moderate amount of WUS moved to L1 layer, where it maintained the expression of CLV3. Similarly, a moderate amount of CLV3 diffused to the meristem rib (**Fig. 1C**). Notably, both WUS and CLV3 expressing regions are limited by lateral boundaries, whereas their expressions in the apical-basal direction are anticorrelated with each other, with the L1 layer expressing CLV3 but not WUS, and bottom layers only expressing WUS (**Fig. 2C**). EPFL was distributed differentially within and across layers, due to the assumption of its isotropic diffusion, and this established a lateral-middle spatial gradient (**Fig. 2C**). In the wus mutant, no CLV3 expression was observed as we expected from the gene regulatory network (**Fig. 2A and D**) [19,22,30,31]. The lateral confinement of both WUS and CLV3 was lost upon the

Table 1. Key assumptions of the model.

Assumption	Reference for experimental evidence
Ligands EPFL are produced in the lateral region of the SAM, but are diffused broadly in the SAM	[28]
EPFL inhibits *CLV3* and *WUS* expression	[29]
CLV3 inhibits *WUS* expression, and WUS activates *CLV3* expression	[8-10]
WUS activates its own expression (for example: an ARR-Cytokinin-*WUS* loop)	[22,32-34]
HAM inhibits CLV3 expression	[12]
HAM and WUS synergize to exert transcriptional regulation	[12,35]
HAM is expressed in the lower middle region of the SAM	[12]
WUS may be expressed broadly in the SAM, except for L1 layer	[8,9]
CLV3 may be expressed broadly in the SAM	[9,12,36,37]
WUS and CLV3 move/diffuse to neighboring cells in the SAM	[10,37,38]

***** The phrase 'may be expressed' is used when the model allows the expression, but it is inhibited by relevant inhibitors when they are present.

Table 2. Known SAM gene expression patterns captured by the model.

Genetic background	Description of patterning	Reference for experimental evidence
Wild type	*CLV3* is expressed in the top middle region of the SAM	[6,31,37,39]
Wild type	*WUS* is expressed in the lower middle region of the SAM	[6,8,9,39]
wus mutant	No *CLV3* expression	[30,31]
clv3 mutant	Increased *WUS* expression in the SAM as compared to wild type, including lateral region	[8,36]
erf mutant	Increased *WUS* expression in the SAM as compared to wild type, including lateral region	[40]
erf mutant	Increased and broader *CLV3* expression as compared to wild type	[30,40]
clv3-erf mutant	Highly increased *WUS* expression as compared to wild type	[29,30]
ham mutant	*CLV3* expression is centered at in the lower middle region of the SAM	[12,41]
Induction of *CLV3* expression by 10-fold	Stable *WUS* expression pattern in the SAM	[42]

removal of signaling triggers by EPFL (**Fig. 2E**): WUS expression had a moderate lateral expansion, whereas CLV3 had a dramatic expansion in the epidermal (L1) layer and the L2 layer (note that the erf mutant in this study refers to the absence of multiple ERf receptors, which requires knocking outthree genes experimentally). These observations are consistent with recent experimental findings [30,40]. Interestingly, the model showed that the anticorrelation pattern of WUS and CLV3 expressions was largely maintained in this mutant despite their own expansions (**Fig. 1E**). The model reproduced the well- known phenotype of the CLV3 knockout (KO): the WUS expressing region expanded both apically and laterally upon the loss of CLV3 (**Fig. 1F**). Moreover, the expression in the meristem rib was increased from the level in the wildtype (**Fig. 1C and F**), indicating the inhibitory effect of CLV3 diffused to this region. The model showed that in the absence of both EPFL and CLV3 signals, WUS had a dramatic increase in expression across the SAM (**Fig. 1G**). The model also showed that the anticorrelated WUS-CLV3 expression pattern was lost in the absence of HAM (**Fig. 2H**), and this co-expression of WUS and CLV3 in the organizing center with HAM KO was observed previously [12,41]. Interestingly, there was a moderate decrease of CLV3 expression in the central zone with the loss of HAM compared to the wild type (**Fig. 2H**), even though the central zone CLV3 expression was not regulated by HAM directly in our model (see Methods). The decrease of CLV3 expression in the central zone was because of the negative feedback between WUS and CLV3: the moderately decreased WUS expression upon the expansion of CLV3 expression to the meristem rib reduced the availability of WUS protein in the central zone. This reduction in turn decreased the CLV3 expression in the central zone, but not in the meristem rib due to the dominant effect of the loss of HAM. The alteration of the CLV3 expression pattern in the ham mutant is consistent with a recent report [12]. Nonetheless, a significant level of WUS expression was maintained in the

meristem rib [41], and this level of WUS in the SAM was critical for the overall gene patterns in the region, as manifested in the phenotype upon the complete loss of WUS (**Fig. 1D**). In addition to these genetic perturbations, our model recapitulated the observed stability of the WUS expression when the CLV3 expression was increased by 10-fold [42] (**Fig. S1A**). We summarized the key SAM expression patterns that are captured by the model and their supporting experimental evidence in **Table 2**. In conclusion, our model captures the effects of perturbations of key genes that regulate SAM patterning in both apical-basal and lateral directions.

The model makes an immediate prediction that the loss of HAM and EPFL will cause dramatic expansion of the CLV3-expressing region, as well as expansion of the WUS-expressing region in both the lateral and apical-basal axes (**Fig. 2I**). In the following sections, we describe specific insights and other predictions that we obtained from the model.

Differential roles of EPFLs and CLV3 in regulating SAM patterning

It has been previously shown that *WUS* expression in the middle SAM is essential for maintaining stem cell populations [7,43]. In contrast, *WUS* expression in the lateral region of the SAM is associated with abnormal development [9,30]. These observations suggest that the two regions may require different modes of regulation. To gain deeper understanding of the roles of EPFL and CLV3 in limiting the *WUS* expression region, we focused on two SAM areas described in the model (**Figure 3A**). Region 1 (**Figure 3A**, blue) includes cells near the middle apical-basal axis of the SAM, whereas Region 2 (**Figure 3A**, Indian red) includes cells in the peripheral zone. In terms of our simulation results (**Figure 2C**), Region 1 was defined as cells that express either *WUS* or *CLV3* under the wild-type condition, whereas Region 2 was defined as cells that neither express *WUS* nor *CLV3* under the same condition.

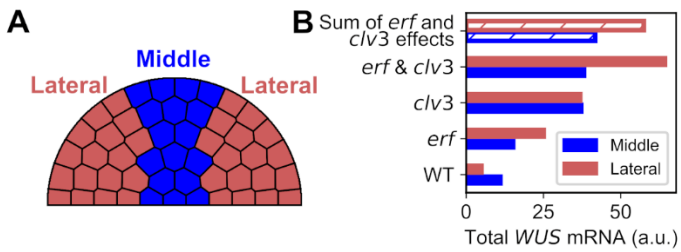

Figure 3. EPFL and CLV3 control patterns of WUS expression at different regions. A. An illustration of two regions that were analyzed for *WUS* mRNA production. Region 1 (blue) contains cells near the apical-basal axis of the SAM, whereas Region 2 (Indian red) contains cells at the lateral boundary between the middle zone and the peripheral zone. **B.** Total *WUS* mRNA in the two regions indicated in A. Simulations were performed with the model structure described in **Figure 1**. Mutant genotypes were modeled by removing the production of the indicated mRNAs. The hatched bars were calculated by adding the amounts of mRNA in the *erf* mutant and *clv3* mutant increased from wild type, and the amount of wild-type mRNA.

We quantified the amount of *WUS* mRNA (in an arbitrary unit, or a.u.) in these two areas based on our simulations. We found that upon the loss of EPFLs there was a moderate increase of total *WUS* expression near the middle apical-basal axis, but the increase was more prominent in the *clv3* mutant (**Figure 3B**, blue). This increase in the *clv3* mutant is comparable to that observed in the *erf-clv3* mutant, suggesting that the apical-basal boundary of the *WUS*-expressing zone is primarily controlled by CLV3. In contrast to the dominant role of CLV3 in Region 1, EPFL and CLV3 both control *WUS* expression in Region 2: the loss of either factor (single-mutants) resulted in a significant increase of *WUS* expression, and the loss of both factors produced an even more dramatic increase (**Figure 2B**, Indian red). Interestingly, the sum of the effects on *WUS* expression from the two single-mutants was less than the effect of the *erf-clv3* mutant (**Figure 3B**, hatched vs. solid), suggesting a nonlinear cooperativity between EPFL and CLV3 signals. We found that this cooperativity was maintained when we perturbed the parameter values in the model (**Figure S2**). Together with the observation that the loss of EPFL resulted in an increased CLV3 signal (**Figure 2E**), our model further suggests that part of the lost inhibition

of *WUS* expression in the *erf* mutant is compensated for by an increased level of CLV3. Together, these results show that EPFL and CLV3 signals

synergistically control the lateral boundary of the *WUS*-expressing zone, whereas the apical-basal boundary of the *WUS*-expressing zone is primarily controlled by the CLV3 signal. In addition to the synergy between

EPFL and CLV3 in the regulation of *WUS*, we found that the spatial distributions of the cells producing EPFL and HAM (**Figure S1B and C**) were critical for maintaining the expression patterns of both *WUS* and *CLV3*: the expansion of HAM production to upper layers resulted in the reduction of *CLV3* expression and the lateral expression of *WUS* expression; the expansion of EPFL to the middle SAM reduced the overall *CLV3* expression, and it dampened the *WUS* expression in the middle SAM while causing the lateral expansion of the *WUS* expression (**Figure S1B and C**). These results suggest the synergy between EPFL and HAM, and the importance of their spatial distributions.

Inhibition of *WUS* and *CLV3* expression by EPFL is important for maintaining SAM patterning

It was recently observed that EPFL inhibits the expression of both *WUS* and *CLV3* [29]. It was, however, unclear how each of these inhibitions contributes to SAM patterning. We therefore removed these two inhibitory relationships from our model one at a time and examined the steady state patterning of the SAM (**Figure 4**). We found that upon the loss of *CLV3* inhibition by EPFL, there was a 30% increase of both *CLV3* mRNA and CLV3 protein in the SAM. Interestingly, *CLV3* was expressed around the organizing center in both the apical and lateral directions (**Figure 4A and C**). This lateral expansion of *CLV3* expression suggests that the inhibition of *CLV3* by EPFL is critical for restricting *CLV3* expression in the top layers of the

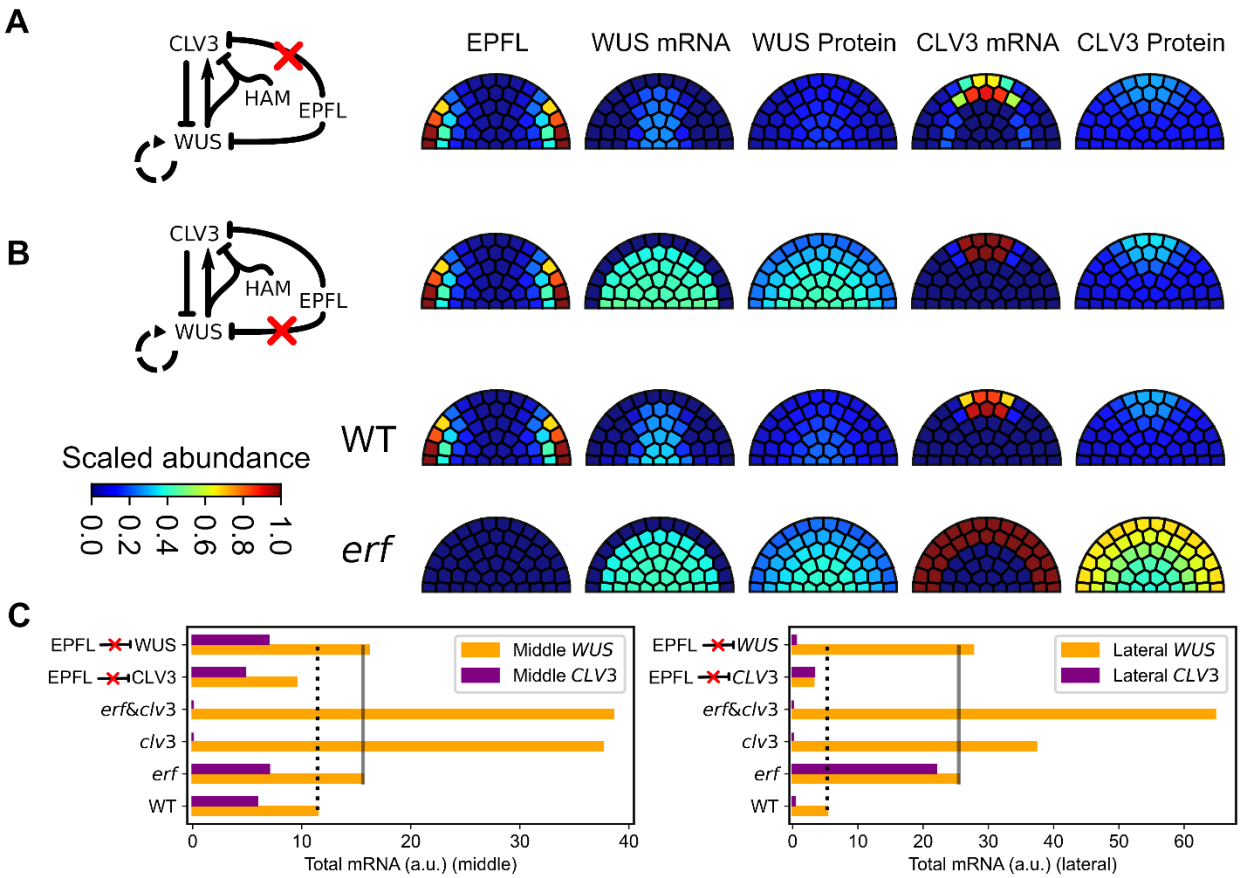

Figure 4. The effects of WUS and CLV3 inhibition by EPFL. A. A simulation with the removal of *CLV3* inhibition by EPFL. **B**. A simulation with the removal of *WUS* inhibition by EPFL. In both A and B, the indicated transcriptional inhibition was removed from the model by increasing the threshold to a large number (1000). Simulations were performed with the procedure as those described **in Figure** 1. Steady state SAM patterns were analyzed. Wild type and *erf* mutant patterning are shown for comparison. **C**. Left: *WUS* and *CLV3* mRNA in the middle region (**Figure 2**, blue). Right: *WUS* and *CLV3* mRNA in the lateral region (**Figure 2**, Indian red). Dotted lines are visual guides for wild-type *WUS* mRNA. Gray lines are visual guides for *erf* mutant *WUS* mRNA.

middle SAM. In addition, *WUS* expression moderately decreased compared to the wild type (**Figure 2C**) due to the expanded *CLV3* expression. When we removed the inhibition of *WUS* by EPFL, the *WUS* expression region had a significant lateral expansion, and its expression in the middle region also increased compared to the wild type (**Figure 4B and C**, dotted line). These analyses demonstrated the paradoxical roles of EPFL on *WUS* expression: it directly downregulates *WUS* in both the lateral and middle regions of the SAM while it indirectly upregulates the same gene by inhibiting *CLV3*. The direct downregulation has the dominant effect, because blocking this regulation produced a *WUS* pattern similar to that of the *erf* mutant (**Figure 3**, gray line). Nonetheless, the slightly higher *WUS* expression in the blocked EPFL-to-*WUS* condition than in the *erf* mutant provides further evidence for the paradoxical roles of EPFL (**Figure 4**, gray line). Together, these results show that EPFL inhibition of both *WUS* and *CLV3* is critical for SAM patterning. We found that the alterations of the gene expression upon perturbations were not always intuitive. For example, blocking the EPFL-to-*CLV3* inhibition resulted in a reduction of *CLV3* mRNA in the middle of the SAM (**Figure 4C**), suggesting the importance of the negative feedback loop between CLV3 and WUS. In the next section, we describe our analyses of the interconnected feedback loops in the SAM.

Paradoxical feedbacks between WUS and CLV3 maintain robust patterning in apical-basal axis of SAM

We noticed that the SAM regulatory network contains two feedback loops between WUS and CLV3 (**Figure 2A and Figure 5A**). In the first network motif, WUS activates *CLV3* expression and CLV3 inhibits *WUS* expression, forming a negative feedback loop. The second motif consists of *WUS* inhibition by CLV3, and *CLV3* inhibition by HAM and high concentration of WUS [12-14]. This motif is a double-negative (positive) feedback loop (**Figure 5A**, top panel).

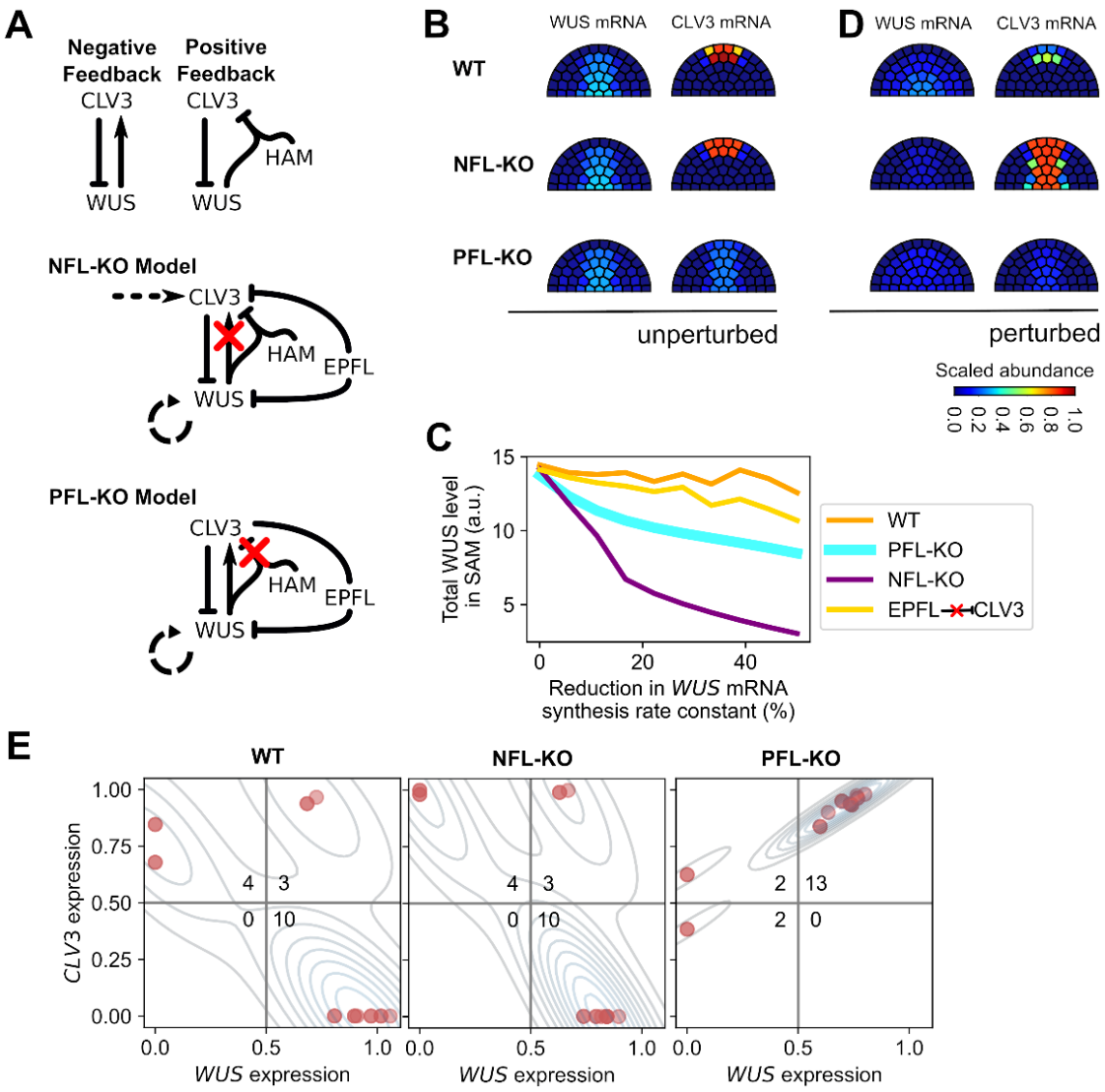

Figure 5. Roles of paradoxical feedbacks between WUS and CLV3. A. Top: two motifs showing the negative and the positive feedback between WUS and CLV3. Middle: network structure of negative feedback knockout model (NFL-KO) which does not have a WUS-CLV3 negative feedback loop. Dashed line indicates a hypothetical activation signal for maintaining CLV3. Bottom: network structure of positive feedback knockout model (PFL-KO) which does not have the WUS-CLV3 positive feedback loop. **B**. Steady state distributions of *WUS* and *CLV3* mRNA in SAM with circuits of wild-type, NFL-KO and PFL-KO models. **C**. Steady state distributions of *WUS* and *CLV3* mRNA in SAM with circuits of wild-type, NFL-KO and PFL-KO models with 50% reduction of *WUS* mRNA production rate constant. **D**. Total *WUS* mRNA in SAM with respect to reduction of *WUS* mRNA production rate constant. **E**. Distributions of 17 middle SAM cells in the phase space of *WUS* and *CLV3* mRNA with three models under normal condition. Each dot indicates a cell and in the middle region of the SAM (Figure 2.2A Indian red), and its coordinates show the levels of *WUS* mRNA and *CLV3* mRNA, respectively. Contour maps show the density of these cells in the *WUS* and *CLV3* mRNA space. Numbers in quadrants indicate cell numbers. The cell numbers in the top left and lower right quadrants reflect the diversity of the WUS^{on} and $CLV3^{on}$ cells.

These two feedback loops are both interconnected (i.e. they share a regulation) and paradoxical (i.e. they are negative and positive respectively). While the first loop is a well-known negative feedback that has been proposed to be critical for maintaining the homeostasis of the SAM, the function of the interconnected and paradoxical feedbacks between WUS and CLV3 is unclear. To examine the roles of these two feedbacks on SAM patterning, we constructed two alternative models with disrupted negative and positive feedbacks respectively (NFL-KO, PFL-KO models. **Figure 4A**). For NFL-KO model, we introduced a hypothetical activation signal for CLV3 in the L1 and L2 layers of the central zone. This signal avoids the trivial outcome of the complete absence of CLV3 in the SAM, and the addition of the signal gave rise to a SAM pattern similar to the wild type (**Figure 5B**). For the PFL-KO model, we removed the downregulation of *CLV3* by the WUS signal. In order to compare these alternative models to the basal (wild-type) model in terms of *WUS* expression patterning, we further adjusted the synthesis rate constants of *CLV3* mRNA in the alternative models such that the overall *WUS* expression patterns obtained with the three models are comparable (**Figure 5B**).

We next perturbed the expression of *WUS* by reducing its mRNA synthesis rate constant. This perturbation reflects possible aberrant environmental or genetic changes. Because the regulation of *WUS* itself was not altered in the PFL-KO or NFL-KO models, this perturbation was not biased towards any model in a trivial way. However, the wild type model was robust with respect to the perturbation in terms of total WUS production in the SAM (**Figure 5C**): a 50% decrease of the rate constant resulted in less than 10% loss of the *WUS* in the wild type SAM (**Figure 5C**, orange). In contrast, the loss of either negative or positive feedback decreased the stability of *WUS* production when challenged with the same perturbations. In particular, the NFL-KO model had a more prominent decrease of *WUS* production (> 3-fold from unperturbed condition) than

the PFL-KO model did **(Figure 5C**, purple), suggesting that the negative feedback has a dominant role in protecting the stability of *WUS* production in the SAM. In earlier analysis, we showed that blocking the inhibition of *CLV3* by EPFL gave rise to a *WUS* expression pattern comparable to the wild type (**Figure 4A**), a feature found in the NFL-KO and PFL-KO models. We observed that the inhibition of *CLV3* by EPFL also facilitates the maintenance of *WUS* expression stability, but its effect is less than that of the feedback loops (**Figure 5C**, yellow). We found that when the *WUS* mRNA production rate constant was reduced in the wild type, the level of *CLV3* expression was significantly decreased (**Figure 5D**), which in turn compensated for the loss of *WUS* mRNA production, thereby maintaining the stability of *WUS* expression in the SAM via a negative feedback. This compensation effect via downregulation of *CLV3* was not observed with the NFL-KO model, and was only moderate in the PFL-KO model as compared to the wild type model (**Figure 5D**). We further perturbed the system with increasing WUS production rate constant, and we used additional metrics to examine the response in terms of the SAM patterning. We found that the wild-type model consistently performed equally well as or better than the alternative models (**Figure S3**).

Positive feedback (or double-negative feedback) is widely used in developmental systems for maintaining tissue boundaries [29,44,45]. In the wild type SAM, cells along the middle apical-basal axis are either $WUS^{off}CLV3^{on}$ or $WUS^{on}CLV3^{off}$ except for L2 cells which had significant expression of both *WUS* and *CLV3* (**Figure 5B and E**). The robustness of the anticorrelated expression pattern of *WUS* and *CLV3* in most cells of the SAM was also reflected in mutant simulations when EPFL-driven inhibition was partially or completely lost (**Figures 2E, 3, and 5B**). However, in the absence of the positive feedback loop (**Figure 2.4A**, PFL-KO model), the number of cells co-expressing *WUS* and *CLV3* increased significantly, and the anticorrelation

pattern of *WUS* and *CLV3* expressions was lost (**Figure 5B and E**).

Together, these results show that the paradoxical feedbacks between WUS and CLV3 are critical both for stabilizing *WUS* expression and for generating the separation between *WUS*-expressing and *CLV3*-expressing regions. Stable *WUS* expression may be important for maintaining the size of the SAM, while separation between *WUS*-expressing and *CLV3*-expressing cells may be important for maintaining diverse cellular properties, such as proliferation rate, in different regions of the SAM. The specialization of cellular phenotypes along the apical basal axis may in turn support the robust structure of the SAM.

Tradeoff in maintaining SAM patterning

Due to the lack of quantitative measurement in terms of the SAM patterning, we did not attempt to obtain a single parameter set that gives the best fit to experimental data in this study. However, the emergence of the simulated SAM patterns that are qualitatively consistent with many experimental observations allows us to interrogate the influence of the parameter values on the SAM patterning in a collective manner. In the previous sections we discussed three key features of the SAM regulatory network: 1) the network uses two signals to fully repress *WUS* expression in the lateral region of the SAM; 2) the network maintains the stability of WUS production in the SAM using two feedback loops; and 3) the network generates a distinct population containing WUS^{on} cells and $CLV3^{on}$ cells in the middle region of the SAM. If these three features are critical for plant physiology, how would the kinetic rate constants of the system be optimized to achieve them? To gain insight into this question, we used three metrics describing three performance objectives: lowering *WUS* expression in the lateral region, lowering the variability of *WUS* production in the presence of perturbations, and increasing the number of WUS^{on} cells and $CLV3^{on}$ cells in the middle region (**Figure 6A**). For easier interpretation, all three metrics were

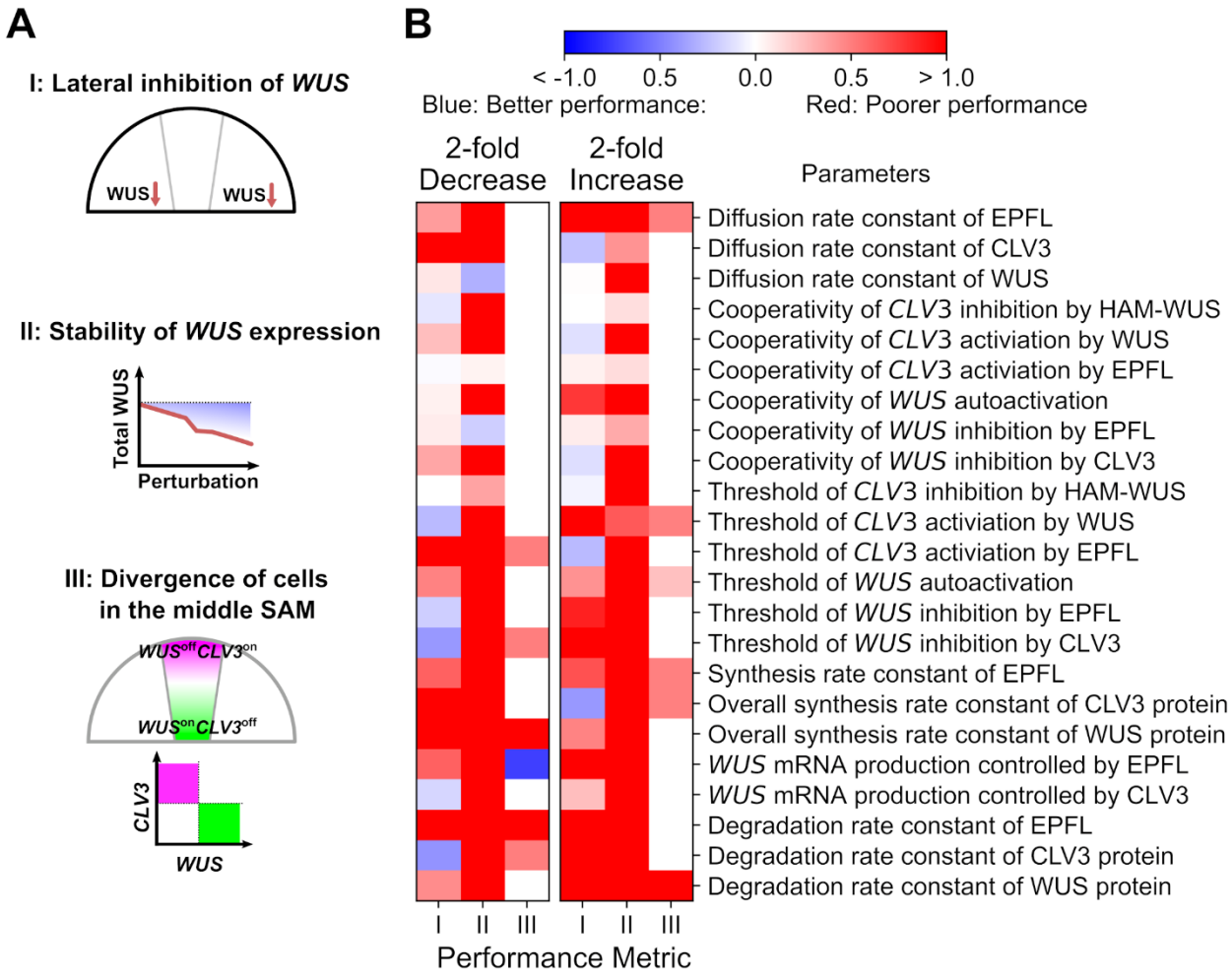

Figure 6. Influence of parametric changes on three performance objectives of SAM patterning. A. Illustrations of the three performance metrics of SAM patterning. See Methods for details of these metrics. **B**. The performance scores upon perturbations of 23 parameters. Each parameter was decreased and increased by 2-fold and simulation was performed in the same procedure as that with the wild-type (basal) model. Steady state SAM patterning was scored based on the three metrics, and the scores were compared with those obtained with basal model. Blue: perturbed model has better score than basal model does. Red: perturbed model has poorer score than basal model does. White: perturbed model and basal model have the same score.

designed such that lower scores mean 'better' performance and higher scores mean 'poorer' performance (see Methods, **Figure 6B** top). We perturbed 23 model parameters by decreasing each of them 2-fold, and then increasing each 2-fold, scored the performance of the perturbed models using the three performance metrics, and then normalized them to the scores obtained from wild type model (**Figure 6B**) by subtracting the wild-type scores from the scores of the

perturbed models (see Methods). Among the three metrics, the scores of the diversity metric (Metric III)

were most robust with respect to the perturbations among the three metrics, possibility because it is based on a discrete measurement in terms of cell numbers rather than a continuous one. Changes in each parameter had some influence on at least one performance score, and changes in 13 out of the 23 parameters had one performance score better than the basal one. However, none of the changes of individual parameters gave rise to better performance in two or three metrics (**Figure 6, heatmap, Figure S4**).

This analysis suggests a possible tradeoff in optimizing the kinetics of the SAM network: achieving better performance in one metric is likely accompanied with jeopardized performance in at least one other metric. However, this phenomenon might be simply due to the fact the very few perturbations of individual parameters had improved performance in any metric, so the absence of better performance in two or three metrics may just occur by chance. To further examine the relationship among these three performance objectives, we generated 10^4 perturbed models with all of their parameter values deviated from the basal set. These parameter values were randomly selected from intervals bounded by values with 50% changes from the basal set. Among these 10^4 randomly perturbed models, 1964 of them had improved performance score (< 0, or better-than-basal) for Metric I, 202 of them had improved score for Metric II and 423 of them had improved score for Metric III (**Figure 7A**). However, only 2 of them had improved scores for all three metrics. We performed a permutation test and confirmed that this number is significantly low (**Figure 7B**, upper panel, $p < 10^{-4}$). Furthermore, when a model had a better-than-basal score in one or more metric, the probability that it also had a lower-than-basal score in one or more metric was 99.8%, a number that is significantly higher than expected (**Figure 6B**,

lower panel, $p = 0.006$). These results show the there exists a tradeoff in optimizing the three performance objectives of SAM patterning. We then asked which pairs of metrics have a significant tradeoff problem when multiple kinetic rate constants are varied, and we found that if a model has a better score for Metric I or Metric II (lateral inhibition and stability), there is a significantly high probability that it has a poorer score for Metric III (divergence), suggesting that there is a pairwise tradeoff between optimizing for *WUS*-*CLV3* diversity and other features (**Figure 7C**). Other pairs of metrics did not show significantly high probability of having such opposite trends of performance change (**Figure 6C**). Overall, these results suggest that there may exist a tradeoff among the three objectives of the SAM patterning when the system varies its rate constants to achieve those goals simultaneously.

Discussion

Two-axis control of *WUS* expression in the SAM

Patterning of *WUS* and *CLV3* expression in the SAM is considered to be a crucial system for stem cell maintenance in plants. In this study, we built a multicellular model describing the key gene regulatory network controlling SAM patterning. In particular, we considered signals that regulate *WUS* expression from both the middle SAM and peripheral regions. This differs from previous models which focused on the middle SAM region around the apical-basal axis [10,12,15,16,23,24,27]. Our model shows how the system combines the peripheral signal EPFL with the

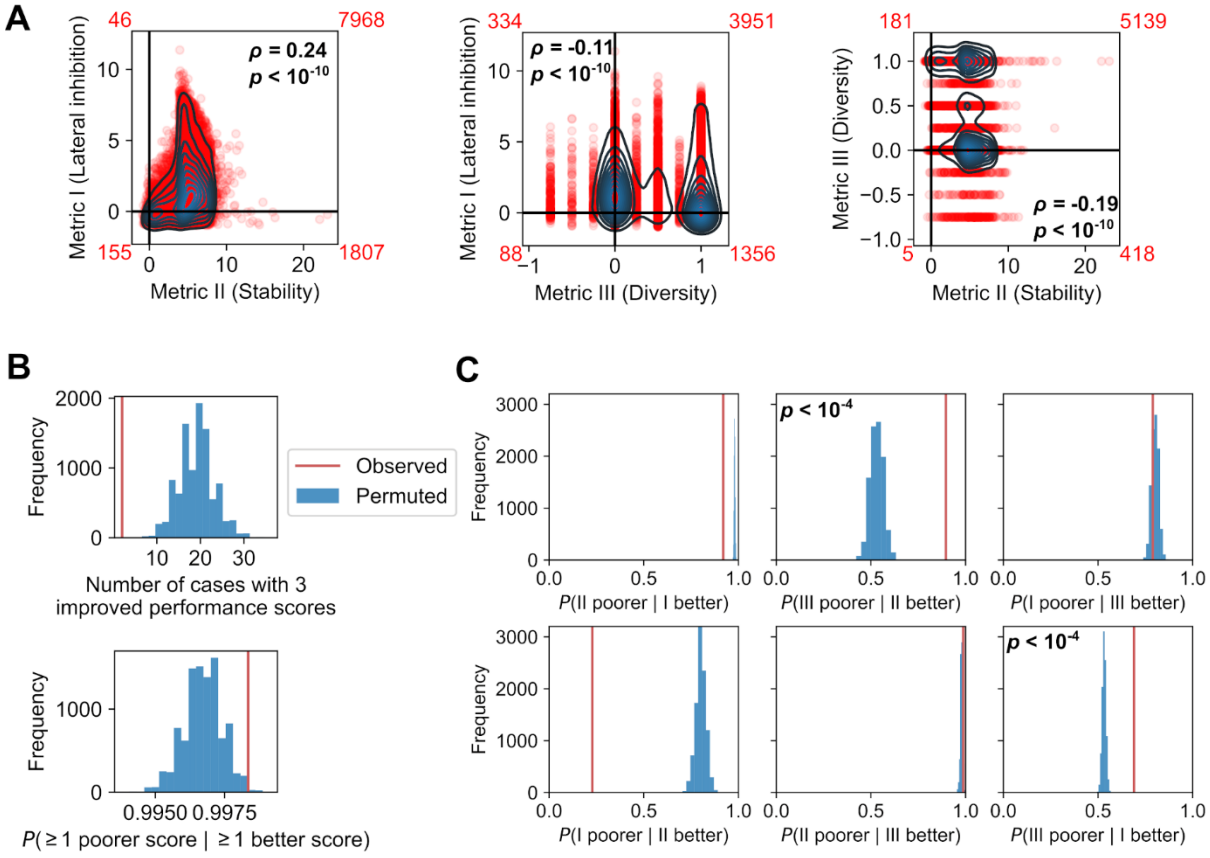

Figure 7. Tradeoffs in optimizing parameters to gain better performance of SAM patterning. 10,000 models were generated with random parameter values around those of the basal (wild-type) model. These values were chosen from a uniform distribution bounded by ±50% from the corresponding basal values in the wild-type model. Each model was simulated in the same way as with the basal model, and then the steady state SAM patterning was scored with the three metrics mentioned in Figure 5 (see Methods for details). Positive scores mean poorer performance than wild-type model. Negative scores mean better performance than wild-type model. **A**. Score distributions in phase space of all pairs of metrics. Red numbers show cases in quadrants, e.g. numbers for the lower left quadrants show the numbers of models with improved scores from basal model in two metrics. Models with scores on the x or y axis were not included in red numbers. Spearman correlation coefficient and its *p*-value are shown in each panel. **B**. The scores of the perturbed models were arranged in a 10,000×3 matrix. Each of the three columns were randomly permutated 10,000 times independently, and the resulting 10,000 matrices were analyzed based on statistics of their rows. Blue: histogram of scores or probabilities with permuted scores. Red: Observed scores or probabilities with the perturbed models. Top panel shows the cases with three better (improved) scores (there are two observed cases out of the 10,000). Lower panels show the probability of obtaining at least one poorer score under the condition of obtaining at least one better score. **C**. Pairwise conditional probabilities of obtaining opposite performance in two metrics. The right-tail *p*-value is > 0.05 unless otherwise indicated.

CLV3 signal originating from the top central SAM to restrict *WUS* expression to the organizing center in the meristem rib. In addition, this peripheral signal synergizes with the WUS and HAM signals from the meristem rib to restrict *CLV3* expression to the top central SAM. Notably, this localization of *CLV3* expression can be achieved without assuming pocket-like expressionregions of any inhibitory factor [12,27]. The prominent roles of EPFL in regulating SAM patterning by modulating *WUS* and *CLV3* expression is consistent with its key roles in plant development that were identified previously [28,30]. The model reveals a remarkable cooperativity of the peripheral and middle signals for shaping the patterning of *WUS* and *CLV3* expression. This cooperativity is particularly manifested in our observation that *WUS* expression in the lateral SAM region is controlled by both CLV3 and EPFL, each of which has partial but significant impact on *WUS* inhibition. Our results suggest that stem cell maintenance in *Arabidopsis* requires a highly regulated crosstalk between the middle and peripheral regions of the SAM rather than signals in the middle apical-basal axis alone.

Patterning and size regulation of the SAM and model limitations

Our modeling study focuses on gene expression patterning, which has a major influence on the size of the SAM. Because of the central role of WUS in maintaining the stem cell population and its positive correlation with cell proliferation rates, it is reasonable to use changes in the amount of WUS in the SAM as an indicator for changes in SAM size. For example, upregulation of *WUS* that was observed in *erf*, *clv3* and other mutants is expected to correlate with an increase of stem cell populations, which in turn gives rise to an increase in SAM size. This is consistent with previous experimental observations under such conditions [29,34,40,46,47]. However, the interplay between cell proliferation and gene expression patterning is bidirectional, dynamic, and more complex than this simple inference assumes. For example, lateral expansion of the SAM during

development could in theory reduce the effect of EPFL on the middle region unless the production rate of EPFL scales with the expansion. Understanding these forms of interplay will be important for quantitative characterization of SAM patterning and size control. Furthermore, it has been shown that the size and the shape of the SAM undergo significant changes in processes such as ontogeny [48], suggesting the complexity of the size-patterning interplay. Finally, cytokinin and auxin hormones, transcription factor SHOOTMERISTEMLESS (STM), microRNAs and other CLE peptides may influence meristem patterning directly, by regulating the rate of cell proliferation, or by interacting with the WUS-CLV3 loop [5,49-55]. Ultimately, these regulators also need to be incorporated into the model of SAM regulation once their role in the SAM and the interplay with the WUS-CLV3 loop are clearly defined. Nonetheless, our work provides critical insights into the middle-peripheral interplay of SAM patterning, which can serve as a foundation for future development of more complex and more realistic models of SAM growth.

The roles of paradoxical feedbacks

It has been long considered that the negative feedback between *WUS* and *CLV3* plays an essential role in maintaining the stem cell population in the SAM [8,9]. The self-limiting property of negative feedback ensures the stable expression of both genes. However, recent data suggest that the interactions between *WUS* and *CLV3* might be more complex than a negative feedback loop: WUS and HAM from the meristem rib can inhibit *CLV3*, which is prevented from being expressed below the subepidermal layer [12,14,35]. As such, WUS and CLV3 are involved in a negative feedback loop as well as a positive (or double-negative) feedback loop. The latter network motif is known for its function in generating switch-like behaviors and formation of tissue boundaries during development [56,57]. Consistent with these features, we found that this

interconnected, paradoxical feedback WUS-CLV3 network supports the stability of WUS expression against alteration of kinetic rates, and it facilitates the diversification of SAM cells, in particular cells in the middle region, into *WUS*^{on} and *CLV3*^{on} cells. Although the two types of cells do not have a clear boundary along the apical-basal axis at single cell-layer resolution, the formation of a heterogeneous population with stable phenotypic composition is consistent with established theories about positive feedback loops [58].

Since the homeostatic function of a negative feedback loop does not necessarily depend on the spatial separation of two types of molecules, why does the SAM need to separate *WUS*^{on} and *CLV3*^{on} cells? One plausible reason is that the stem cell transcriptional program depends on a high concentration of CLV3 and a low concentration of WUS. Another possibility is that the differential cell proliferation rates along the apical-basal axis [22], which can be governed by heterogeneous expression patterns of *WUS* and *CLV3*, may play essential roles in maintaining the structure of the SAM. Future work is warranted to connect these molecular and cellular features of SAM patterning to the physiology of plants.

Tradeoffs in optimizing the SAM gene regulatory network

Tradeoffs in designing biological circuits have been extensively studied previously; e.g., the tradeoff between noise attenuation and speed of response, and that between maximizing information content in individual cells and cell populations [59,60]. However, the roles of tradeoffs in complex traits such as tissue patterning remain elusive. Although the exact physiological function of SAM patterning is only partially understood, it is clear that the structure of the SAM gene regulatory network and its underlying biochemical properties serve multiple purposes, because diverse alterations of SAM patterning are often associated with abnormal development ranging from organ formation failure to nonoptimal size of organisms[6,28,41]. Our modeling study

revealed that the kinetic rates in the SAM gene regulatory network have a general tradeoff among achieving multiple 'desired' features of patterning. For example, parameter sets that can achieve more diverse populations of *WUS*^{on} and *CLV3*^{on} cells are likely associated with less stability in terms of *WUS* expression, or less regulation of *WUS* expression in the lateral region. These nontrivial tradeoffs may act as a complex selection pressure similar to multi-objective optimization problems, and they can play crucial roles in shaping the structure and kinetic rates of the SAM regulatory network through evolution. Furthermore, while there are a wide variety of SAM regulations in plants and a single optimal set of biochemical kinetic rate constants may not exist even within a single species, the tradeoff among the goals may serve as a general principle in shaping these kinetic rate constants.

Overall, our model includes a few key elements for controlling SAM patterning that were not considered previously. It captures many patterning phenotypes observed under normal conditions and with genetic perturbations. It offers insights into the interplay between peripheral and middle SAM signals, the intricate feedback regulations, and the principles governing the network design of this system.

Methods

Construction of mathematical model

To model the spatiotemporal dynamics of gene regulation in the shoot apical meristem (SAM), we considered 51 cells that are organized in a dome-like structure. We estimated this number of cells in the SAM from Chen et al. [47], and a similar number was used in a recent SAM model [12]. We described this 2D cellular network with 51 points within a half-circle with a radius of 25 μm [47]. In the model, the diffusive EPFL ligands are synthesized in the peripheral regions distant from the middle apical-basal axis and inhibit the expression of both *WUS* and *CLV3* through binding

to their receptors which are assumed to be broadly expressed in the SAM [28,29]. CLV3 is a diffusive peptide, and WUS is a transcription factor that moves across cells [10,37,38]. In addition to the WUS-CLV3 negative feedback and these lateral regulators, our model describes a HAIRY MERISTEM (HAM) signal that originates from the rib zone and inhibits *CLV3* expression in the organizing center [12]. In this model, we do not assume that HAM can move across cells due to the lack of experimental evidence. The spatial distribution of *HAM* expression is established by a diffusive microRNA that is not considered in the model explicitly [5]. It has been shown that HAM and WUS control gene expression synergistically [35], and that high concentration of WUS may also contribute to *CLV3* downregulation [14]. We therefore assumed that the inhibition of *CLV3* expression by HAM signal depends on WUS. As such, WUS has a paradoxical role (both activation and inhibition) in regulating *CLV3* in the presence of HAM. Finally, we considered a CLV3 independent positive feedback involving WUS. This feedback may be supported by a WUS-cytokinin mutual activation loop: it was previously shown that cytokinin activates *WUS* expression [22,34,39], whereas WUS derepresses cytokinin signal by inhibiting Type A *ARABIDOPSIS RESPONSE REGULATOR* (ARR) genes which act as inhibitors of cytokinin [13,32,33]. In addition, the WUS autoactivation loop may be supported by other factors. Based on these assumptions, dynamics of six interacting species representing concentrations of regulatory molecules is described with nonlinear ordinary differential equations (ODEs) in each cell (point) of the model (additional spatial constraints are shown in **Figure 2.1B**):

$$\frac{dW_p}{dt} = k_{W_p} W_r - b_W W_p + D_W \Delta W_p$$

$$\frac{dC_p}{dt} = k_{C_p} C_r - b_C C_p + D_C \Delta C_p$$

$$\frac{dW_r}{dt} = k_{W_r}\left(\frac{k_{WL}}{1+\left(\frac{L}{K_{WL}}\right)^{n_{WL}}} + \frac{k_{WC}}{1+\left(\frac{C_p}{K_{WC}}\right)^{n_{WC}}}\right)\left(k_{0W} + \frac{\left(\frac{W_p}{K_{WW}}\right)^{n_{WW}}}{1+\left(\frac{W_p}{K_{WW}}\right)^{n_{WW}}}\right) - b_{W_r}W_r$$

$$\frac{dC_r}{dt} = \frac{k_{C_r}}{1+\left(\frac{L}{K_{CL}}\right)^{n_{CL}}}\left(a_C + \frac{\left(\frac{W_p}{K_{CW}}\right)^{n_{CW}}}{1+\left(\frac{W_p}{K_{CW}}\right)^{n_{CW}}}\right)\frac{1}{1+\left(\frac{H}{K_{CH}}\right)^{n_{CH}}} - b_{C_r}C_r$$

$$\frac{dL}{dt} = k_L - b_L L + D_L \Delta L$$

$$\frac{dH_p}{dt} = k_P - b_P H_p$$

$$\frac{dH}{dt} = k_H \frac{\left(\frac{W_p}{K_{HW}}\right)^{n_{HW}}}{1+\left(\frac{W_p}{K_{HW}}\right)^{n_{HW}}} H_p - b_H H \qquad (1)$$

Here, state variables W_r, W_p, C_r, C_p, L and H_p represent the concentrations (or strengths) of *WUS* mRNA, WUS protein, *CLV3* mRNA, CLV3 protein, EPFL, and HAM respectively. H represents a meristem rib signal that combines both HAM and WUS, the latter of which inhibits *CLV3* expression at high concentration. A full list of parameter descriptions and their numerical values is available in **Table S1**. Briefly, k_X is the production rate constant of molecule X; b_X is the degradation rate constant of molecule X; K_{XY} is the threshold of activation or inhibition of X by Y. n_{XY} is the cooperativity of activation or inhibition of X by Y; D_X is the rate constant of passive diffusion-like transport of molecule X; Δ is the Laplace operator describing gradients of concentrations, which govern passive diffusion-like transport; ΔX has a unit of concentration per unit area. D_X was adjusted by multiplying with a scaling factor $\langle l \rangle / l$, where l represents the distance between the centers of the two cells [61]; and neighboring cells are defined as cells that are located within a radius of 10 μm. We neglected the subcellular geometry of the cells, their contact areas and the influence of mechanics in this study (the effected contact area for WUS

transport cannot be directly inferred from total contact area of plasma membrane) [12]. The diffusion of EPFL and CLV3, and the diffusion-like symplastic transport of WUS are responsible for the intercellular communication in the model. We used Hill function to describe nonlinearity in the gene regulation. Previous models of the SAM and other complex systems have used similar nonlinear functions [16,18,27,62]. a_C is a constant for us perturb the negative feedback regulation (see next section). When a molecule is controlled by multiple factors, we assumed a multiplicative form of Hill functions (AND-gate-like) (for example, nonlinear interaction of WUS and HAM may arise from their physical interactions [35]), except for the inhibitions of *WUS* by CLV3 and EPFL, which were assumed to be additive (OR-gate-like). Because the absolute concentrations of these molecules have not been measured experimentally, we used an arbitrary unit (a.u.) to describe concentration (or strength) of each molecule. Once these measurements become available, one can easily scale these variables to fit to specific concentrations. We used no-flux boundary condition for the model, and this is similar to a recently published SAM model [12].

We fit the parameters to known patterning phenotypes of the SAM under normal and genetically perturbed conditions (see details of mutant models below). These phenotypes are listed in **Table 1**. Because only qualitative information is available from the experimental data, we performed the fitting manually. Here, we do not attempt to obtain an optimal set of parameters that give the best fit to experimental data. We instead discuss the general trends of the influence of each parameter on multiple features of the SAM patterning (see Performance Metrics). To perform a simulation for a SAM system, we solved the system of ODEs numerically using the Tellurium package [63]. The initial concentrations for all variables were set to zero. An example of the time

course solution of the wild type SAM is shown in Movie S1. For all our analyses, steady state solutions (at Day 100) were used to determine the patterning of the SAM.

Simulations for mutants

For each mutant SAM model, we simulated the genetic perturbation by setting the production rate constant for the knocked-out gene(s) to zero. These parameters include k_{W_r} for the *wus* mutant, k_{C_r} for the *clv3* mutant, k_L for the *erf* mutant, and k_H for the *ham* mutant.

To examine the roles of individual interactions in the gene regulatory network, e.g. the activation of *CLV3* by EPFL, we set the parameters describing the activation/inhibition thresholds (K) of the interactions to 1000 a.u., which exceeds the maximum concentrations of the activators/inhibitors.

All other parameters were kept the same as those in the wild-type model. Steady state distributions of all modeled molecules were obtained with the same procedure as the simulation for the wild-type SAM.

Normalization of concentrations for visualization

All analyses of molecular abundance (concentrations) were based on raw values obtained from the simulations. However, because visualization of the SAM patterning with multiple molecules would involve using the same color scale (jet colormap) for different ranges of concentrations, we normalized the concentrations of all molecules by dividing all values by their own maximum concentration across all genotypes before visualization. Therefore, the ranges of all visualized abundance are [0, 1], where the value 1 effectively represents the maximum concentrations of individual molecules across all simulations.

Models without feedback loops

To examine the roles of feedback loops on SAM patterning, we created two alternative models, each of which has a feedback loop (negative or positive) removed from the basal (wild type) model. To 'knockout' a feedback loop, we first removed the regulation of *CLV3* by either the WUS or HAM signal by setting threshold constants (K) to 1000 a.u.. The removal of these interactions generates prominent changes of SAM patterning. For example, if WUS-to-*CLV3* inhibition is removed from the basal model, then *CLV3* is not expressed in the SAM and *WUS* is highly expressed compared to the basal model. However, these changes may not reflect the fitness advantage of the feedback loop because the other kinetic rate constants can be altered to compensate for the effect of the removal of the interactions. We therefore further adjusted the parameters to mimic this compensation. For the negative feedback knockout model, we introduced an activation signal for CLV3 by letting $a_c = 1$, reducing k_{C_r} by 15%, and reducing k_{W_r} by 50%. With this adjustment, the *WUS* expression pattern became comparable to the wild type. For the positive feedback knockout model, we reduced k_{C_r} by 85% and reduced k_{W_r} by 50%. The *WUS* expression pattern with this model also became comparable to the wild type. After these changes, we compared the feedback knockout models with the basal model in terms of *WUS* expression patterning in similar dynamic ranges.

Performance metrics for SAM patterning

To quantify the effect of changes in parameter values on SAM patterning, we used three performance metrics. These metrics are used to describe traits that might be critical for normal plant physiology rather than fit to experimental data, which are not available in a quantitative manner in most studies of SAM patterning. We do not claim that plants optimize their biochemical rate constants to achieve these three goals in general, because there are many other

objectives that plants must achieve to gain better fitness. Our focus is rather on the relationship among these three goals.

Metric I (lateral inhibition) describes the ability of the system to inhibit *WUS* expression in the lateral region of the SAM. Specifically, it is the total *WUS* mRNA at steady state in 34 cells that are closest to the peripheral boundaries, i.e.

$$M_1 = \sum_{i}^{l} w_i \tag{2}$$

where l is the total number of cells in the lateral region (34), and w_i is the steady state WUS mRNA concentration in cell i.

Metric II (WUS stability) measures the deviations of total WUS in the SAM from unperturbed models to perturbed models when the mRNA production rate constant k_{W_r} is reduced by 0-50%. We chose 10 levels of such reduction in the parameter in the interval [0, 0.5], and obtained the deviation score given by:

$$M_2 = \sum_{i}^{m} \sum_{j}^{n} \left| W_{i,j} - W_j^0 \right| \tag{3}$$

where m is the number of perturbations (10), n is the number of cells the SAM (51), and $W_{i,j}$ is the steady state level of WUS protein in cell j with perturbation i, and W_j^0 is the steady state level of WUS protein in cell j with the unperturbed parameter set.

Metric III (*WUS*-*CLV3* heterogeneity) describes the size and heterogeneity of the cell population consisting of $WUS^{on}CLV3^{off}$ and $WUS^{off}CLV3^{on}$ cells in the middle region of the SAM. First, the *WUS* and *CLV3* expression was binarized with a threshold of 0.5 a.u.. Next, we calculated the heterogeneity score with the following function:

$$M_3 = |x - y| - (x + y) \tag{4}$$

where x is the total number of *WUS*^{on}*CLV3*^{off} cells in the middle region (17 cells closest to the central axis) of the SAM, and y is the total number of *WUS*^{off}*CLV3*^{on} cells in the same region. The scores of the basal (wild type) model are 5.3, 0.48 and -8 for M_1, M_2 and M_3 respectively. We perturbed the parameters in the basal model in two ways and then examined the performance of the perturbed models (note that this perturbation is different from that in Metric II). In the first analysis, we decreased each parameter of the model by 2-fold, and then increased it by 2-fold. These two perturbations were performed for each parameter and six scores were obtained. In the second analysis, we perturbed all parameters in the model by randomly selecting their values from the intervals $[u/2, 3u/2]$, where u is the basal value of each parameter. These parametric changes represent the alterations of biochemical rate constants that may occur through evolution to achieve desired fitness goals.

Since we are interested in how these performance scores (M_1, M_2 and M_3) change when the parameters of the model are systematically perturbed from the basal set, we further normalized the raw values of these scores with the performance score obtained from the basal parameter, i.e.

$$m = \frac{M - M^0}{|M^0|} \tag{5}$$

where M is the performance score of the perturbed model, and M^0 is the performance score of the basal model. The same normalization was used to scale the scores for all three metrics. As such, if the perturbation gives rise to a performance better than that obtained with the basal set, the normalized score is negative. If the performance is poorer than that with that obtained with the basal set, the normalized score is positive.

Permutation test

The parametric perturbations and performance scoring described in the previous section generate performance scores that can be organized in an $n \times 3$ matrix, where n is the number of

perturbations. In our random perturbation of parameters, the value of n is 10^4. We are interested in whether there exists a significant tradeoff in obtaining better scores of all three metrics when multiple parameters are perturbed. We first described a possible tradeoff in a small number of cases in which all three performance scores are improved ($m < 0$) in these n perturbations. Out of the 10^4 parametric perturbations, only 2 of them gave rise to three negative scores. To test whether this number is significantly low, given that the total numbers of improved (better than basal) scores for the three metrics are 1964, 2020 and 423, respectively, we permutated each column of the matrix independently for 10^4 times. We next compared the distribution of the numbers of cases in which all three performance scores are improved in these 10^4 matrices with the observed number of cases (2), and we calculated the empirical *p*-value with the area of the left-tail of the distribution with the right bound of 2, i.e. the probability of observing 2 or less cases.

The same strategy was used to quantify the significance of other descriptions of tradeoffs. We tested whether there is a significantly high probably of obtaining one or more poorer-than-basal score when an improved score (in any metric) is obtained with a parameter set. This analysis was then performed for each pair of metrics, i.e. permutation tests for six conditional probabilities were conducted. In these analyses, empirical right-tail *p*-values were obtained.

Resource Availability

Computer code for reproducing all key results and figures is available at:

https://github.com/lfsc507/sam

Acknowledgements

This work was supported by the National Institute of General Medical Sciences of the National Institutes of Health under Award R01GM140462 to TH. This work was supported by the

National Science Foundation (grant no. IOS–2016756 to ES). Funding sources had no such involvement in study design; in the collection, analysis and interpretation of data; in the writing of the report; or in the decision to submit the article for publication.

Declaration of Interests

The authors declare no conflict of interest.

References

1 Scheres, B. Stem-cell niches: nursery rhymes across kingdoms. *Nat Rev Mol Cell Biol* **8**, 345-354 (2007). https://doi.org/10.1038/nrm2164

2 Sablowski, R. The dynamic plant stem cell niches. *Curr Opin Plant Biol* **10**, 639-644 (2007). https://doi.org/10.1016/j.pbi.2007.07.001

3 Uchida, N. & Torri, K. U. Stem cells within the shoot apical meristem: identity, arrangement and communication. *Cell Mol Life Sci* **76**, 1067-1080 (2019).

4 Kitagawa, M. & Jackson, D. Control of Meristem Size. *Annu Rev Plant Biol* **70**, 269-291 (2019). https://doi.org/10.1146/annurev-arplant-042817-040549

5 Han, H. *et al.* A signal cascade originated from epidermis defines apical-basal patterning of Arabidopsis shoot apical meristems. *Nature communications* **11**, 1-17 (2020).

6 Fletcher, J. C., Brand, U., Running, M. P., Simon, R. & Meyerowitz, E. M. Signaling of cell fate decisions by CLAVATA3 in Arabidopsis shoot meristems. *Science* **283**, 1911-1914 (1999). https://doi.org/10.1126/science.283.5409.1911

7 Laux, T., Mayer, K. F., Berger, J. & Jurgens, G. The WUSCHEL gene is required for shoot and floral meristem integrity in Arabidopsis. . *Development* **122**, 87-96 (1996).

8 Schoof, H. *et al.* The stem cell population of Arabidopsis shoot meristems is maintained by a regulatory loop between the CLAVATA and WUSCHEL genes. *Cell* **100**, 635-644 (2000).

9 Brand, U., Fletcher, J. C., Hobe, M., Meyerowitz, E. M. & Simon, R. Dependence of stem cell fate in Arabidopsis on a feedback loop regulated by CLV3 activity. *Science* **289**, 617-619 (2000). https://doi.org/10.1126/science.289.5479.617

10 Yadav, R. K. *et al.* WUSCHEL protein movement mediates stem cell homeostasis in the Arabidopsis shoot apex. *Genes Dev* **25**, 2025-2030 (2011). https://doi.org/10.1101/gad.17258511

11 Somssich, M., Je, B. I., Simon, R. & Jackson, D. CLAVATA-WUSCHEL signaling in the shoot meristem. *Development* **143**, 3238-3248 (2016). https://doi.org/10.1242/dev.133645

12 Zhou, Y. *et al.* HAIRY MERISTEM with WUSCHEL confines CLAVATA3 expression to the outer apical meristem layers. *Science* **361**, 502-506 (2018).

13 Shimotohno, A. & Scheres, B. Topology of regulatory networks that guide plant meristem activity: similarities and differences. . *Curr Opin Plant Biol* **51**, 74-80 (2019).

14 Perales, M. *et al.* Threshold-dependent transcriptional discrimination underlies stem cell homeostasis. *Proc Natl Acad Sci U S A* **113**, E6298-E6306 (2016). https://doi.org/10.1073/pnas.1607669113

15 Jönsson, H. *et al.* Modeling the organization of the WUSCHEL expression domain in the shoot apical meristem. *Bioinformatics* **21**, i232-i240 (2005).

16 Nikolaev, S. V., Penenko, A. V., Lavreha, V. V., Mjolsness, E. D. & Kolchanov, N. A. A model study of the role of proteins CLV1, CLV2, CLV3, and WUS in regulation of the structure of the shoot apical meristem. *Russian Journal of Developmental Biology* **38**, 383-388 (2007).

17 Hohm, T., Zitzler, E. & Simon, R. A dynamic model for stem cell homeostasis and patterning in Arabidopsis meristems. *PLoS One* **5**, e9189 (2010). https://doi.org/10.1371/journal.pone.0009189

18 Fujita, H., Toyokura, K., Okada, K. & Kawaguchi, M. Reaction-diffusion pattern in shoot apical meristem of plants. *PLoS One* **6**, e18243 (2011). https://doi.org/10.1371/journal.pone.0018243

19 Adibi, M., Yoshida, S., Weijers, D. & Fleck, C. Centering the Organizing Center in the Arabidopsis thaliana Shoot Apical Meristem by a Combination of Cytokinin Signaling and Self-Organization. *PLoS One* **11**, e0147830 (2016). https://doi.org/10.1371/journal.pone.0147830

20 Gruel, J. *et al.* An epidermis-driven mechanism positions and scales stem cell niches in plants. *Sci Adv* **2**, e1500989 (2016). https://doi.org/10.1126/sciadv.1500989

21 Gruel, J., Deichmann, J., Landrein, B., Hitchcock, T. & Jönsson, H. The interaction of transcription factors controls the spatial layout of plant aerial stem cell niches. *NPJ systems biology and applications* **4**, 36 (2018).

22 Chickarmane, V. S., Gordon, S. P., Tarr, P. T., Heisler, M. G. & Meyerowitz, E. M. Cytokinin signaling as a positional cue for patterning the apical–basal axis of the growing Arabidopsis shoot meristem. *Proceedings of the National Academy of Sciences* **109**, 4002-4007 (2012).

23 Banwarth-Kuhn, M. *et al.* Cell-Based Model of the Generation and Maintenance of the Shape and Structure of the Multilayered Shoot Apical Meristem of Arabidopsis thaliana. *Bull Math Biol* **81**, 3245-3281 (2019). https://doi.org/10.1007/s11538-018-00547-z

24 Klawe, F. Z. *et al.* Mathematical modeling of plant cell fate transitions controlled by hormonal signals. *PLoS Comput Biol* **16**, e1007523 (2020). https://doi.org/10.1371/journal.pcbi.1007523

25 Mayer, K. F. *et al.* Role of WUSCHEL in regulating stem cell fate in the Arabidopsis shoot meristem. *Cell* **95**, 805-815 (1998). https://doi.org/10.1016/s0092-8674(00)81703-1

26 Jonsson, H. *et al.* Modeling the organization of the WUSCHEL expression domain in the shoot apical meristem. *Bioinformatics* **21 Suppl 1**, i232-240 (2005). https://doi.org/10.1093/bioinformatics/bti1036

27 Gruel, J., Deichmann, J., Landrein, B., Hitchcock, T. & Jonsson, H. The interaction of transcription factors controls the spatial layout of plant aerial stem cell niches. *NPJ Syst Biol Appl* **4**, 36 (2018). https://doi.org/10.1038/s41540-018-0072-1

28 Kosentka, P. Z., Overholt, A., Maradiaga, R., Mitoubsi, O. & Shpak, E. D. EPFL Signals in the Boundary Region of the SAM Restrict Its Size and Promote Leaf Initiation. *Plant Physiol* **179**, 265-279 (2019). https://doi.org/10.1104/pp.18.00714

29 Zhang, L., DeGennaro, D., Lin, G., Chai, J. & Shpak, E. D. ERECTA family signaling constrains CLAVATA3 and WUSCHEL to the center of the shoot apical meristem. *Development* **148** (2021). https://doi.org/10.1242/dev.189753

30 Kimura, Y., Tasaka, M., Torii, K. U. & Uchida, N. ERECTA-family genes coordinate stem cell functions between the epidermal and internal layers of the shoot apical meristem. *Development* **145**, dev156380 (2018).

31 Brand, U., Grünewald, M., Hobe, M. & Simon, R. Regulation of CLV3 expression by two homeobox genes in Arabidopsis. *Plant physiology* **129**, 565-575 (2002).

32 Leibfried, A. *et al.* WUSCHEL controls meristem function by direct regulation of cytokinin-inducible response regulators. *Nature* **438**, 1172 (2005).

33 To, J. P. C. *et al.* Type-A Arabidopsis response regulators are partially redundant negative regulators of cytokinin signaling. *The Plant Cell* **16**, 658-671 (2004).

34 Wang, J. *et al.* Cytokinin signaling activates WUSCHEL expression during axillary meristem initiation. *The Plant Cell* **29**, 1373-1387 (2017).

35 Zhou, Y. *et al.* Control of plant stem cell function by conserved interacting transcriptional regulators. *Nature* **517**, 377 (2015).

36 Reddy, G. V. & Meyerowitz, E. M. Stem-cell homeostasis and growth dynamics can be uncoupled in the Arabidopsis shoot apex. *Science* **310**, 663-667 (2005).

37 Lenhard, M. & Laux, T. Stem cell homeostasis in the Arabidopsis shoot meristem is regulated by intercellular movement of CLAVATA3 and its sequestration by CLAVATA1. *Development* **130**, 3163-3173 (2003).

38 Daum, G., Medzihradszky, A., Suzaki, T. & Lohmann, J. U. A mechanistic framework for noncell autonomous stem cell induction in Arabidopsis. *Proc. Natl. Acad Sci. U. S. A.* **111**, 14619-14624 (2014).

39 Gordon, S. P., Chickarmane, V. S., Ohno, C. & Meyerowitz, E. M. Multiple feedback loops through cytokinin signaling control stem cell number within the Arabidopsis shoot meristem. *Proc. Natl. Acad Sci. U. S. A.* **106**, 16529-16534 (2009).

40 Uchida, N., Shimada, M. & Tasaka, M. ERECTA-family receptor kinases regulate stem cell homeostasis via buffering its cytokinin responsiveness in the shoot apical meristem. *Plant Cell Physiol.* **54**, 343-351 (2013).

41 Schulze, S., Schäfer, B. N., Parizotto, E. A., Voinnet, O. & Theres, K. LOST MERISTEMS genes regulate cell differentiation of central zone descendants in Arabidopsis shoot meristems. *The Plant Journal* **64**, 668-678 (2010).

42 Müller, R., Borghi, L., Kwiatkowska, D., Laufs, P. & Simon, R. Dynamic and compensatory responses of Arabidopsis shoot and floral meristems to CLV3 signaling. *The Plant Cell* **18**, 1188-1198 (2006).

43 Yadav, R. K., Tavakkoli, M. & Reddy, G. V. WUSCHEL mediates stem cell homeostasis by regulating stem cell number and patterns of cell division and differentiation of stem cell progenitors. *Development* **137**, 3581-3589 (2010).

44 Cotterell, J. & Sharpe, J. An atlas of gene regulatory networks reveals multiple three-gene mechanisms for interpreting morphogen gradients. *Mol. Syst. Biol.* **6** (2010).

45 Zagorski, M. *et al.* Decoding of position in the developing neural tube from antiparallel morphogen gradients. *Science* **356**, 1379-1383 (2017).

46 Clark, S. E., Running, M. P. & Meyerowitz, E. M. CLAVATA3 is a specific regulator of shoot and floral meristem development affecting the same processes as CLAVATA1. *Development* **121**, 2057-2067 (1995).

47 Chen, M.-K., Wilson, R. L., Palme, K., Ditengou, F. A. & Shpak, E. D. ERECTA family genes regulate auxin transport in the shoot apical meristem and forming leaf primordia. *Plant Physiol.* **162**, 1978-1991 (2013).

48 Kwiatkowska, D. Flowering and apical meristem growth dynamics. *Journal of Experimental Botany* **59**, 187-201 (2008).

49 Williams, L., Grigg, S. P., Xie, M., Christensen, S. & Fletcher, J. C. Regulation of Arabidopsis shoot apical meristem and lateral organ formation by microRNA miR166g and its AtHD-ZIP target genes. *Development* **132**, 3657-3668 (2005).

50 Rodriguez-Leal, D. *et al.* Evolution of buffering in a genetic circuit controlling plant stem cell proliferation. *Nat. Genet.* **51**, 786-792 (2019).

51 Chung, Y. *et al.* Auxin response factors promote organogenesis by chromatin-mediated repression of the pluripotency gene SHOOTMERISTEMLESS. *Nature communications* **10**, 1-11 (2019).

52 Long, J. A., Moan, E. I., Medford, J. I. & Barton, M. K. A member of the KNOTTED class of homeodomain proteins encoded by the STM gene of Arabidopsis. *Nature* **379**, 66-69 (1996).

53 Fouracre, J. P. & Poethig, R. S. Role for the shoot apical meristem in the specification of juvenile leaf identity in Arabidopsis. *Proc. Natl. Acad Sci. U. S. A.* **116**, 10168-10177 (2019).

54 Knauer, S. *et al.* A protodermal miR394 signal defines a region of stem cell competence in the Arabidopsis shoot meristem. *Dev. Cell* **24**, 125-132 (2013).

55 Zhao, Z. *et al.* Hormonal control of the shoot stem-cell niche. *Nature* **465**, 1089-1092 (2010).

56 Dahmann, C., Oates, A. C. & Brand, M. Boundary formation and maintenance in tissue development. *Nature Reviews Genetics* **12**, 43 (2011).

57 Novak, B., Tyson, J. J., Gyorffy, B. & Csikasz-Nagy, A. Irreversible cell-cycle transitions are due to systems-level feedback. *Nat. Cell Biol.* **9**, 724-728 (2007).

58 Hong, T., Oguz, C. & Tyson, J. J. A Mathematical Framework for Understanding Four-Dimensional Heterogeneous Differentiation of CD4+ T Cells. *Bull. Math. Biol.*, 1-19 (2015). https://doi.org/10.1007/s11538-015-0076-6

59 Hong, T. *et al.* Semi-adaptive response and noise attenuation in bone morphogenetic protein signalling. *Journal of The Royal Society Interface* **12**, 20150258 (2015).

60 Suderman, R., Bachman, J. A., Smith, A., Sorger, P. K. & Deeds, E. J. Fundamental trade-offs between information flow in single cells and cellular populations. *Proc. Natl. Acad Sci. U. S. A.* **114**, 5755-5760 (2017).

61 Delile, J., Herrmann, M., Peyriéras, N. & Doursat, R. A cell-based computational model of early embryogenesis coupling mechanical behaviour and gene regulation. *Nature communications* **8**, 1-10 (2017).

62 Ye, Y., Kang, X., Bailey, J., Li, C. & Hong, T. An enriched network motif family regulates multistep cell fate transitions with restricted reversibility. *PLoS Comput. Biol.* **15**, e1006855 (2019). https://doi.org/10.1371/journal.pcbi.1006855

63 Choi, K. *et al.* Tellurium: an extensible python-based modeling environment for systems and synthetic biology. *Biosystems* **171**, 74-79 (2018).

Appendix

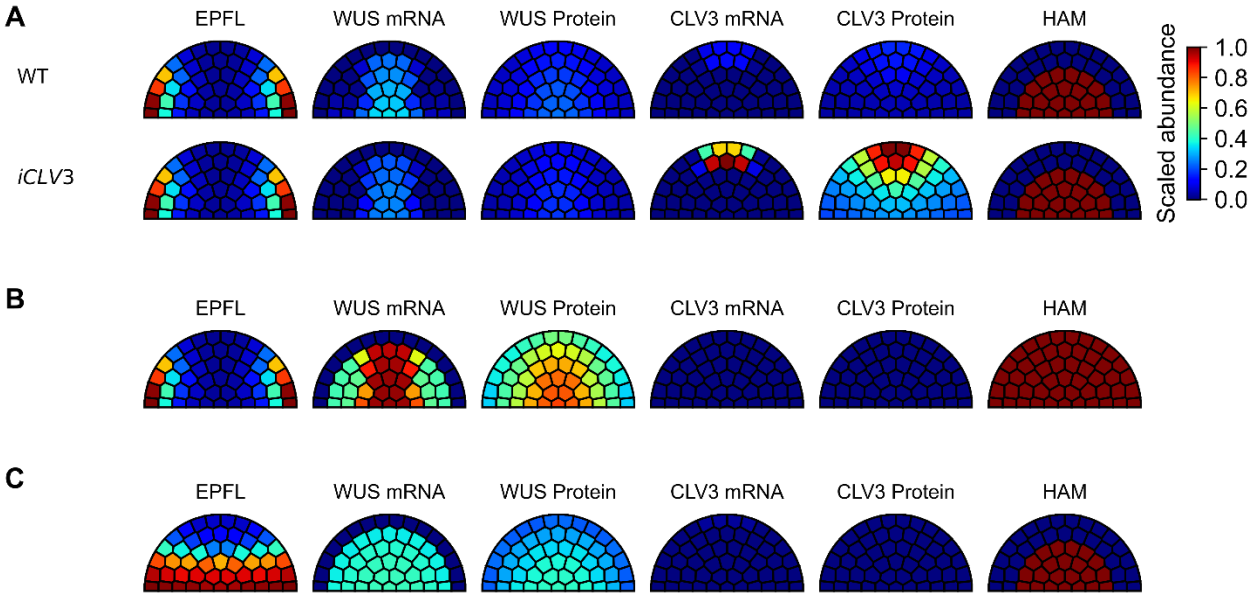

Figure S1. Additional perturbations of the SAM model. A. Bottom panels show an *iCLV3* condition under which the production rate constant of *CLV3* mRNA k_{C_r} was increased by 10-fold. Top panel show the wild-type control simulation with a color gradient normalized based on the ranges of these two simulations. **B**. A simulation with the production zone of HAM expanded to all cells. **C**. A simulation with the production zone of EPFL expanded to cells in the two bottom rows. All other parameters/assumptions were the same as the wild-type SAM model.

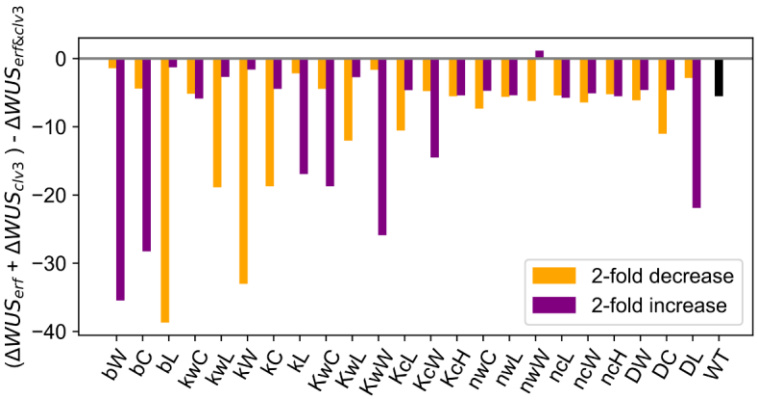

Figure S2. Synergy between EPFL and CLV3 in inhibiting lateral *WUS* expression when parameters of the model were perturbed. Synergy was measured as the difference between the sum of the amounts of lateral *WUS* mRNA in the *erf* mutant and *clv3* mutant increased from the wild type, and the amount of lateral *WUS* mRNA in the *erf-clv3* mutant increased from the wild type. A negative quantity indicates that a nonlinear cooperativity between EPFL and CLV3 exists. Each parameter was increased and decrease by 2-fold.

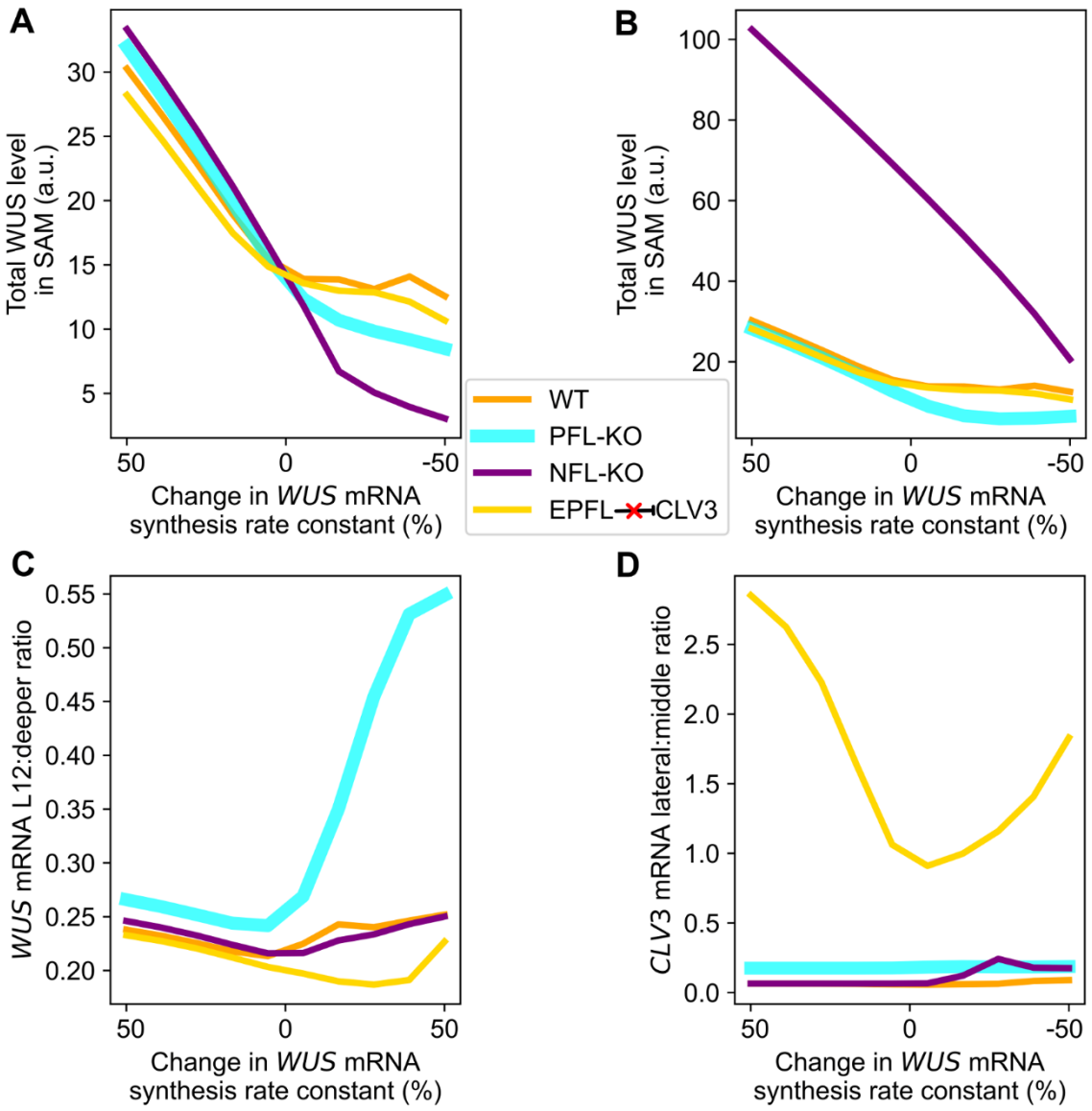

Figure S3. Robustness of the SAM patterns with respect to perturbations. A. Steady state distributions of *WUS* and *CLV3* mRNA in SAM with circuits of wild-type and three alternative models with 50% changes of *WUS* mRNA production rate constant. **B.** Steady state distributions of *WUS* and *CLV3* mRNA in SAM with circuits of wild-type and three alternative models with 50% changes of *WUS* mRNA production rate constant. The total amount of *WUS* mRNA under the unperturbed condition was not unified with the adjustment of *CLV3* expression. **C**. Steady state distributions of the ratio of *WUS* mRNA in the L1 and L2 layers to the rest of the SAM, with circuits of wild-type and three alternative models with 50% changes of *WUS* mRNA production rate constant. **D**. Steady state distributions of the lateral to middle ratio of *CLV3* mRNA, with circuits of wild-type and three alternative models with 50% changes of *WUS* mRNA production rate constant.

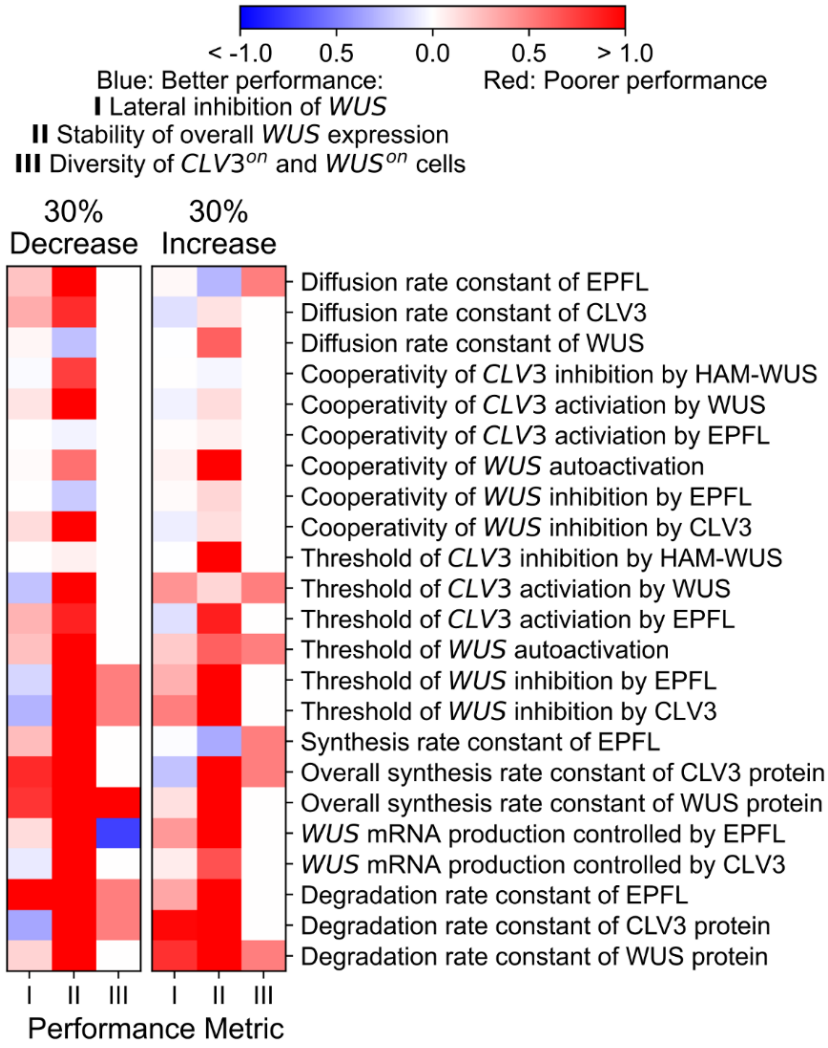

Figure S4. Influence of moderate parametric changes on three performance objectives of SAM patterning. The performance scores upon moderate perturbations of 23 parameters. Each parameter was decreased and increased by 30% and simulation was performed in the same procedure as that with the wild-type (basal) model. Steady state SAM patterning was scored based on the three metrics, and the scores were compared with those obtained with basal model. Blue: perturbed model has better score than basal model does. Red: perturbed model has poorer score than basal model does. White: perturbed model and basal model have the same score.

Table S1. Parameter values of the wild-type SAM model.

Parameter	Description	Value	Unit
K_{CW}	Threshold of *CLV3* activation by WUS	0.2	a.u.*
n_{CW}	Cooperativity of regulation of *CLV3* by WUS	6	NA
k_{C_r}	Production rate constant of *CLV3* mRNA	0.5	a.u./h
K_{CL}	Threshold of *CLV3* inhibition by EPFL	0.24	a.u
n_{CL}	Cooperativity of regulation of *CLV3* by EPFL	6	
K_{CH}	Threshold of *CLV3* activation by HAM	0.13	a.u.
n_{CH}	Cooperativity of regulation of *CLV3* by HAM	5	
k_{C_p}	Production rate constant of CLV3 protein	2.7	a.u./h
b_C	Degradation rate constant of CLV3 protein	1	/h
b_{W_r}	Degradation rate constant of *CLV3* mRNA	0.5	/h
k_{WL}	Proportion of *WUS* mRNA production rate controlled by EPFL	1	NA
k_{WC}	Proportion of *WUS* mRNA production rate controlled by CLV3	1	NA
k_{W_r}	Production rate constant of *WUS* mRNA	1.2	a.u./h
K_{WW}	Activation threshold of WUS autoactivation	0.53	a.u
n_{WW}	Cooperativity of WUS self-regulation	2	NA
K_{WL}	Threshold of *WUS* inhibition by EPFL	0.29	a.u
n_{WL}	Cooperativity of regulation of *WUS* by EPFL	6	NA
K_{WC}	Threshold of *WUS* inhibition with CLV3	0.1	a.u
n_{WC}	Cooperativity of regulation of *WUS* by CLV3	6	NA
k_{W_p}	Production rate constant of WUS protein	0.345	a.u./h
b_W	Degradation rate constant of WUS protein	0.4	/h
b_{W_r}	Degradation rate constant of *WUS* mRNA	1	/h
k_{0W}	Production rate constant of *WUS* mRNA independent of autoactivation	0.3	NA
a_C	Constant for generating negative feedback free model	0	NA
K_{HW}	Threshold of HAM-WUS signal activation by WUS	0.3	a.u.
n_{HW}	Cooperativity of regulation of HAM-WUS by WUS	4	NA
b_P	Degradation rate constant of HAM protein	1	/h
k_P	Production rate constant of HAM	1	a.u./h
b_H	Decay rate constant of HAM-WUS signal	1	/h
k_H	Activation rate constant of HAM-WUS signal	1	a.u./h
k_L	Production rate constant of EPFL	10	a.u./h
b_L	Degradation rate constant of EPFL protein	1.5	/h
D_W	Passive diffusion-like symplastic transport rate constant of WUS protein	1	a.u. area/h**
D_C	Passive diffusion rate constant of CLV3 peptide	6	a.u. area/h
D_L	Passive diffusion rate constant of EPFL protein	1.2	a.u. area/h

* a.u. is an arbitrary unit of concentration. ** a.u. area is an arbitrary unit of area.

CHAPTER III

ARP2/3-DEPENDENT ENDOCYTOSIS FACILITATES CDC42 OSCILLATIONS BY PERIODIC REMOVAL OF PAK1-MEDIATED NEGATIVE FEEDBACK

This chapter is based on the article pre-published below:

Harrell MA, Liu Z, Campbell BF, Chinsen O, Hong T, Das M. The Arp2/3 complex promotes periodic removal of Pak1-mediated negative feedback to facilitate anticorrelated Cdc42 oscillations. *bioRxiv 10.1101/2023.11.08.566261*: 2023.11.08.566261

The full text is available at

https://www.biorxiv.org/content/10.1101/2023.11.08.566261v1.article-info.

The experimental portion of this paper was conducted by Harrell MA, Campbell BF, Chinsen O, and Das M. I was responsible for the conceptualization, validation, formal analysis, investigation, visualization, methodology, software development, and review and editing of the manuscript.

Abstract

The GTPase Cdc42 regulates polarized growth in most eukaryotes. In the bipolar yeast *S. pombe*, Cdc42 activation cycles periodically at sites of polarized growth. These periodic cycles are caused by alternating positive feedback and time-delayed negative feedback loops. At each polarized end, negative-feedback is established when active Cdc42 recruits the Pak1 kinase to prevent further Cdc42 activation. It is unclear how Cdc42 activation returns to each end after Pak1-dependent negative feedback. We find that disrupting branched actin-mediated endocytosis disables Cdc42 reactivation at the cell ends. Using experimental and mathematical approaches we show that endocytosis-dependent Pak1 removal from the cell ends allows the Cdc42 activator Scd1 to return to that end to enable reactivation of Cdc42. Moreover, we show that Pak1 elicits its own removal via activation of endocytosis. These findings provide a deeper insight into the self-organization of Cdc42 regulation and reveal previously unknown feedback with endocytosis in the establishment of cell polarity.

Introduction

The relationship between structure and function is a core tenet of biology. This holds true for cells, which must achieve a specific shape for their function. As such, the plethora of environments and purposes that cells occupy results in a wide diversity of cellular shapes and corresponding functions. These diverse shapes are attributed to polarized growth, wherein cells organize the cytoskeleton to promote growth from specific sites [1,2]. While several works have investigated how cells polarize and acquire shape, the fundamentals of polarization are still not well understood. This is mainly because polarization involves multiple signaling proteins and pathways that are tightly regulated. Major regulators of polarized growth across most eukaryotes are the highly conserved Rho Family GTPases which consists of Cdc42, Rac, and Rho [3]. These GTPases are tightly regulated to promote cell motility, cell shape, and proliferation [3-5]. For example, the GTPases spatiotemporally regulate cell protrusions, speed and direction during migration, and promote different aspects of cell differentiation in synapse formation [6-8]. These findings indicate that the GTPases are regulated via complex higher-order pathways to ensure their proper spatiotemporal activation. Given the complexity of these pathways and the limitations of the mammalian systems, the molecular mechanisms governing cell polarization are not well understood.

The fission yeast, *Schizosaccharomyces pombe* grows in a bipolar manner from the two cell ends. In fission yeast, growth initiates at the old end, the end that existed in the previous generation, upon completion of cell division. As the cell reaches a certain size in the G2 phase, the new end that is formed as a result of cell division also initiates growth resulting in a bipolar growth pattern [9]. Similar to most eukaryotes, Cdc42 is a major regulator of cell polarization in fission yeast [10]. Fission yeast share the same conserved mechanisms as higher eukaryotes making

it an excellent model to understand higher-order molecular pathways that promote polarization and bipolarity. During bipolar growth in fission yeast, Cdc42 activity cycles on and off in a periodic manner often resulting in oscillations [11]. Cdc42 oscillations are dictated by cycles of positive feedback and time-delayed negative feedback via its regulators resulting in bipolar growth [11-13]. Cdc42 activation occurs in an anti-correlated manner between the two growing ends suggesting that the growing ends must compete for resources to sustain Cdc42 activity and growth [11,13-16]. Due to this competition, Cdc42 must be inactivated at one cell-end for the opposite end to activate Cdc42 and vice-versa [11,16]. Disruption of these Cdc42 activation cycles leads to a loss of bipolar growth [11]. It is not known how Cdc42 activity periodically returns to a cell end after each cycle of the negative-feedback to allow for the oscillations.

Cdc42 positive-feedback is mediated by the guanine nucleotide exchange factor (GEF) Scd1 and its scaffold protein Scd2 [13,17,18]. The scaffold Scd2 binds active Cdc42 and is thus recruited to the growing cell ends [19-21]. Scd2 at the cell ends then recruits Scd1 for further Cdc42 activation thus establishing a positive-feedback. Active Cdc42 can be inactivated by its GTPase activating proteins (GAPs) Rga4, Rga6, and Rga3 [22-25]. As Cdc42 activity reaches a certain threshold it triggers time-delayed negative feedback mediated by the Pak1 kinase [11,26,27]. The Pak1 kinase (p21-activated kinase) is a serine/threonine kinase and is highly conserved in regulating growth in most eukaryotes [5,28]. The Pak1 kinase is activated and recruited to the growing cell ends when it binds active Cdc42 [29,30]. When active, Pak1 phosphorylates effector proteins to modulate a host of biological pathways [11,29-34]. In the absence of Pak1 activity, Scd1 and Scd2 accumulate at the cell ends leading to increased Cdc42 activity [11]. In budding yeast, the Pak1 homolog Cla4 has been shown to phosphorylate Cdc24, the Scd1 homolog, to prevent its interaction with Bem1, the Scd2 homolog [35,36]. Together, Cdc42 positive feedback followed by time delayed negative feedback results in oscillations at growing cell ends.

Cdc42 regulates multiple pathways such as membrane trafficking and cytoskeletal F-actin organization [3,4,10,37-42]. When activated, Cdc42 in turn activates the formin, For3, to nucleate

linear actin cables[40,43-45]. Active Cdc42 also triggers branched actin polymerization, necessary for endocytosis in yeasts, through the WASP protein, Wsp1, and the type 1 myosin, Myo1 [38-40,44,46-49] . Both Wsp1 and Myo1 regulate endocytosis by binding the Arp2/3 complex to promote the nucleation of branched actin [47]. Genetic experimentation from our lab and others show that Cdc42 regulates endocytosis in fission yeast both at the division site and also at the site of cell growth and the underlying mechanisms are still being investigated [42,48,50,51]. However, it is not well understood how membrane trafficking events in turn regulate Cdc42 dynamics.

Using *in vivo* experiments alongside mathematical modeling, we find that Arp2/3-mediated endocytosis is required for proper removal of Pak1, to allow anticorrelated oscillations. When the branched actin nucleator Arp2/3 complex is inhibited, Pak1 stabilizes at a cell end, preventing localization of the GEF, Scd1, and disrupting the positive and negative feedback loops needed for periodic Cdc42 activity at that end. Arp2/3 complex mediated branched actin is required for endocytosis in fission yeast. While Cdc42 has been shown to regulate actin organization, our findings provide evidence that endocytosis also directly impacts Cdc42 activity [37,52]. It is widely acknowledged that proper protein localization is vital for activity. Here we show that timely removal of inhibition plays an equally critical role and sets the stage for positive regulators to return and continue the cycles of activity.

Results

The Arp2/3 complex is required for anticorrelated oscillations between growing cell ends.

There are two F-actin structures in *S. pombe* during interphase: linear actin cables and branched actin networks [53]. Actin cables transverse the length of the cell, physically connecting both ends, and are required for actin mediated delivery [53]. Branched actin patches are primarily located at the growing cell ends and are required for endocytosis [40,48]. Given the role for F-actin in

membrane trafficking and polarization, we asked if actin structures regulate anticorrelated Cdc42 oscillations. We used the fluorescent probe CRIB-3xGFP to specifically visualize active Cdc42 for our experiments [25]. We quantified the competition between the ends within a cell by measuring the correlation of Cdc42 activity between the ends under all experimental conditions (**Fig.8D**). To disrupt F-actin, we treated cells with an inhibitor of actin polymerization Latrunculin A (Lat-A, **Fig.8A**). As has been reported before, we find that Cdc42 oscillations are disrupted in Lat-A treated cells, resulting in loss of CRIB-3xGFP signal at the cell ends and increased depolarized signal along the cell sides [54,55]. Lat-A treated cells displayed enhanced correlation of CRIB-3xGFP signal between cells ends (**Fig.8D**).

To identify the nature of actin filament involved in regulating Cdc42 oscillations, we analyzed four conditions: DMSO, Lat-A, *for3*Δ, and CK-666. DMSO treatment served as a control (**Fig.8A, B**). *for3*Δ mutants lack actin cables and cells treated with the Arp2/3 inhibiting drug CK-666 lack branched actin [40,44,56-58]. We then compared the level of anticorrelation between the cell ends in the absence of each actin structure (**Fig.8D**). Interestingly, we find that *for3*Δ mutants still show anti-correlated active Cdc42 oscillations, similar to DMSO-treated cells, indicating that linear actin cables do not facilitate anticorrelation between the two ends (**Fig.8C, D**). However, cells treated with CK-666, which inhibits the Arp2/3 complex and branched actin formation, do not exhibit anti-correlated oscillations (**Fig.8C, D**). Moreover, in several cells treatment with CK-666 resulted in Cdc42 activation at mostly one end **(Fig.8A, C**). This suggests that the Arp2/3 complex plays a role in facilitating anticorrelated Cdc42 activity between the cell ends.

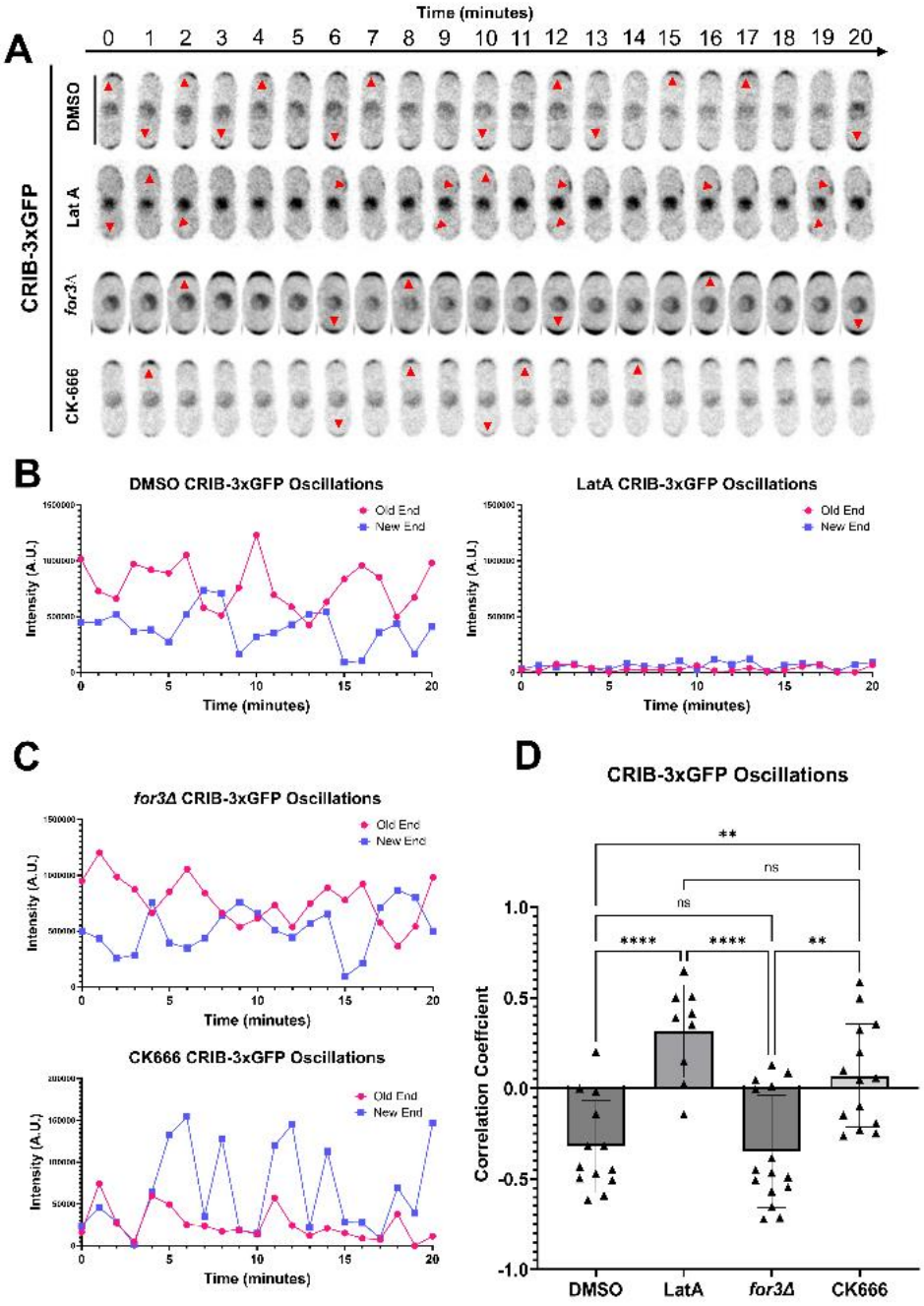

Figure 8. Branched actin is required for competition for active Cdc42 between growing ends. A. Cdc42 dynamics in CRIB-3xGFP expressing cells treated with DMSO, Lat-A, CK666 and in for3Δ mutants. Drug treatment and genetic perturbation were used to investigate the role of actin structures. Red arrow heads mark the site of Cdc42 activation. **B.** Representative CRIB-3xGFP oscillations in DMSO and Lat-A treated cells. **C.** Representative CRIB-3xGFP oscillations in for3Δ and CK-666 treated cells. **D.** Correlation coefficient of active Cdc42 oscillations between cell ends. Scale bar, 10μm. n.s., not significant; p value, *<0.05, Student's t-test.

Previous works have demonstrated that under stress conditions, including Lat-A treatment, Cdc42 activity is depolarized and is instead localized along the cell sides [54,55]. We asked if CK-666 treatment triggered a similar stress response resulting in the loss of anticorrelation. Stress response results in the activation of the mitogen-activated protein kinase (MAP kinase), Sty1 that promotes decreased localization of Scd1 at the cell ends and increased localization of the Cdc42 GEF Gef1 along the cell sides resulting in depolarized Cdc42 activation [19,55]. Gef1 is mostly cytoplasmic and shows increased cortical localization only in response to stress [59]. We analyzed CRIB-3xGFP and Gef1-mNG localization in DMSO and CK-666 treated cells. In CK-666 treated cells, we did not observe CRIB-3xGFP localization along the cell sides (**Fig.S5, A, B**) and Gef1-mNG continued to display cytoplasmic localization (**Fig.S5, C, D**). This suggests that cells must lose all F-actin structures to trigger the stress response as opposed to just branched actin. To test this, we depleted branched actin in mutants lacking linear actin cables to mimic Lat-A treatment. We treated *for3Δ* mutants with CK-666 to get rid of all F-actin structures. Indeed, we find that *for3*Δ cells when treated with CK-666 displayed depolarized CRIB-3xGFP and Gef1-mNG **(Fig.S5**). This suggests that CK-666 treatment by itself does not trigger a stress response.

Inhibition of the Arp2/3 complex depletes Scd1 from cell ends.

Next, we elucidated how inhibition of the Arp2/3 complex disrupted Cdc42's regulation resulting in loss of anticorrelation between the cell ends. The Arp2/3 complex is required for branched actin-mediated endocytosis and CK-666 treatment is known to abolish endocytosis [42,47,48,58,60]. Endocytosis is required to recycle proteins from the cell cortex [61,62]. Inhibition of endocytosis leads to accumulation of these recycled proteins at the cell cortex. We asked if the Cdc42 regulators were similarly recycled by endocytosis. We visualized fluorescently labeled Cdc42

regulators in DMSO-treated and CK-666-treated cells (**Fig.9A**). Scd1-mNG (primary GEF), Scd2-GFP (Scd1 Scaffold), and Rga4-GFP (Primary GAP) were imaged using fluorescent microscopy (**Fig.9A**) [20,23]. The Cdc42 GAP, Rga4-GFP did not show any change in its localization in CK-666 treated cells. Contrary to the expectation of endocytosis-driven recycling, we find that Scd1, and its scaffold Scd2, are significantly depleted from growing ends upon Arp2/3 complex inhibition (**Fig.9B, C**). This suggests that Scd1 and Scd2 are not recycled from the cell cortex by endocytosis, rather, endocytosis appears to enhance their localization at the cell ends. Scd1 levels are known to oscillate between the cell ends similar to active Cdc42 [11]. As a result, when imaging Scd1 at any given point of time, it either accumulates at any one cell end or is distributed between the two ends. Indeed, in a DMSO treated population, snapshots of Scd1-mNG show 53% of cells with bipolar localization. In CK-666 treated cells, in addition to decrease in levels of Scd1-mNG, we also observe bipolar localization in only 37% of cells. This suggests that in the absence of branched actin, Scd1 localization is restricted possibly due to the disruption of its oscillation.

Cdc42-GTP inhibits the accumulation of Scd1 through an intermediary molecule.

To relate our observations on polarization regulators under perturbed conditions to the core oscillator controlling Cdc42-GTP dynamics in a rigorous manner, we constructed two models to explore potential mechanisms at the systems level. With a framework combining ordinary and partial differential equations (ODE-PDE), a previous model used an assumption of Cdc42 auto-catalysis and an additional negative feedback loop between Cdc42 and Scd1 to explain Cdc42 oscillations (a classical structure chemical oscillator) [63,64]. However, there is no experimental evidence supporting the auto-catalytic function of Cdc42 to date. We therefore removed this

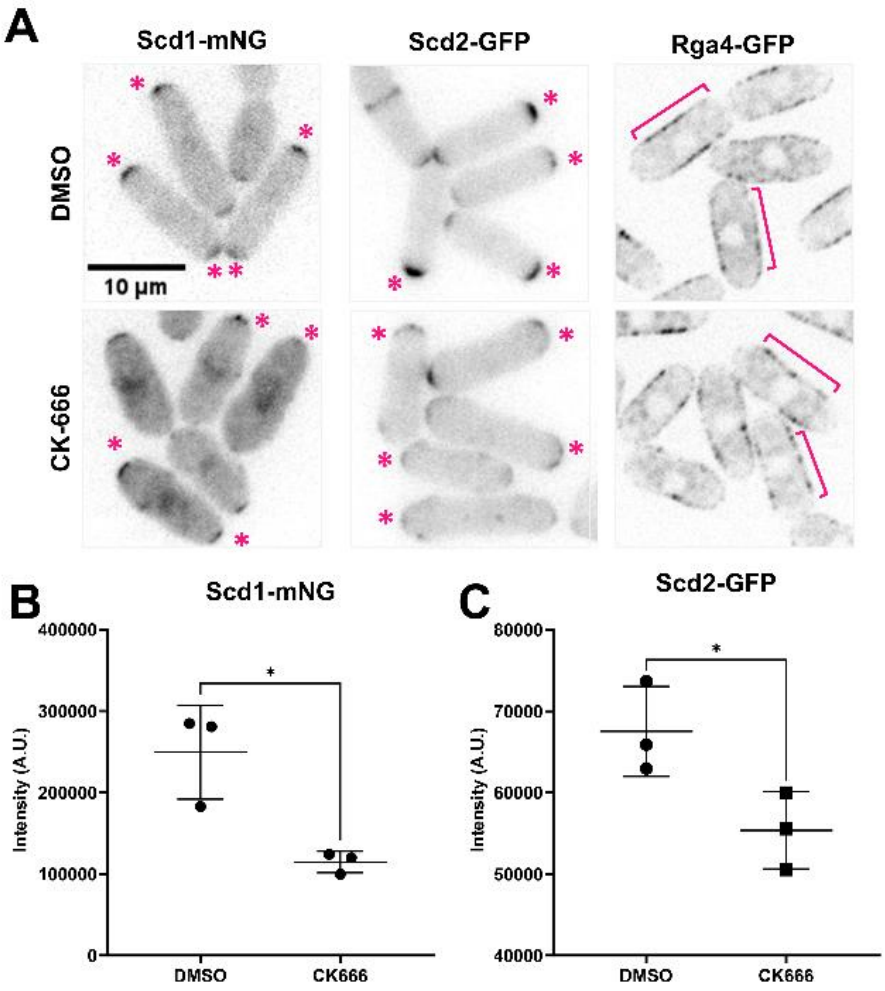

Figure 9. Proper Scd1 localization is lost when the Arp2/3 complex is inhibited. A. Localization of Scd1-mNG, Scd2-GFP and Rga4-GFP at the ends of DMSO and CK-666 treated cells. Magenta asterisks mark the site of Scd1-mNG and Scd2-GFP localization at the cell ends. Magenta brackets label Rga4-GFP along the cell sides. **B-C**. Quantification of Scd1-mNG and Scd2-GFP intensities at ends of DMSO and CK-666 treated cells. Scale bar, 10µm. n.s., not significant; p value, *<0.05, Student's t-test.

assumption and implemented a regulatory network (Model 1) describing Scd1-mediated Cdc42 activity cycle, an experimentally supported positive regulation of Scd1 by Cdc42-GTP, and a hypothetical, direct negative feedback loop between Cdc42-GTP and Scd1 (Negative feedback loop is required for oscillation) (**Fig.10A.i**.). In this ODE-PDE model, the two ends of the cell contain reactions at the membrane (**Fig.10A**), whereas the molecules in the cytoplasm or at the membrane on the sides are only allowed to diffuse [64]. The ODE-PDE model therefore has three

pools of Cdc42 and its regulators, one at each cell end and the third in the cytoplasm. We assign fixed concentrations of Cdc42 and the GEF Scd1, distributed between the three pools depending on their recruitment and detachment rates (**Fig.10B**). With 100,000 randomly sampled parameter values, this model failed to produce oscillatory dynamics observed experimentally (**Fig.10A.i, iii**, Model 1) (see Methods). This suggests that there is another regulator that is essential for oscillation. It was known that delayed negative feedback can produce oscillations without auto-catalysis [65]. Furthermore, membrane bound Scd1 inhibitors have been found experimentally [12]. We therefore introduced an additional unknown protein X to our model (**Fig.10A.ii**, Model 2). Protein X is activated/recruited by active Cdc42, and it inhibits the accumulation of Scd1 at the membrane, which gives rise to a delayed feedback loop. In contrast to Model 1, we found that 1.4% of randomly sampled parameter sets of Model 2 produced oscillation (**Fig.10A.iii**) (see Methods). Since Model 2 captured our experimental observations with respect to Cdc42 oscillatory dynamics, we used this model and a representative oscillation-enabling parameter set to further investigate the role of branched actin in establishing anticorrelation. We assumed that the detachment rate constants (δ) of each molecule positively correlate with endocytosis because branched actin in fission yeast is required for endocytosis. The scenario of branched actin disruption is described by reduced detachment rate constants in our model (i.e., decreased δ) (**Fig.10C.i**). To explore the influence of branched actin, we adjusted the detachment rate constants of Scd1, Cdc42, and protein X at the ends individually with the

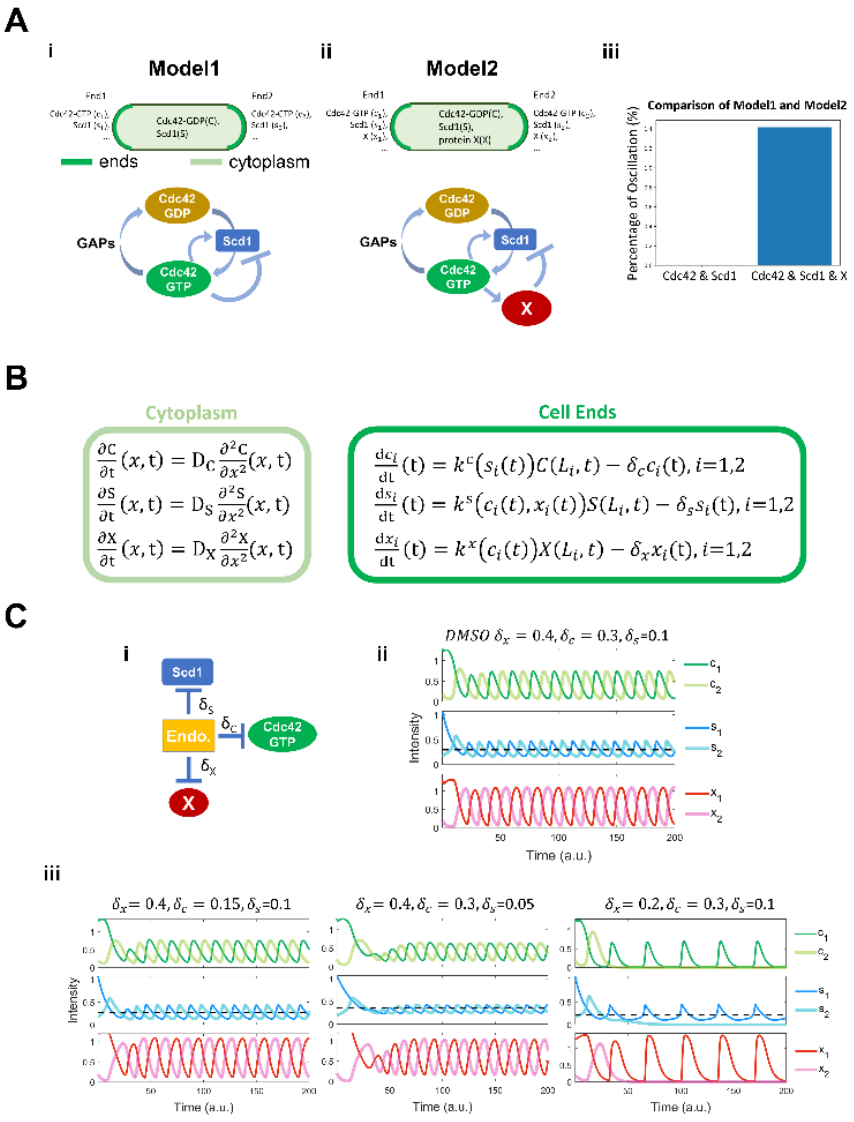

Figure 10. Models for bipolar and monopolar dynamics involving endocytosis. A. (i) Membranes at the cell ends accumulate Cdc42-GTP and Scd1, while the cytoplasm contains diffused Cdc42-GDP and Scd1. The panel below describes the Cdc42 activation network corresponding to Model1. Model1 incorporates feedback loops involving Cdc42-GTP, Cdc42-GDP, and GEF (Scd1), whereby the presence of Cdc42-GTP directly inhibits the membrane accumulation of GEF. (ii) Membranes at the cell ends accumulate Cdc42-GTP, Scd1, and an unknow protein X, while the cytoplasm contains diffused Cdc42-GDP, Scd1 and X. The panel below describes the Cdc42 activation network corresponding to Model2. Model2 incorporates feedback loops involving Cdc42-GTP, Cdc42-GDP, GEF (Scd1), and an unknown protein X, whereby the presence of Cdc42-GTP inhibits the membrane accumulation of GEF via protein X. (iii) A comparison between the percentage of oscillatory dynamics in Model1 and Model2. The number of parameter sets for 2 models is 100,000. **B.** Reaction-diffusion equations for Model2 (details in supplemental materials). Light green frame represents protein diffusion in cytoplasm, and dark green frame denotes protein production and degradation at the cell ends. **C.** (i) The effects of endocytosis on each protein in the Cdc42 activation network. (ii) Numerical results of the PDE-ODE simulations for Model 2. (iii) Numerical results for Model 2 obtained by varying the removal rates of each protein. The black dashed line is average concentration of Scd1 at the oscillatory dynamics tip. Initial conditions at each cell end 1 and 2: c1=1.3, c2=0.2, s1=1.07, s2=0.2, x1=1.3, x2=0.2 (c=Cdc42, s=Scd1, x= protein X).

representative parameter set in Model 2 (**Fig.10C**). We found that decreasing the detachment rates of Cdc42 dampened the overall signal of Cdc42 as well as the GEF Scd1 and factor X (**Fig.10C.iii**, left), but the steady state distributions of these molecules are symmetrical at the two ends. This bipolar distribution was also observed when Scd1 detachment rate was decreased (**Fig.10C.iii**, middle). The bipolarity was observed in a wide range of detachment rate constants (**Fig.S6A-B**). These simulations did not match our experimental observations of monopolar distribution upon loss of branched actin (**Fig.10**). In contrast, decreasing the detachment rate constant of factor X showed monopolar dynamics of Cdc42, Scd1 and factor X itself (**Fig.10C.iii**, right). Furthermore, we found that the mean level of Scd1 decreased with this perturbation, a phenomenon qualitatively reflected in our experiment (black dashed line in **Fig.10C.iii, and Fig.9B and C**). Overall, our simulation results showed that detachment of protein X (i.e., the Scd1 inhibitor) is important for maintaining cell bipolarity and Cdc42 oscillations at both ends.

The PAK kinase, Pak1, stabilizes when the Arp2/3 complex is inhibited.

Our model predicts that decreasing the detachment of the inhibitor X leads to asymmetric Cdc42 dynamics and decreased Scd1 at the cell ends. It has been reported that the Cdc42 effector kinase Pak1 is part of the time-delayed negative feedback and prevents Scd1 localization [28-30]. Thus, factor X could be Pak1 kinase in Model 2. Pak1 localization to the cell ends is dependent on active Cdc42 (**Fig.11A, B**). Cells with decreased active Cdc42 due to *scd1Δ* show a decrease in Pak1-mEGFP at the cell cortex (**Fig.11A**). In *gef1Δ* mutants Pak1-mEGFP is mostly monopolar, while in the *rga4Δrga6Δ* mutant Pak1-mEGFP at the cell cortex is enhanced (**Fig.11A**). Similar to active Cdc42 dynamics, Pak1-mEGFP displays anticorrelated oscillations between the two cells ends (**Fig.11D**) (Supp. Movie 3). We posit that when activated by Cdc42, Pak1 promotes

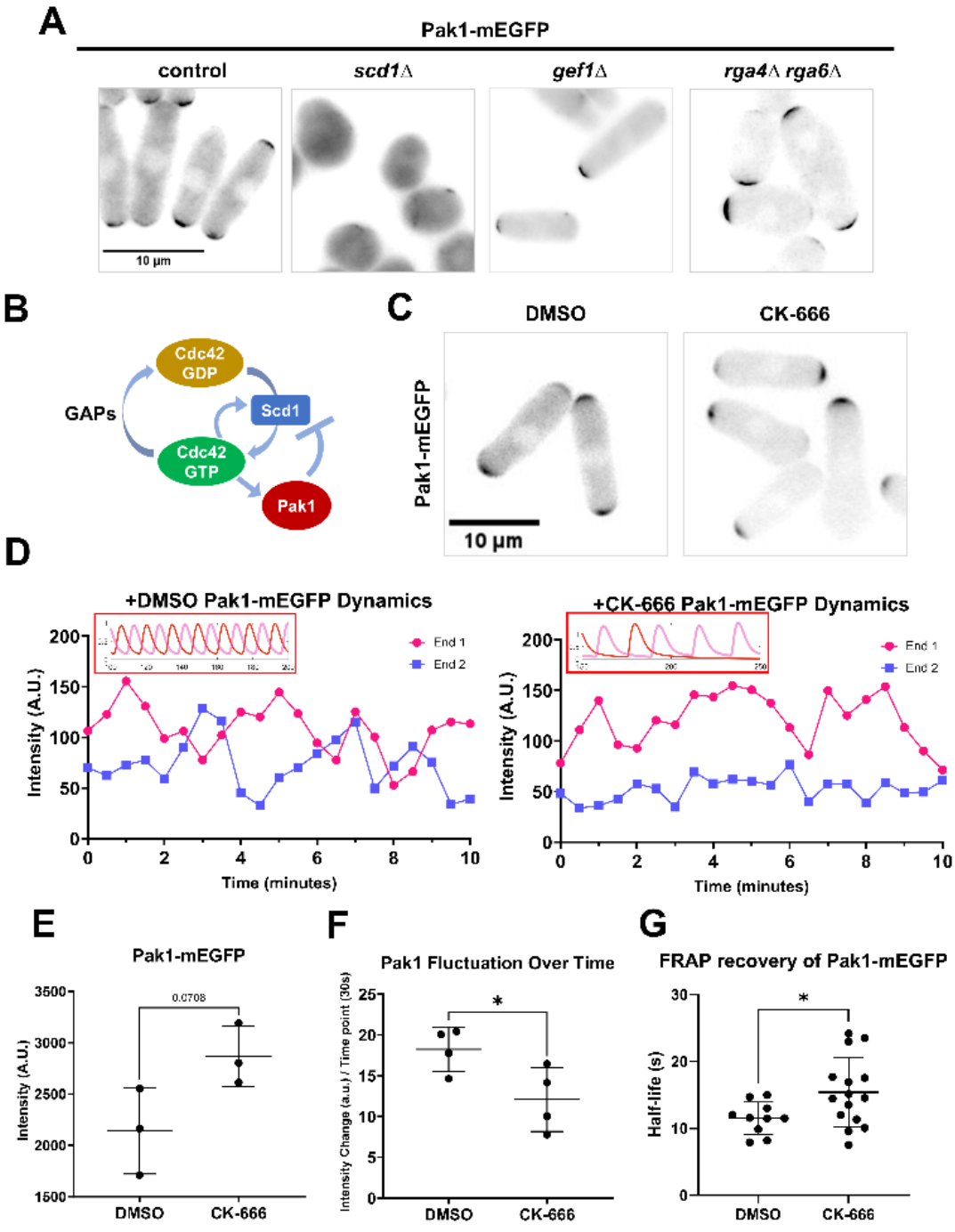

Figure 11. The Pak1 kinase, a potent inhibitor of Scd1, becomes more stable when branched actin is blocked. A. Model describing Cdc42 activation network where Pak1 kinase upon activation by Cdc42 triggers Scd1 removal. **B.** Pak1-mEGFP localization in DMSO and CK-666 treated cells. **C.** Pak1-mEGFP dynamics in cells with treated with DMSO or CK-666. Dynamics observed *in vivo* resembled the dynamics seen in model predictions (insets) **D.** Quantification of Pak1-mEGFP localization at the brightest cell end in DMSO or CK-666 treated cells. **E.** Quantification of the extent of Pak1-mEGFP fluctuations at the cell ends. **F.** FRAP showing the half-life of recovery for Pak1-mEGFP in DMSO and CK-666 treated cells. Scale bar, 10µm. p-value, *<0.05, Student's t-test.

endocytosis and this leads to its own displacement from the cell ends. Thus, we predict that in the absence of branched actin, Pak1 levels at the cell ends will stabilize and decrease in fluctuation. To test this, we used Pak1-mEGFP to visualize Pak1 localization and dynamics using timelapse microscopy (**Fig. 11C, D**). We find that upon CK-666 treatment, Pak1 dynamics at the cell ends resemble that of our model 2 with decreased detachment rate of factor X (**Fig.11D and Fig.10Ciii**). We next measured the intensity of Pak1-mEGFP at the cell ends in DMSO and CK-666 treated cells. In snapshot images we did not see a significant increase in Pak1-mEGFP levels upon CK-666 treatment, although we saw a trend in that direction (**Fig.11E**). However, when we analyzed Pak1-mEGFP dynamics at the cell ends over time we observed that it stabilizes with decreased fluctuations in CK-666 treated cells (**Fig.11C, D, F and S6A**). To further validate whether Pak1-mEGFP showed slower dynamics upon CK-666 treatment, we performed Fluorescence Recovery After Photobleaching (FRAP) in DMSO and CK-666 treated cells. We bleached one half of a cell end and quantified the return of fluorescence to that end. This allows us to measure the net arrival of new Pak1-mEGFP molecules to the region. FRAP shows that Pak1-mEGFP fluorescence recovery is significantly slower in CK-666 treated cells suggesting that Pak1-mEGFP dynamics are indeed slower upon inhibition of the Arp2/3 complex (**Fig. 11G**).

Our model predicts that stabilizing Pak1 kinase leads to decreased Scd1 levels at the cell ends. To test this, we investigated if Scd1 intensity would be impacted upon CK-666 treatment in the absence of Pak1 activity. To this end, we measured Scd1-mNG intensities in the hypomorphic *pak1* mutant *orb2-34* (*pak1-ts*) (**Fig.12A**). The *pak1-ts* mutant cells are monopolar and wider even at the permissive temperature (25ºC). Moreover, in keeping with previous reports, Scd1-mNG levels at the cell ends increases in *pak1-ts* mutant at permissive temperature (**Fig.12A, B**).

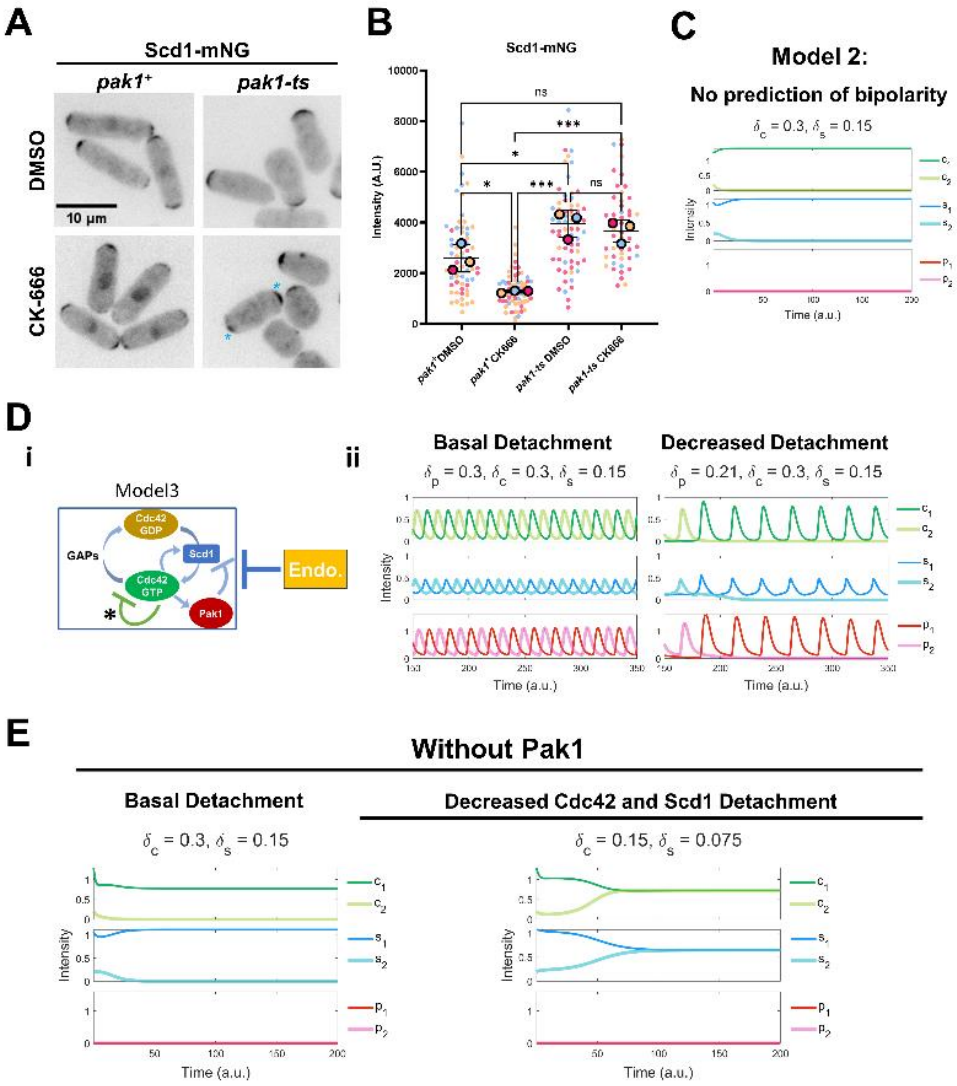

Figure 12. Loss of proper Scd1 localization is caused by Pak1 stabilizing. A. Scd1-mNG localization in *pak1+* and *pak1-ts* mutant cells. Blue asterisk depict bipolar Scd1-mNG localization. **B.** Quantification of Scd1-mNG intensities at the cell ends in *pak1+* and *pak1-ts* cells treated with DMSO and CK-666. Colors represent each replicate by day. Large circles are the means of each experimental replicate ($n \geq 10$ cells). **C.** (i) Model3 incorporates feedback loops involving Cdc42-GTP, Cdc42-GDP, GEF (Scd1), Pak1, and endocytosis, and an additional negative signaling pathway inhibiting Cdc42-GTP. (ii) Left panel shows Model3 simulations and the right panel shows simulations with decreased removal rate of Pak1. **D.** Model3 simulations with an additional negative signaling pathway simulated via decreased removal rate of Cdc42 and Scd1. Scale bar, 10µm. p-value, *<0.05, ***<0.0003, One way ANOVA, followed by Tukey's multiple comparison test.

We treated *pak1-ts* cells at permissive temperature with DMSO and CK-666 and compared Scd1-mNG intensity in these cells against *pak1+* controls under the same conditions. We find that Scd1-mNG intensity is not depleted in *pak1-ts* cells treated with CK-666 (**Fig.5A, B**). This suggests that the decrease in Scd1 levels observed in CK-666 treated cells is indeed due to Pak1 kinase activity. The *pak1-ts* cells are characteristically monopolar, however we unexpectedly find that around 40% of these cells treated with CK-666 showed bipolar localization of Scd1-mNG (**Fig.12A**, asterisks). The mechanism of this bipolar phenotype in the absence of Pak1 is not yet understood with our existing model: in Model 2, Pak1 (X in **Fig.10**) mediated negative feedback is essential for bipolarity (**Fig.12C**). We therefore included an additional, hypothetical negative feedback loop involving Cdc42 in our model (Model 3) (**Fig.12Di, ii**) (see details in supplementary materials). **Figure 5Dii** shows the simulation results of Model 3 under both standard and decreased detachment to replicate DMSO and CK666 conditions. We next ran simulations of Model 3 without Pak1 (p=0) (**Fig.12E**). As expected, the modeling shows monopolar dynamics in the absence of Pak1 (**Fig.12E**). However, the simulations captured bipolar phenotype when detachment rates of Cdc42 and Scd1 are reduced, suggesting that bipolar and monopolar phenotypes can coexist, and a heterogeneous response to CK-666 occurs in the absence of Pak1 (**Fig.12E**).

Pak1 accumulation at the cell ends lags behind Cdc42 activation.

Oscillatory patterning requires positive feedback and time-delayed negative feedback [66]. Cdc42 positive feedback comprises of Scd1 and Scd2 while negative feedback is mediated by the Pak1 kinase [18,21,67,68]. To this end, our model predicts that there is a spatiotemporal delay (phase shift) between the recruitment and peak accumulation of Cdc42 positive feedback proteins and the negative feedback protein, Pak1 at the growing cell ends (**Fig.13A**). Indeed, advancements in

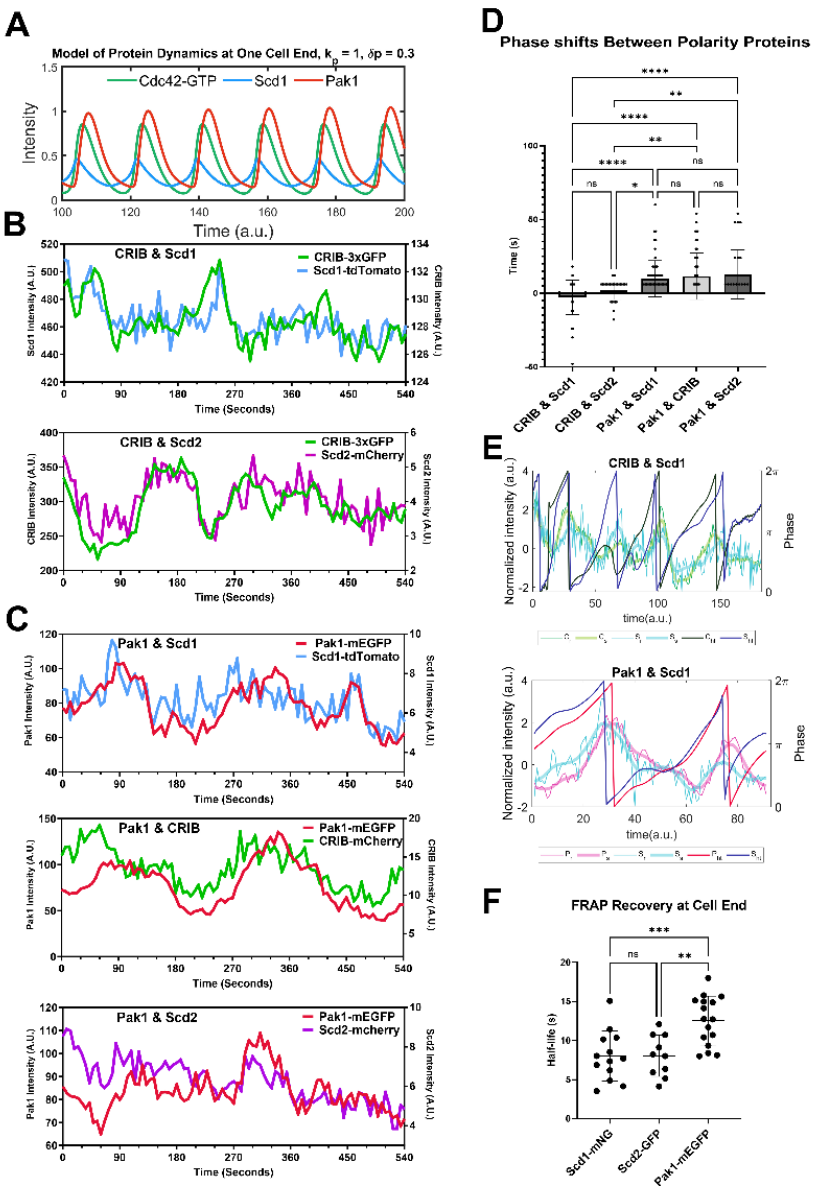

Figure 13. There is a difference in both recovery rate and the order of accumulation of Pak1 compared to positive polarity proteins at the cell end. A. Simulations of our models show a delay or phase shift between the peak accumulations of Cdc42-GTP and Pak1 at the growing end. **B.** Pairs of positive-feedback polarity proteins (CRIB-3xGFP and Scd1-tdTomato, CRIB-3xGFP and Scd2-mCherry) were simultaneously observed at the cell end. **C.** Each positive-feedback protein (Scd1-tdTomato, CRIB-mCherry, and Scd2-mCherry) was observed simultaneously with the negative-feedback protein, Pak1-mEGFP. **D.** The shift in time required to get the best correlation coefficient between signals from each pair of proteins was quantified using cross-correlation analysis. **E.** The Hilbert transform applied to the smoothened traces of Cdc42-GTP and Scd1 for their phase reconstruction and phase shift (Top). The Hilbert transform applied to the smoothened traces of Pak1 and Scd1 for their phase reconstruction and phase shift (Bottom). The thinnest traces represent normalized raw data, the thickest traces represent smoothened traces based on the normalized data, the darkest traces represent the phase progression achieved through Hilbert transform. **F.** FRAP showing the half-life of recovery for Scd1-mNG, Scd2-GFP and Pak1-mEGFP. n.s., not significant; p-value, **<0.005, ****<0.0001 ,One way ANOVA, followed by Tukey's multiple comparison test.

live cell microscopy have allowed for rapid timelapse imaging of even sparse proteins such as Scd1 *in vivo*.

To test this, we used strains with a combination of fluorescently tagged CRIB-3xGFP or CRIB-mCherry, Scd1-mNG or Scd1-tdTomato, Scd2-mCherry, and Pak1-mEGFP (**Fig.13B, C**). We find that there is practically no delay (average of 2 seconds) between positive feedback proteins such as CRIB-3xGFP & Scd1-tdTomato and CRIB-3xGFP & Scd2-mCherry (**Fig.13B, D and S7A**). However, there is an average delay of 12 seconds between the accumulation of positive feedback proteins (CRIB-mCherry, Scd1-tdTomato, or Scd2-mCherry) and the peak accumulation of Pak1-mEGFP (**Fig.13C, D and S7B**). We validated these results *in silico* (**Fig.13E**). The phase shift diagrams were generated using the Hilbert Transform of the normalized data of proteins at the ends. These analyses show both raw traces and transformed traces of the protein levels. The latter highlights the oscillatory cycle of pairs of proteins and assesses for any existing phase shifts (**Fig.13E**) [69]. As we expected the GEF Scd1-tdTomato peaks are in phase with those of active Cdc42 labeled by CRIB-3xGFP. Further, Pak1-mEGFP accumulation had a phase shift with respect to Scd1-tdTomato accumulation.

Current reports suggest that Pak1 kinase localization to the cell cortex is entirely dependent on active Cdc42. This would suggest that Pak1 kinase dynamics would be similar to that of Cdc42 activation. However, we find that Pak1 kinase shows delayed accumulation compared to active Cdc42, Scd1, and Scd2. This suggested that Pak1 dynamics are slower than that of Cdc42 activation. We tested this idea by modifying the model and experimentally measuring Pak1 dynamics. To verify if Pak1 accumulation was indeed slower than that of Cdc42 we increased the accumulation and detachment rates of Pak1 in our models. We find that with increasing rates the oscillations dampen and phase shifts reduce to a minimal value but do not completely disappear.

Furthermore, with decreasing phase shift the oscillations are ultimately extinguished (**Fig.S8**). The observed phase shift, or delay, between the peak accumulations of Cdc42 and Pak1 at cell ends is primarily attributed to the inherent time required for cellular processes. This encompasses the time needed for their diffusion, subsequent accumulation, and detachment.

Next, we compared FRAP recovery dynamics of Pak1-mEGFP with that of Scd1-mNG and Scd2-GFP. The transient binding of the CRIB-3xGFP reporter makes it unsuitable for FRAP analysis. Furthermore, measuring the dynamics of total Cdc42 will not distinguish between active and non-active Cdc42. Our data (**Fig. 13D**) shows that accumulation of active Cdc42, as indicated by CRIB-3xGFP, is similar to that of Scd1-mNG and Scd2-GFP. Thus, we used Scd1-mNG and Scd2-GFP as proxies for Cdc42 activity and compared their dynamics to Pak1-mEGFP. We find that the half-life of Pak1-mEGFP fluorescence recovery is significantly slower than the fluorescence recovery of Scd1-mNG and Scd2-GFP (**Fig. 13F**). This indicates that the dynamics and net recruitment of Pak1 kinase is slower than active Cdc42, Scd1 and Scd2.

Loss of the Arp2/3 regulator *myo1* disrupts Cdc42 oscillatory dynamics.

Next, we validated if the Cdc42 oscillation defects in CK-666 treated cells are due to loss of endocytosis. Endocytosis is an essential cellular process and most endocytic mutants show severe cell growth and polarity defects thus complicating such an analysis. The Arp2/3 complex regulator *myo1* is not essential and loss of *myo1* results in shape and growth defects but these cells are still able to polarize [47]. Thus, we used the *myo1Δ* mutant to investigate Cdc42 oscillatory dynamics. We find that *myo1*Δ mutants show similar defects in Cdc42 oscillatory dynamics to those observed in CK-666 treated cells (**Fig.14A, B**). We observed Cdc42 oscillations in *myo1+* and *myo1Δ* mutants expressing CRIB-3xGFP. Normally, cells show anticorrelated CRIB-3xGFP oscillations with a correlation coefficient of about -0.5 (**Fig.14B**). In

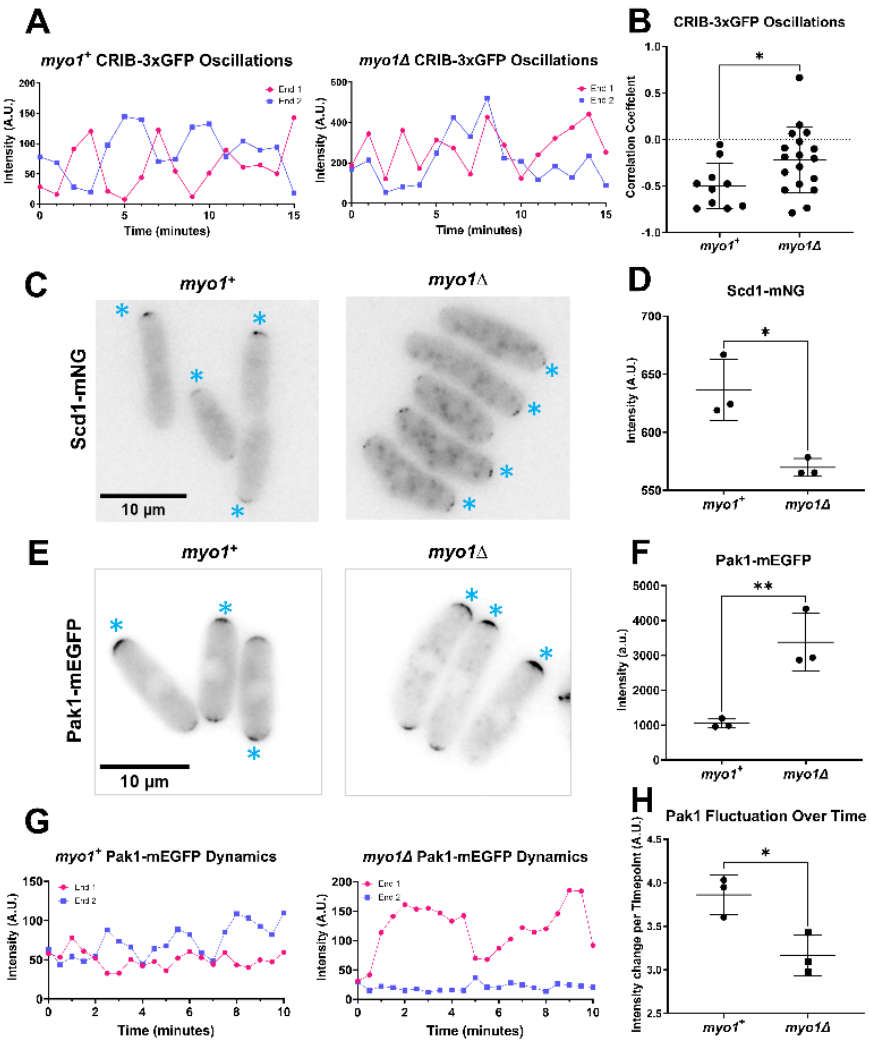

Figure 14. Endocytic mutant *myo1*Δ cells show disrupted Cdc42 activation dynamics similar to CK-666 treatment. A. CRIB-3xGFP dynamics were observed in *myo1*+ and *myo1*Δ cells. **B**. Correlation coefficients of active Cdc42 oscillations between cell ends in *myo1*+ cells and *myo1*Δ mutants. **C**. Scd1-mNG localization in *myo1*+ and *myo1*Δ cells. Asterisks indicate Scd1-mNG localization at the brighter cell end. **D**. Quantification of Scd1-mNG accumulation at cell ends in *myo1*+ and *myo1*Δ cells. **E.** Pak1-mEGFP localization in *myo1*+ and *myo1*Δ cells. Asterisks indicate Pak1-mEGFP localization at the brighter cell end **F.** Quantification of Pak1-mEGFP accumulation at cell ends in *myo1*+ cells and *myo1*Δ mutants. **G.** Pak1-mEGFP dynamics at cell ends in *myo1*+ and *myo1*Δ cells. **H.** Quantification of the extent of Pak1-mEGFP fluctuation in *myo1*+ and *myo1*Δ cells. Scale bar 10μm. p-value, *<0.05, **<0.0085, Student's t-test.

myo1Δ cells CRIB-3xGFP signals at the cell ends continued to fluctuate but displayed an average correlation coefficient of about -0.2 indicating a decrease in anticorrelation (**Fig.14B and S9B**).

Next, we compared the localization of Scd1-mNG at the cell ends in *myo1*+ and *myo1Δ* cells.

Similar to CK-666 treated cells, *myo1Δ* mutants showed a decrease in Scd1-mNG levels at the cell ends (**Fig.14C, D**). We also observed increased monopolar localization of Scd1-mNG at the cell ends in *myo1Δ* mutants. Our results with CK-666 treated cells suggest that loss of Scd1 levels at the cell ends is due to the stabilization of Pak1 kinase at those ends. Thus, we analyzed Pak1-mEGFP levels and dynamics at the cell ends in *myo1Δ* mutants. We find that in *myo1Δ* mutants Pak1-mEGFP levels at the cell ends increase (**Fig.14E, F**). We observed Pak1-mEGFP dynamics using timelapse imaging in *myo1+* and *myo1Δ* cells. Pak1-mEGFP localization mostly appeared at one cell end and displayed decreased fluctuations over time in *myo1Δ* cells (**Fig.14G, H and S9B**). This suggests that, similar to CK-666 treated cells, Pak1 dynamics at the cell ends stabilized in *myo1Δ* cells. Together, these data suggest that efficient endocytosis is required for proper Cdc42 activity between the cell ends.

Endocytic events deplete Pak1 from the membrane.

Our data suggests that the Arp2/3 complex is required for Pak1 removal to allow Scd1 localization and anticorrelated oscillations for Cdc42 between the cell ends. As a result, we hypothesize that Pak1 is depleted from the cell end via endocytosis. Pak1 kinase has been shown to phosphorylate Myo1 for endocytosis. Thus, we posit that Pak1 kinase molecules overlapping with the endocytic patches are removed via

endocytosis. To test this, we first investigated the spatial organization of Pak1 at the cell ends. Our investigations show that Pak1-mEGFP is not evenly distributed as a cap rather, Pak1 localizes as distinct puncta at the cell ends. (**Fig.15A**). Next, we asked if these puncta overlapped with sites of endocytosis.

Endocytic patches in fission yeast can be detected using the actin crosslinking protein Fimbrin, Fim1 [70]. Fim1 specifically localizes to branched actin patches and internalizes into the cytoplasm

with the endocytic patches during endocytosis [70]. We find that the Pak1-mEGFP puncta colocalize with Fim1-mCherry labelled endocytic patches at the plasma membrane (**Fig.15A**). Next, we analyzed Fim1-mCherry internalization in cells co-expressing Pak1-mEGFP. We observe that while the Fim1-mCherry labeled endocytic patch internalizes into the cytoplasm, Pak1-mEGFP does not (**Fig.15A**). However, we find that Pak1-mEGFP puncta overlapping with Fim1-mCherry is lost from the plasma membrane when the endocytic patch internalizes (**Fig.15A**). Most endocytic proteins are known to internalize with the patch. However, several regulators of endocytosis do not internalize but are simply lost from the membrane when the patch internalizes. In fission yeast, the endocytic proteins such as the F-BAR containing Cdc15 and Myo1 are lost from the membrane upon patch internalization [71,72]. In mutants with a delay in patch internalization, loss of these proteins from the plasma membrane is also delayed [42]. It is possible that local puncta of Pak1 show a similar loss at the membrane during patch internalization. To test this, we measured the intensity of Fim1-mCherry and Pak1-mEGFP simultaneously at the plasma membrane. We observe that each time Fim1-mCherry starts to internalize (**Fig.15C**, dashed lines), Pak1-mEGFP decreases at the plasma membrane as indicated by reduced Pak1-mEGFP intensity at the membrane (**Fig.15A, B and C**). Next, we quantified when Pak1-mEGFP was lost from the membrane compared to Fim1-mCherry

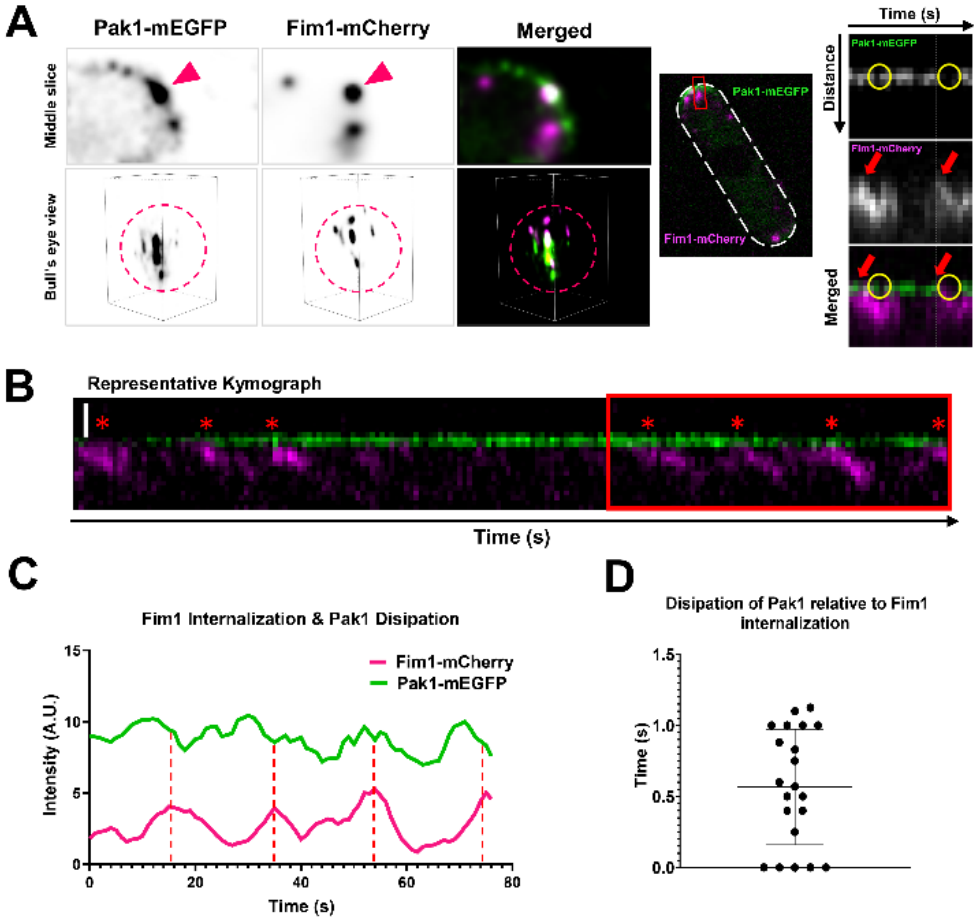

Figure 15. Endocytosis plays a role in removing Pak1 from cell ends. A. Fim1-mCherry and punctate Pak1-mEGFP localization at cell ends. Middle panel shows a whole cell with a white dashed outline. Red box marks the region shown as kymographs in the right panels. Yellow circles mark Pak1-mEGFP loss from the membrane while red arrows mark the onset of Fim1-mCherry internalization at the membrane **B.** Kymograph of Pak1-mEGFP and Fim1-mCherry as captured in a 3-minute timelapse movies with 1 second intervals. Red box marks the region quantified in C. **C.** Quantification of Pak1-mEGFP and Fim1-mCherry intensities at the membrane over time. Red dashed lines indicate the peak and subsequent drop of Fim1-mCherry intensity. **D.** Quantification of the time taken for dissipation of Pak1-mEGFP relative to Fim1-mCherry internalization. (n ≥6 endocytic events per kymograph, N= 21 kymographs from 3 experiments) Representative images of the cell tip are clarified and denoised, made in NIS elements.

internalization (**Fig.15C, D**). We find that, on average, Pak1-mEGFP is lost from the membrane within 1 second of Fim1-mCherry internalization (**Fig.15C, D**). This suggests that Pak1 is removed from cell ends when the endocytic patch internalizes.

Pak1 activity promotes successful internalization of endocytic patches.

While the role for Pak1 kinase in endocytosis has not been fully investigated, it has been shown to phosphorylate Myo1 for endocytosis [47,73]. Given the importance of endocytic events for depleting Pak1 from cell ends and Pak1 colocalization with endocytic patches at the membrane, we next wanted to

investigate the relationship between Pak1 activity and endocytosis. Thus, we hypothesized that the Pak1 kinase is required for endocytosis. To test this, we analyzed endocytic dynamics in the absence of Pak1 kinase. The *pak1-ts* mutant, *orb2-34,* shows polarity defects even at its permissive temperature of 25°C. We find that successful endocytic events are significantly reduced in *pak1-ts* mutants (**Fig.16B, E**) at 25°C. Fim1-mEGFP was used to specifically visualize endocytic patches. We observe that endocytic patches still

form at the membrane in *pak1+* and *pak1-ts* cells and their lifetime at the cell membrane remains the same **(Fig.16B, C**). Thus, Pak1 does not influence the ability of endocytic patches to form. Endocytic patches that internalize >350 nm away from the membrane are considered to have undergone successful scission from the plasma membrane [74]. We find that there is a significant decrease in the overall distance that patches internalize in *pak1-ts* mutants compared to *pak1+* cells (**Fig.16B, D**). Furthermore, a higher fraction of the patches in *pak1-ts* mutants did not internalize beyond 350nm indicating a greater fraction of failed endocytic events compared to *pak1+* cells (**Fig.16B, E**). In addition, patches that do not properly internalize show three types

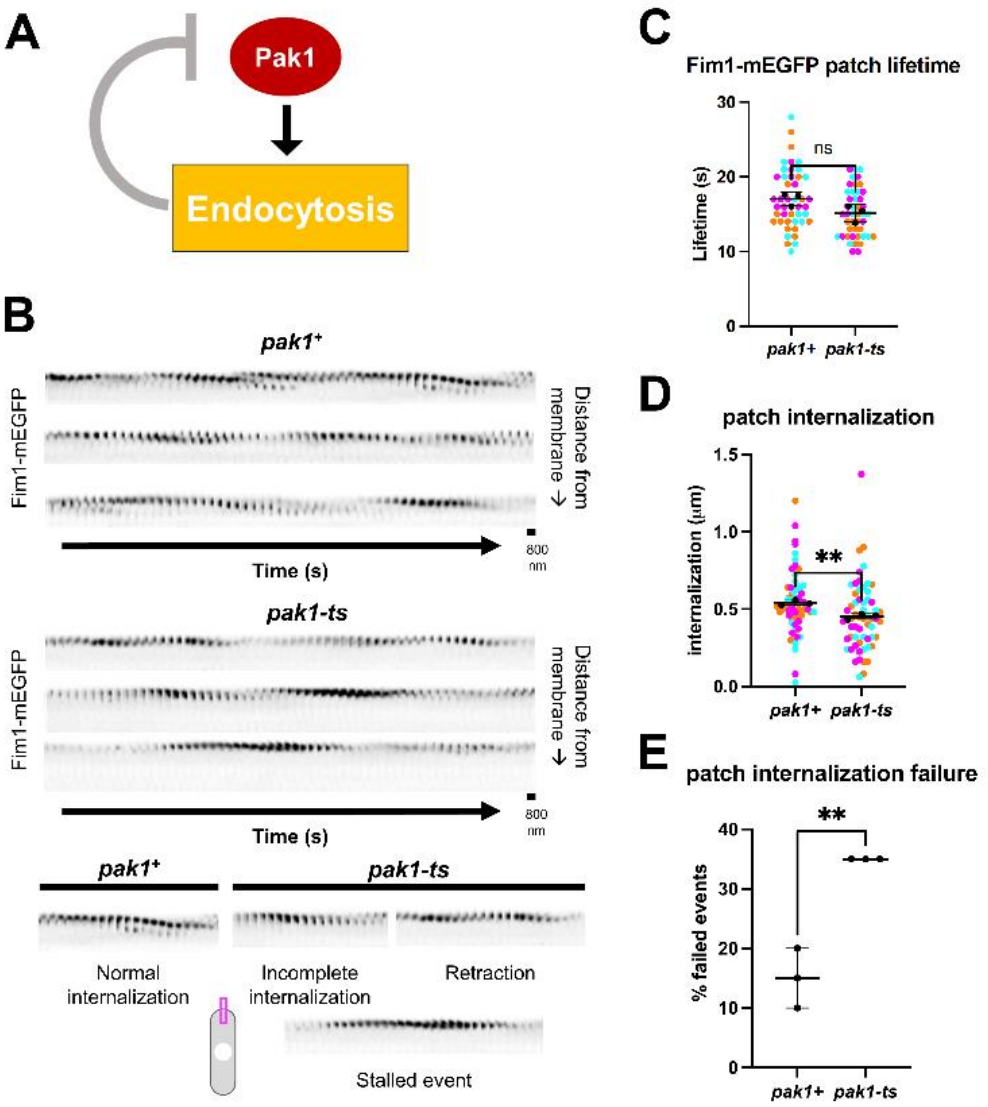

Figure 16. Pak1 plays a role in promoting endocytosis. A. Schematic depicting our hypothesis that Pak1 activity promotes its own removal through endocytosis. **B.** Montages of Fim1-mEGFP labeled endocytic patches at growing ends of interphase *pak1*$^{+}$ and *pak1-ts* cells (scale bars = 800 nm; frame rates = 1 second per frame (SPF)). **C.** Quantification for lifetimes of Fim1-mEGFP labeled endocytic patches in *pak1*$^{+}$ and *pak1-ts* (n=15 endocytic patches per experiment, N=3 experiments). **D.** Quantification of Fim1-mEGFP labeled endocytic patch internalization into the cell interior from the plasma membrane in *pak1-ts* mutants compared to *pak1*$^{+}$ cells (n=20 endocytic patches per genotype per experiment, N=3 experiments). E**.** Quantification of failed endocytic events in *pak1*$^{+}$ cells compared to *pak1-ts.* Failed events do not internalize beyond 350 nm from the plasma membrane (n=20 endocytic patches per genotype per experiment, N=3 experiments). Symbol colors in graphs = distinct experiments. Solid symbols = means of experiments. n.s., not significant; p-value, **<0.01, Student's t-test.

of failed endocytic events such as incomplete internalizations, patch retractions, or stalled events (**Fig.16B**).

Discussion

While Cdc42 activation spatiotemporally regulates actin organization for membrane trafficking and polarized growth, it is not well understood how Cdc42 itself is dynamically regulated. In fission yeast, Cdc42 and its regulators undergo oscillatory dynamics between the two cell ends, and this lends itself to dynamic regulation of actin organization [13,17,46,56,75,76]. However, the molecular details of how these proteins undergo oscillatory dynamics are not clear. At each cell end, Cdc42 activation occurs via positive feedback and a time-delayed negative feedback resulting in the oscillatory pattern [11,17,46,59,63,64,77,78]. The molecular details of how each cell-end overcomes this negative-feedback to allow reactivation of Cdc42 at that end is not known. Here we find that endocytosis enables periodic reactivation of Cdc42 at the cell ends by removing the negative-feedback and allowing the Cdc42 GEFs to return to that end.

Arp2/3 dependent endocytosis is known to be required for growth in *S. pombe* and other fungal species as well as mammalian cells with high membrane tension [74,79,80]. Previous works show that Arp2/3 dependent endocytosis is required to overcome the high internal turgor pressure for proper polarization and growth in yeasts [79,81]. Here, we expound upon the importance of Arp2/3 dependent endocytosis for proper spatiotemporal regulation of polarity factors. We show that adequate removal of inhibitors is critical for proper polarized growth. Indeed, our lab has previously reported the importance of Rga4 removal for proper cell cycle progression and resumption of growth [82]. While previous works have described how exocytosis dilutes polarity protein concentration and dampens the concentration of active Cdc42 at that site, our work finds that endocytosis promotes Cdc42 activity through the removal of inhibition [52,83]. Interestingly,

we also find that Pak1 is required for normal endocytic patch dynamics. We hypothesize that Cdc42 activity promotes endocytosis through downstream regulators such as Pak1 and will investigate this further in future works.

The time-delayed negative feedback in Cdc42 regulation is mediated by its effector kinase Pak1 [11,17,26,29,30,36]. Here we show that impeding endocytosis either by inhibition of the Arp2/3 complex or by deletion of *myo1* results in Pak1 accumulation at the cell ends. This suggests that endocytosis promotes Pak1 removal from the cell ends. Without Pak1 removal, Scd1 cannot localize to activate Cdc42, and, without further Cdc42 activation, the cell ends fail to compete for resources. Pak1 removal enables Scd1 localization to the cell ends and allows for proper Cdc42 activation dynamics between the two cell ends. Thus, endocytosis is required for maintaining anticorrelated Cdc42 activation dynamics between the cell ends thus promoting bipolar growth. Previous models have demonstrated the need for negative regulation on active Cdc42 for its oscillations [11,13,26,64]. However, these models did not explore the impact of endocytosis on active Cdc42 dynamics and cell polarity. In this study, we developed models to illustrate how the accumulation of active Cdc42 hinders the buildup of Scd1 through the excess accumulation of Pak1 on the cellular membrane. Additionally, we found that endocytosis allows cellular bipolarity by facilitating the removal of Pak1.

While active Cdc42 is required for polarized growth, it is possible to have too much of a good thing. Absence of negative feedback, due to the loss of Pak1 activity, leads to an abundance of positive feedback at the dominant end. Thereby, Cdc42 activation at the dominant end is too strong for the second end to compete against, resulting in aberrant rounded morphology and monopolar growth as observed in *pak1-ts* mutants [11,84]. We find that inhibition of the Arp2/3 complex due to CK-666 treatment or *myo1Δ* leads to enhanced negative feedback due to

stabilization of Pak1 at the cell ends. This enhanced negative feedback results in monopolar Cdc42 activity and growth is inhibited at the site where Pak1 stabilizes. Positive feedback leads to Cdc42 activation which, in turn, allows Pak1 activation and time-delayed negative feedback. We report that Pak1 plays a role in promoting endocytosis (**Fig.16**). Our findings show that disruption of negative feedback via endocytosis-dependent Pak1 removal enables the return of positive feedback to the same cell end.

pak1-ts cells are characteristically monopolar. However, we observe that *pak1-ts* cells can localize Scd1 in a bipolar manner in a fraction of the cells, upon CK-666 treatment. We hypothesize that this may be explained by a secondary form of negative regulation mediated by Arp2/3 complex that is still unknown. As per Model 3, bipolar Scd1 in the absence of Pak1 occurs when Scd1 at the end is stabilized. It is possible that endocytosis partially contributes to Scd1 removal by an unknown mechanism and this is observable only in the absence of Pak1 kinase. Further research will investigate the mechanism of this second negative regulation. One possibility could be that endocytosis leads to changes in the levels of proteins at the cortex thus altering Cdc42 activation. Alternately, endocytosis may alter the lipid composition of the plasma membrane thereby affecting Cdc42 activation.

While the functions and localizations of Cdc42 and its regulators have been extensively studied, the spatiotemporal localization (phase shifts) among these proteins had not been shown *in vivo*. Previous work has elucidated phase shifts among polarity factors, ion signaling, and growth in pollen tubes [78,85,86]. *In vitro* experiments using *Xenopus* frog egg extracts and protein reconstituted systems have also shown phase shifts between waves of Rho GTPase activity and actin polymerization [46,75]. Our data show that the accumulation of active Cdc42 is in phase with the recruitment of its activator Scd1 but, by contrast, the accumulation of Pak1 shows a phase

delay relative to the positive regulators. The phase shift between Pak1 and the positive regulators likely results from its multiple roles and step wise regulation of both Pak1 kinase and active Cdc42. In vitro investigations show that active Cdc42 physically binds and activates Pak1 kinase at the plasma membrane. However, the dynamics of Cdc42-dependent Pak1 recruitment at the cell ends has not been fully investigated. These phase shifts suggest that Pak1 kinase can remain at the membrane at least for a small period of time after the loss of active Cdc42. Indeed, we find that Pak1 dynamics at the membrane are slower than that of the Cdc42 activators Scd1 and Scd2. It is unknown if Pak1 once recruited still needs to or even can keep binding active Cdc42 once it interacts with downstream substrates. Further investigations will explore the nature of these interactions and dynamics. Overall, our data suggests that the inhibitory role of increasing Pak1 activity causes a gradual decrease in its own recruitment until, eventually, Pak1 removal rate exceeds recruitment rate. This intrinsic delay is further evidence of the complexity of self-organized processes and the multiple mechanisms in cell polarity.

Self-organization is seen throughout biology as a means to precisely regulate cellular processes [87]. Our work furthers the understanding of Cdc42's extensive self-organizing capabilities [18,88,89]. Our findings show that the Cdc42 regulatory complex along with actin-mediated endocytosis form a self-organizing unit in the regulation of cell polarity. Complex signaling pathways with higher order molecular feedbacks have been observed in several processes and systems [87,90-93]. In nature, robustness is important but cannot come at the expense of adaptability or vice versa. These higher order pathways allow for adaptability while maintaining robustness. The RHO family GTPases undergo higher-order pathways via multiple feedback loops and this allows for their precise spatiotemporal activation necessary for cell polarization [6,18,94-97]. Our findings on Cdc42 regulation define higher order signaling pathways with multiple feedback loops and

ensures polarized growth at each cell end which allows for bipolarity. While the role for Cdc42 regulating membrane trafficking is well documented, here we show how membrane trafficking also contributes to Cdc42 regulation and maintenance of bipolar growth.

Materials and Methods

Strains and cell culture

The S. pombe strains used in this study are listed in **Table S1**. All strains are isogenic to the original strain PN567. Cells were cultured in yeast extract (YE) medium and grown exponentially at 25°C, unless specified otherwise. Standard techniques were used for genetic manipulation and analysis [98]. Cells were grown exponentially for at least three rounds of eight generations each before imaging.

Microscopy

Imaging was performed at room temperature (23–25°C). We used an Olympus IX83 microscope equipped with a VTHawk two-dimensional array laser scanning confocal microscopy system (Visitech International, Sunderland, UK), a Hamamatsu electron-multiplying charge-coupled device digital camera (Hamamatsu EM-CCD Digital Camera ImageM Model: C9100-13 Serial No: 741262, Hamamatsu, Hamamatsu City, Japan) and a 100×/1.49 NA UAPO lens (Olympus, Tokyo, Japan). Images were acquired using MetaMorph (Molecular Devices, Sunnyvale, CA). We also used a spinning disk confocal microscope system with a Nikon Eclipse inverted microscope with a 100×/1.49 NA lens, a CSU-22 spinning disk system (Yokogawa Electric Corporation) and a Photometrics EM-CCD camera (Photometrics Technology Evolve with excelon Serial No: A13B107000). Images were acquired using MetaMorph (Molecular Devices, Sunnyvale, CA).

Additionally, we used a Nikon Ti2 Eclipse wide field microscope with a 100x/1.49 NA objective, an ORCA-FusionBT digital camera (Hamamatsu Model: C15440-20UP Serial No: 500428, Hamamatsu, Hamamatsu City, Japan). Images were acquired using Nikon NIS Elements (Nikon, Melville, NY). Fluorophores were excited using an AURA Light Engine system (Lumencor, Beaverton, OR).

Microscopy was also performed with a 3i spinning disk confocal using a Zeiss AxioObserver microscope with integrated Yokogawa spinning disk (Yokogawa CSU-X1 A1 spinning disk scanner) and a 100x/1.49 NA objective. Images were acquired with a Teledyne Photometrics Prime 95b back-illuminated sCMOS camera (Serial No: A20D203014, Tucson, AZ). Images were acquired using SlideBook (3i Intelligent Imaging innovations, Denver, CO).

Acquiring and quantifying fluorescence intensity

Fluorescence intensity was measured using ImageJ software. All images were sum projected and mean intensities were reported. Freehand ROIs were used to measure signal at the cell ends. For analysis of two ends of the same cell, cytoplasm with little or no signal was used for background subtraction. For all other experiments, a region outside of the cell was used for background subtraction. The mean intensity was measured and recorded after the background subtractions.

To quantify the anticorrelation between two ends, cells in each condition were imaged every minute for 60 minutes. The data from each cell was then analyzed to find the correlation coefficient between fluorescent signals of both ends within the cell.

To quantify signal stability at the cell ends, cells were imaged every 30 seconds for 20 minutes. The stability of the proteins was then quantified by measuring the difference in intensity between each subsequent timepoint for the duration of the timelapse imaging. Populations that had larger

average variations of fluorescent intensity between each timepoint were more dynamic and less stable than populations that had smaller variations between each timepoint.

To observe and quantify the in vivo phase-shifts, cells were imaged every 6 seconds for 9 minutes. Two fluorescent proteins were imaged simultaneously using the 488 nm and 561 nm wavelengths. LED power was set to 3% for each wavelength. Standard fluorescence intensity method was used to measure each timepoint. The phase-lag between each protein at each cell end was then quantified using cross-correlation analysis wherein the correlation coefficient is calculated for both signals with and without shifting the quantified signal. The second fluorescent signal is shifted backwards by 20 timepoints while the first signal remains the same and the correlation coefficient is calculated for each shift. The correlation coefficient is also calculated as the signal is shifted forward by 20 timepoints and calculated for each shift. The number of shifts required to achieve the best correlation coefficient indicates how far one signal lags the other. The shift required to produce the best correlation between the two fluorescent signals was verified as showing true correlation or not before being included in the final comparative analysis for each set of protein signals.

For FRAP analysis, cells were imaged for every 250ms for 30 seconds with 15% laser power. Square ROIs were used to target, bleach, and measure the fluorescence intensity at half of one cell end as it was bleached and subsequently allowed to recover. Bleaching was performed on the 10^{th} timepoint using two 150ms bleach repetitions at 5% laser power. The half-life of fluorescence recovery was quantified in using SlideBook FRAP analysis software.

To observe the loss of Pak1 from the cell membrane in relation to the internalization of Fim1, cells were imaged each second for 3 minutes. Rectangular ROIs were used to isolate regions of the cell end for analysis. These ROIs were used to make kymographs of both Fim1-mCherry

signal and Pak1m-EGFP signal. These kymographs were quantified by plotting the intensity profile of both proteins at the cell membrane. These intensity profiles were then analyzed by recording when Pak1 was lost in comparison to each successful endocytic event. Between 6-10 endocytic events were captured in each kymograph. These events were then averaged for each kymograph and graphed.

Actin cytoskeleton disruptions

Cells were treated with 100 μM CK-666 (Sigma-Aldrich, SML006-5MG) in DMSO (Sigma-Aldrich, D8418-250ML) to block the Arp2/3 complex and branched actin assembly. To block the polymerization of all F-actin structures, cells were treated with 10 μM Latrunculin A (LatA; EMD Millipore) dissolved in DMSO for 30 minutes prior to imaging. Control cells were treated with 0.1% DMSO in YE media.

Statistical tests

Significance was determined using GraphPad Prism. When comparing two conditions, a Student's t-test was used (two-tailed, unequal variance). One way ANOVA, followed by a Tukey's multiple comparison test, was used to determine significance for experiments with three or more conditions.

Mathematical models for regulation networks

The details of the regulatory network are provided in the supplementary materials. This paper introduces three networks, all described using a reaction-diffusion model based on the Xu-Jilkine model [64]. Model 1 and Model 2 each include one negative regulatory pathway of active Cdc42. In Model 1, there is a direct inhibition from active Cdc42 to Scd1. In Model 2, the negative pathway involves Pak1. Model 3, on the other hand, includes two negative regulatory pathways

of active Cdc42, with one involving Pak1. However, the details of the second pathway remain unclear. For the numerical analysis, MATLAB was used.

Computational phase analysis

Z-scores were used to normalize the data. Prior to analysis, the normalized data was smoothened, and the Hilbert Transform of the data was applied using MATLAB.

Declaration of Interests

The authors declare no competing or financial interests.

Acknowledgements

We thank James Moseley and Vladimir Sirotkin for providing strains and Bret Judson at Boston College Imaging core for imaging support. We thank Guangyuan Liao for helping with the MATLAB code.

Funding

This work is supported by the National Institutes of Health grant R01GM136847 to M.D. T.H. is supported by the National Institutes of Health grant R35GM149531.

References

1 Drubin, D. G. & Nelson, W. J. Origins of Cell Polarity. *Cell* **84**, 335-344 (1996). https://doi.org/10.1016/s0092-8674(00)81278-7

2 Glotzer, M. & Hyman, A. A. Cell Polarity: The importance of being polar. *Current Biology* **5**, 1102-1105 (1995). https://doi.org/10.1016/s0960-9822(95)00221-1

3 Nobes, C. D. & Hall, A. Rho GTPases control polarity, protrusion, and adhesion during cell movement. *J Cell Biol* **144**, 1235-1244 (1999). https://doi.org/10.1083/jcb.144.6.1235

4 Etienne-Manneville, S. Cdc42--the centre of polarity. *J Cell Sci* **117**, 1291-1300 (2004). https://doi.org/10.1242/jcs.01115

5 Manser, E., Leung, T., Salihuddin, H., Zhao, Z. S. & Lim, L. A brain serine/threonine protein kinase activated by Cdc42 and Rac1. *Nature* **367**, 40-46 (1994). https://doi.org/10.1038/367040a0

6 Martin-Vilchez, S. *et al.* RhoGTPase Regulators Orchestrate Distinct Stages of Synaptic Development. *PLoS One* **12**, e0170464 (2017). https://doi.org/10.1371/journal.pone.0170464

7 Machacek, M. *et al.* Coordination of Rho GTPase activities during cell protrusion. *Nature* **461**, 99-103 (2009).

8 de Beco, S. *et al.* Optogenetic dissection of Rac1 and Cdc42 gradient shaping. *Nat Commun* **9**, 4816 (2018). https://doi.org/10.1038/s41467-018-07286-8

9 Mitchison, J. M. & Nurse, P. Growth in cell length in the fission yeast Schizosaccharomyces pombe. *J Cell Sci* **75**, 357-376 (1985). https://doi.org/10.1242/jcs.75.1.357

10 Johnson, D. I. Cdc42: An essential Rho-type GTPase controlling eukaryotic cell polarity. *Microbiol Mol Biol Rev* **63**, 54-105 (1999). https://doi.org/10.1128/mmbr.63.1.54-105.1999

11 Das, M. *et al.* Oscillatory dynamics of Cdc42 GTPase in the control of polarized growth. *Science* **337**, 239-243 (2012). https://doi.org/10.1126/science.1218377

12 Butty, A. C. A positive feedback loop stabilizes the guanine-nucleotide exchange factor Cdc24 at sites of polarization. *The EMBO Journal* **21**, 1565-1576 (2002). https://doi.org/10.1093/emboj/21.7.1565

13 Das, M. & Verde, F. Role of Cdc42 dynamics in the control of fission yeast cell polarization. *Biochem Soc Trans* **41**, 1745-1749 (2013). https://doi.org/10.1042/BST20130241

14 Turing, A. M. The chemical basis of morphogenesis. 1953. *Bull Math Biol* **52**, 153-197; discussion 119-152 (1990). https://doi.org/10.1007/BF02459572

15 Wu, C. F. *et al.* Role of competition between polarity sites in establishing a unique front. *Elife* **4** (2015). https://doi.org/10.7554/eLife.11611

16 Chiou, J. G. *et al.* Principles that govern competition or co-existence in Rho-GTPase driven polarization. *PLoS Comput Biol* **14**, e1006095 (2018). https://doi.org/10.1371/journal.pcbi.1006095

17 Wu, C. F. & Lew, D. J. Beyond symmetry-breaking: competition and negative feedback in GTPase regulation. *Trends in cell biology* **23**, 476-483 (2013). https://doi.org/10.1016/j.tcb.2013.05.003

18 Lamas, I., Merlini, L., Vještica, A., Vincenzetti, V. & Martin, S. G. Optogenetics reveals Cdc42 local activation by scaffold-mediated positive feedback and Ras GTPase. *PLoS Biol* **18**, e3000600 (2020). https://doi.org/10.1371/journal.pbio.3000600

19 Hercyk, B. S., Rich-Robinson, J., Mitoubsi, A. S., Harrell, M. A. & Das, M. E. A novel interplay between GEFs orchestrates Cdc42 activity during cell polarity and cytokinesis. *Journal of Cell Science* **132**, jcs236018 (2019). https://doi.org/10.1242/jcs.236018

20 Chang, E. C. *et al.* Cooperative interaction of S. pombe proteins required for mating and morphogenesis. *Cell* **79**, 131-141 (1994). https://doi.org/0092-8674(94)90406-5 [pii]

21 Endo, M., Shirouzu, M. & Yokoyama, S. The Cdc42 binding and scaffolding activities of the fission yeast adaptor protein Scd2. *J Biol Chem* **278**, 843-852 (2003). https://doi.org/10.1074/jbc.M209714200

22 Revilla-Guarinos, M. T. *et al.* Rga6 is a Fission Yeast Rho GAP Involved in Cdc42 Regulation of Polarized Growth. *Mol Biol Cell* **27**, 1524-1535 (2016). https://doi.org/10.1091/mbc.E15-12-0818

23 Das, M. *et al.* Regulation of cell diameter, For3p localization, and cell symmetry by fission yeast Rho-GAP Rga4p. *Mol Biol Cell* **18**, 2090-2101 (2007). https://doi.org/10.1091/mbc.e06-09-0883

24 Gallo Castro, D. & Martin, S. G. Differential GAP requirement for Cdc42-GTP polarization during proliferation and sexual reproduction. *J Cell Biol* **217**, 4215-4229 (2018). https://doi.org/10.1083/jcb.201806016

25 Tatebe, H., Nakano, K., Maximo, R. & Shiozaki, K. Pom1 DYRK regulates localization of the Rga4 GAP to ensure bipolar activation of Cdc42 in fission yeast. *Curr Biol* **18**, 322-330 (2008). https://doi.org/10.1016/j.cub.2008.02.005

26 Howell, A. S. *et al.* Negative feedback enhances robustness in the yeast polarity establishment circuit. *Cell* **149**, 322-333 (2012). https://doi.org/10.1016/j.cell.2012.03.012

27 McCusker, D. & Kellogg, D. R. Plasma membrane growth during the cell cycle: unsolved mysteries and recent progress. *Current opinion in cell biology* **24**, 845-851 (2012). https://doi.org/10.1016/j.ceb.2012.10.008

28 Marcus, S. *et al.* Shk1, a homolog of the Saccharomyces cerevisiae Ste20 and mammalian p65PAK protein kinases, is a component of a Ras/Cdc42 signaling module in the fission yeast Schizosaccharomyces pombe. *Proceedings of the National Academy of Sciences* **92**, 6180-6184 (1995). https://doi.org/10.1073/pnas.92.13.6180

29 Tu, H. & Wigler, M. Genetic evidence for Pak1 autoinhibition and its release by Cdc42. *Mol Cell Biol* **19**, 602-611 (1999). https://doi.org/10.1128/mcb.19.1.602

30 Ottilie, S. *et al.* Fission yeast pak1+ encodes a protein kinase that interacts with Cdc42p and is involved in the control of cell polarity and mating. *The EMBO Journal* **14**, 5908-5919 (1995). https://doi.org/10.1002/j.1460-2075.1995.tb00278.x

31 Molli, P. R., Li, D. Q., Murray, B. W., Rayala, S. K. & Kumar, R. PAK signaling in oncogenesis. *Oncogene* **28**, 2545-2555 (2009). https://doi.org/10.1038/onc.2009.119

32 Onwubiko, U. N. *et al.* Cdc42 prevents precocious Rho1 activation during cytokinesis in a Pak1-dependent manner. *J Cell Sci* **136** (2023). https://doi.org/10.1242/jcs.261160

33 Magliozzi, J. O. *et al.* Fission yeast Pak1 phosphorylates anillin-like Mid1 for spatial control of cytokinesis. *J Cell Biol* **219** (2020). https://doi.org/10.1083/jcb.201908017

34 Magliozzi, J. O. & Moseley, J. B. Pak1 kinase controls cell shape through ribonucleoprotein granules. *Elife* **10** (2021). https://doi.org/10.7554/eLife.67648

35 Kuo, C. C. *et al.* Inhibitory GEF phosphorylation provides negative feedback in the yeast polarity circuit. *Current biology : CB* **24**, 753-759 (2014). https://doi.org/10.1016/j.cub.2014.02.024

36 Rapali, P. *et al.* Scaffold-mediated gating of Cdc42 signalling flux. *Elife* **6** (2017). https://doi.org/10.7554/eLife.25257

37 Das, M., Wiley, D. J., Chen, X., Shah, K. & Verde, F. The Conserved NDR Kinase Orb6 Controls Polarized Cell Growth by Spatial Regulation of the Small GTPase Cdc42. *Current Biology* **19**, 1314-1319 (2009). https://doi.org/10.1016/j.cub.2009.06.057

38 Kolluri, R., Tolias, K. F., Carpenter, C. L., Rosen, F. S. & Kirchhausen, T. Direct interaction of the Wiskott-Aldrich syndrome protein with the GTPase Cdc42. *Proc Natl Acad Sci U S A* **93**, 5615-5618 (1996). https://doi.org/10.1073/pnas.93.11.5615

39 Lechler, T., Shevchenko, A. & Li, R. Direct involvement of yeast type I myosins in Cdc42-dependent actin polymerization. *J Cell Biol* **148**, 363-373 (2000). https://doi.org/10.1083/jcb.148.2.363

40 Kovar, D. R., Sirotkin, V. & Lord, M. Three's company: the fission yeast actin cytoskeleton. *Trends Cell Biol* **21**, 177-187 (2011). https://doi.org/10.1016/j.tcb.2010.11.001

41 Onwubiko, U. N., Rich-Robinson, J., Mustaf, R. A. & Das, M. E. Cdc42 promotes Bgs1 recruitment for septum synthesis and glucanase localization for cell separation during cytokinesis in fission yeast. *Small GTPases* **12**, 257-264 (2021). https://doi.org/10.1080/21541248.2020.1743926

42 Onwubiko, U. N. *et al.* A Cdc42 GEF, Gef1, through endocytosis organizes F-BAR Cdc15 along the actomyosin ring and promotes concentric furrowing. *J Cell Sci* **132** (2019). https://doi.org/10.1242/jcs.223776

43 Thomas *et al.* Homeostatic Actin Cytoskeleton Networks Are Regulated by Assembly Factor Competition for Monomers. *Current Biology* **24**, 579-585 (2014). https://doi.org/10.1016/j.cub.2014.01.072

44 Bendezú, F. O. & Martin, S. G. Actin cables and the exocyst form two independent morphogenesis pathways in the fission yeast. *Molecular Biology of the Cell* **22**, 44-53 (2011). https://doi.org/10.1091/mbc.e10-08-0720

45 Martin, S. G., Rincon, S. A., Basu, R., Perez, P. & Chang, F. Regulation of the formin for3p by cdc42p and bud6p. *Molecular biology of the cell* **18**, 4155-4167 (2007).

46 Landino, J. *et al.* Rho and F-actin self-organize within an artificial cell cortex. *Curr Biol* **31**, 5613-5621 e5615 (2021). https://doi.org/10.1016/j.cub.2021.10.021

47 Lee, W.-L., Bezanilla, M. & Pollard, T. D. Fission Yeast Myosin-I, Myo1p, Stimulates Actin Assembly by Arp2/3 Complex and Shares Functions with Wasp. *Journal of Cell Biology* **151**, 789-800 (2000). https://doi.org/10.1083/jcb.151.4.789

48 Gachet, Y. & Hyams, J. S. Endocytosis in fission yeast is spatially associated with the actin cytoskeleton during polarised cell growth and cytokinesis. *J Cell Sci* **118**, 4231-4242 (2005). https://doi.org/10.1242/jcs.02530

49 Sirotkin, V., Beltzner, C. C., Marchand, J. B. & Pollard, T. D. Interactions of WASp, myosin-I, and verprolin with Arp2/3 complex during actin patch assembly in fission yeast. *J Cell Biol* **170**, 637-648 (2005). https://doi.org/10.1083/jcb.200502053

50 Campbell, B. F. *et al.* Cdc42 GTPase activating proteins Rga4 and Rga6 coordinate septum synthesis and membrane trafficking at the division plane during cytokinesis. *Traffic* **23**, 478-495 (2022). https://doi.org/10.1111/tra.12864

51 Hercyk, B. S. & Das, M. E. F-BAR Cdc15 Promotes Cdc42 Activation During Cytokinesis and Cell Polarization in Schizosaccharomyces pombe. *Genetics* **213**, 1341-1356 (2019). https://doi.org/10.1534/genetics.119.302649

52 Watson, L. J., Rossi, G. & Brennwald, P. Quantitative Analysis of Membrane Trafficking in Regulation of Cdc42 Polarity. *Traffic* **15**, 1330-1343 (2014). https://doi.org/10.1111/tra.12211

53 Pelham, R. J. & Chang, F. Role of actin polymerization and actin cables in actin-patch movement in Schizosaccharomyces pombe. *Nature Cell Biology* **3**, 235-244 (2001). https://doi.org/10.1038/35060020

54 Salat-Canela, C. *et al.* Stress-dependent inhibition of polarized cell growth through unbalancing the GEF/GAP regulation of Cdc42. *Cell Rep* **37**, 109951 (2021). https://doi.org/10.1016/j.celrep.2021.109951

55 Mutavchiev, D. R., Leda, M. & Sawin, K. E. Remodeling of the Fission Yeast Cdc42 Cell-Polarity Module via the Sty1 p38 Stress-Activated Protein Kinase Pathway. *Curr Biol* **26**, 2921-2928 (2016). https://doi.org/10.1016/j.cub.2016.08.048

56 Pelham, R. J. & Chang, F. Actin dynamics in the contractile ring during cytokinesis in fission yeast. *Nature* **419**, 82-86 (2002). https://doi.org/10.1038/nature00999

57 Feierbach, B. & Chang, F. Roles of the fission yeast formin for3p in cell polarity, actin cable formation and symmetric cell division. *Curr Biol* **11**, 1656-1665 (2001). https://doi.org/10.1016/s0960-9822(01)00525-5

58 Nolen, B. J. *et al.* Characterization of two classes of small molecule inhibitors of Arp2/3 complex. *Nature* **460**, 1031-1034 (2009). https://doi.org/10.1038/nature08231

59 Das, M. *et al.* Phosphorylation-dependent inhibition of Cdc42 GEF Gef1 by 14-3-3 protein Rad24 spatially regulates Cdc42 GTPase activity and oscillatory dynamics during cell morphogenesis. *Mol Biol Cell* **26**, 3520-3534 (2015). https://doi.org/10.1091/mbc.E15-02-0095

60 Stamnes, M. Regulating the actin cytoskeleton during vesicular transport. *Curr Opin Cell Biol* **14**, 428-433 (2002). https://doi.org/10.1016/s0955-0674(02)00349-6

61 Gundelfinger, E. D., Kessels, M. M. & Qualmann, B. Temporal and spatial coordination of exocytosis and endocytosis. *Nature reviews. Molecular cell biology* **4**, 127-139 (2003). https://doi.org/10.1038/nrm1016

62 Wu, L. G., Hamid, E., Shin, W. & Chiang, H. C. Exocytosis and endocytosis: modes, functions, and coupling mechanisms. *Annu Rev Physiol* **76**, 301-331 (2014). https://doi.org/10.1146/annurev-physiol-021113-170305

63 Novák, B. & Tyson, J. J. Design principles of biochemical oscillators. *Nature Reviews Molecular Cell Biology* **9**, 981-991 (2008). https://doi.org/10.1038/nrm2530

64 Xu, B. & Jilkine, A. Modeling the Dynamics of Cdc42 Oscillation in Fission Yeast. *Biophysical journal* **114**, 2025 (2018). https://doi.org/10.1016/j.bpj.2018.04.009

65 Goodwin, B. C. Oscillatory behavior in enzymatic control processes. *Adv Enzyme Regul* **3**, 425-438 (1965). https://doi.org/10.1016/0065-2571(65)90067-1

66 Cao, Y., Lopatkin, A. & You, L. Elements of biological oscillations in time and space. *Nat Struct Mol Biol* **23**, 1030-1034 (2016). https://doi.org/10.1038/nsmb.3320

67 Wheatley, E. & Rittinger, K. Interactions between Cdc42 and the scaffold protein Scd2: requirement of SH3 domains for GTPase binding. *The Biochemical journal* **388**, 177-184 (2005). https://doi.org/10.1042/BJ20041838

68 Lamas, I., Weber, N. & Martin, S. G. Activation of Cdc42 GTPase upon CRY2-Induced Cortical Recruitment Is Antagonized by GAPs in Fission Yeast. *Cells* **9** (2020). https://doi.org/ARTN 2089

10.3390/cells9092089

69 Sabherwal, N. *et al.* Differential phase register of Hes1 oscillations with mitoses underlies cell-cycle heterogeneity in ER(+) breast cancer cells. *Proc Natl Acad Sci U S A* **118** (2021). https://doi.org/10.1073/pnas.2113527118

70 Nakano, K., Satoh, K., Morimatsu, A., Ohnuma, M. & Mabuchi, I. Interactions among a fimbrin, a capping protein, and an actin-depolymerizing factor in organization of the fission yeast actin cytoskeleton. *Mol Biol Cell* **12**, 3515-3526 (2001). https://doi.org/10.1091/mbc.12.11.3515

71 Macquarrie, C. D. *et al.* Adaptor protein Bbc1 regulates localization of Wsp1 and Vrp1 during endocytic actin patch assembly. *Journal of Cell Science* **132**, jcs233502 (2019). https://doi.org/10.1242/jcs.233502

72 Arasada, R. & Pollard, Thomas D. Distinct Roles for F-BAR Proteins Cdc15p and Bzz1p in Actin Polymerization at Sites of Endocytosis in Fission Yeast. *Current Biology* **21**, 1450-1459 (2011). https://doi.org/https://doi.org/10.1016/j.cub.2011.07.046

73 Attanapola, S. L., Alexander, C. J. & Mulvihill, D. P. Ste20-kinase-dependent TEDS-site phosphorylation modulates the dynamic localisation and endocytic function of the fission

yeast class I myosin, Myo1. *Journal of Cell Science* **122**, 3856-3861 (2009). https://doi.org/10.1242/jcs.053959

74 Basu, R., Munteanu, E. L. & Chang, F. Role of turgor pressure in endocytosis in fission yeast. *Mol Biol Cell* **25**, 679-687 (2014). https://doi.org/10.1091/mbc.E13-10-0618

75 Bement, W. M. *et al.* Activator-inhibitor coupling between Rho signalling and actin assembly makes the cell cortex an excitable medium. *Nat Cell Biol* **17**, 1471-1483 (2015). https://doi.org/10.1038/ncb3251

76 Coll, P. M., Trillo, Y., Ametzazurra, A. & Perez, P. Gef1p, a new guanine nucleotide exchange factor for Cdc42p, regulates polarity in Schizosaccharomyces pombe. *Mol Biol Cell* **14**, 313-323 (2003). https://doi.org/10.1091/mbc.e02-07-0400

77 Tsai, T. Y.-C. *et al.* Robust, Tunable Biological Oscillations from Interlinked Positive and Negative Feedback Loops. *Science* **321**, 126-129 (2008). https://doi.org/10.1126/science.1156951

78 Hwang, J.-U., Gu, Y., Lee, Y.-J. & Yang, Z. Oscillatory ROP GTPase Activation Leads the Oscillatory Polarized Growth of Pollen Tubes. *Molecular Biology of the Cell* **16**, 5385-5399 (2005). https://doi.org/10.1091/mbc.e05-05-0409

79 Aghamohammadzadeh, S. & Ayscough, K. R. Differential requirements for actin during yeast and mammalian endocytosis. *Nat Cell Biol* **11**, 1039-1042 (2009). https://doi.org/10.1038/ncb1918

80 Epp, E. *et al.* Forward genetics in Candida albicans that reveals the Arp2/3 complex is required for hyphal formation, but not endocytosis. *Mol Microbiol* **75**, 1182-1198 (2010). https://doi.org/10.1111/j.1365-2958.2009.07038.x

81 Basu, R., Munteanu, E. L. & Chang, F. Role of turgor pressure in endocytosis in fission yeast. *Molecular Biology of the Cell* **25**, 679-687 (2014). https://doi.org/10.1091/mbc.e13-10-0618

82 Rich-Robinson, J., Russell, A., Mancini, E. & Das, M. Cdc42 reactivation at growth sites is regulated by local cell-cycle-dependent loss of its GTPase-activating protein Rga4 in fission yeast. *J Cell Sci* **134** (2021). https://doi.org/10.1242/jcs.259291

83 Ghose, D. & Lew, D. Mechanistic insights into actin-driven polarity site movement in yeast. *Mol Biol Cell* **31**, 1085-1102 (2020). https://doi.org/10.1091/mbc.E20-01-0040

84 Sawin, K. E., Hajibagheri, M. A. N. & Nurse, P. Mis-specification of cortical identity in a fission yeast PAK mutant. *Current Biology* **9**, 1335-1338 (1999). https://doi.org/10.1016/s0960-9822(00)80058-5

85 Messerli, M. & Robinson, K. R. Tip localized Ca2+ pulses are coincident with peak pulsatile growth rates in pollen tubes of Lilium longiflorum. *J Cell Sci* **110 (Pt 11)**, 1269-1278 (1997). https://doi.org/10.1242/jcs.110.11.1269

86 Messerli, M. A., Danuser, G. & Robinson, K. R. Pulsatile influxes of H+, K+ and Ca2+ lag growth pulses of Lilium longiflorum pollen tubes. *J Cell Sci* **112 (Pt 10)**, 1497-1509 (1999). https://doi.org/10.1242/jcs.112.10.1497

87 Karsenti, E. Self-organization in cell biology: a brief history. *Nature reviews. Molecular cell biology* **9**, 255-262 (2008). https://doi.org/nrm2357 [pii]

10.1038/nrm2357

88 Gerganova, V. *et al.* Cell patterning by secretion-induced plasma membrane flows. *Sci Adv* **7**, eabg6718 (2021). https://doi.org/10.1126/sciadv.abg6718

89 Rutkowski, D. M., Vincenzetti, V., Vavylonis, D. & Martin, S. G. Cdc42 mobility and membrane flows regulate fission yeast cell shape and survival. *bioRxiv* (2023). https://doi.org/10.1101/2023.07.21.550042

90 Glazenburg, M. M. & Laan, L. Complexity and self-organization in the evolution of cell polarization. *J Cell Sci* **136** (2023). https://doi.org/10.1242/jcs.259639

91 Guo, X. & Dong, J. Protein polarization: Spatiotemporal precisions in cell division and differentiation. *Curr Opin Plant Biol* **68**, 102257 (2022). https://doi.org/10.1016/j.pbi.2022.102257

92 Landge, A. N., Jordan, B. M., Diego, X. & Müller, P. Pattern formation mechanisms of self-organizing reaction-diffusion systems. *Dev Biol* **460**, 2-11 (2020). https://doi.org/10.1016/j.ydbio.2019.10.031

93 Stock, J. & Pauli, A. Self-organized cell migration across scales - from single cell movement to tissue formation. *Development* **148** (2021). https://doi.org/10.1242/dev.191767

94 Nobes, C. D. & Hall, A. Rho, rac, and cdc42 GTPases regulate the assembly of multimolecular focal complexes associated with actin stress fibers, lamellipodia, and filopodia. *Cell* **81**, 53-62 (1995). https://doi.org/10.1016/0092-8674(95)90370-4

95 Martin, K. *et al.* Spatio-temporal co-ordination of RhoA, Rac1 and Cdc42 activation during prototypical edge protrusion and retraction dynamics. *Sci Rep* **6**, 21901 (2016). https://doi.org/10.1038/srep21901

96 Fairn, G. D., Hermansson, M., Somerharju, P. & Grinstein, S. Phosphatidylserine is polarized and required for proper Cdc42 localization and for development of cell polarity. *Nat Cell Biol* **13**, 1424-1430 (2011). https://doi.org/10.1038/ncb2351

97 Hedrick, N. G. *et al.* Rho GTPase complementation underlies BDNF-dependent homo- and heterosynaptic plasticity. *Nature* **538**, 104-108 (2016). https://doi.org/10.1038/nature19784

98 Moreno, S., Klar, A. & Nurse, P. Molecular genetic analysis of fission yeast Schizosaccharomyces pombe. *Methods Enzymol* **194**, 795-823 (1991). https://doi.org/10.1016/0076-6879(91)94059-l

Appendix

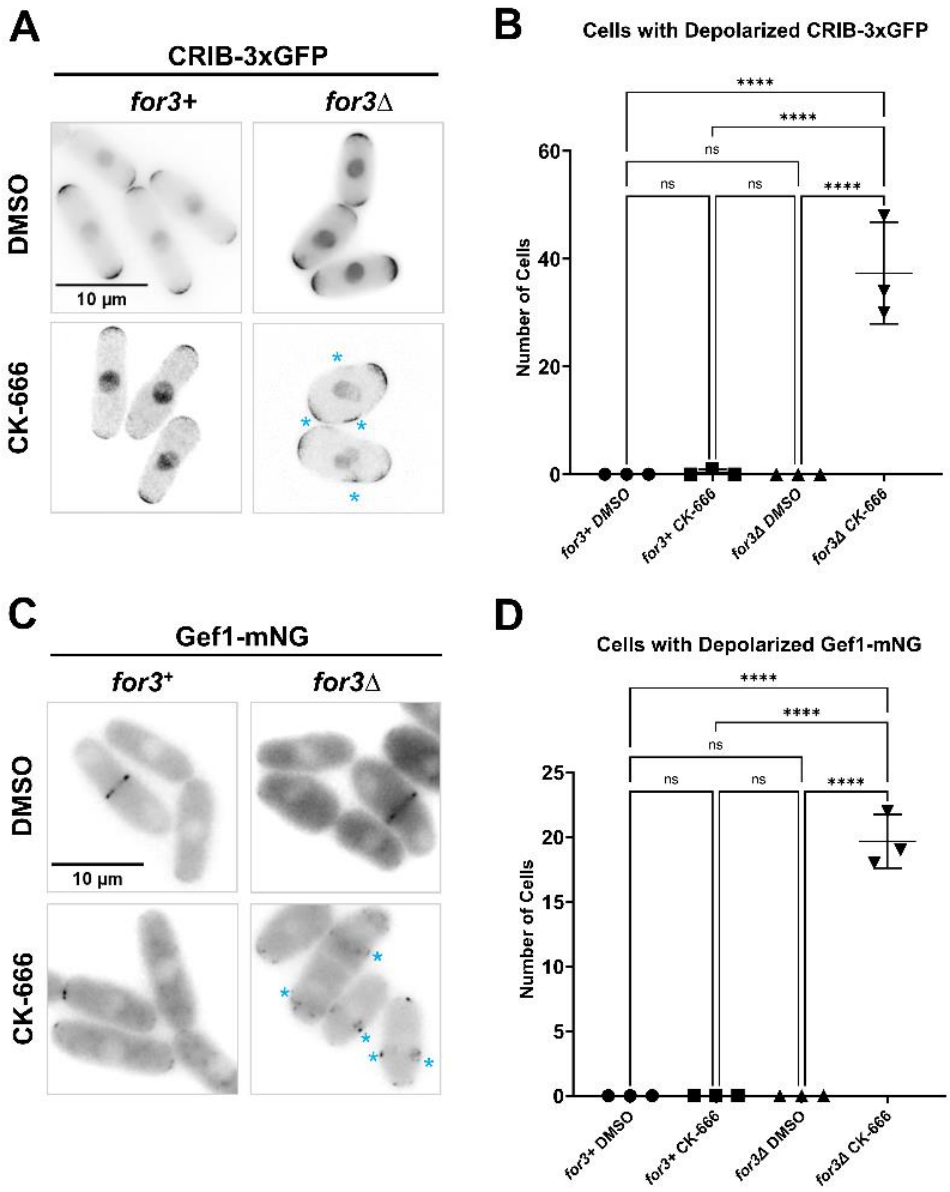

Figure S5. Loss of both F-actin structures causes a stress response but CK-666 treatment alone does not. A. CRIB-3xGFP localization in *for3+ and for3*Δ cells treated with DMSO and CK-666. **B.** Quantification of the number of cells with depolarized CRIB-3xGFP localization. **C.** Gef1-mNG localization in *for3+* and *for3*Δ cells treated with DMSO and CK-666. **D.** Quantification of the number of cells with depolarized Gef1-mNG localization. Scale bar, 10µm. n.s., not significant; p-value, ****<0.0001, One way ANOVA, followed by Tukey's multiple comparison test.

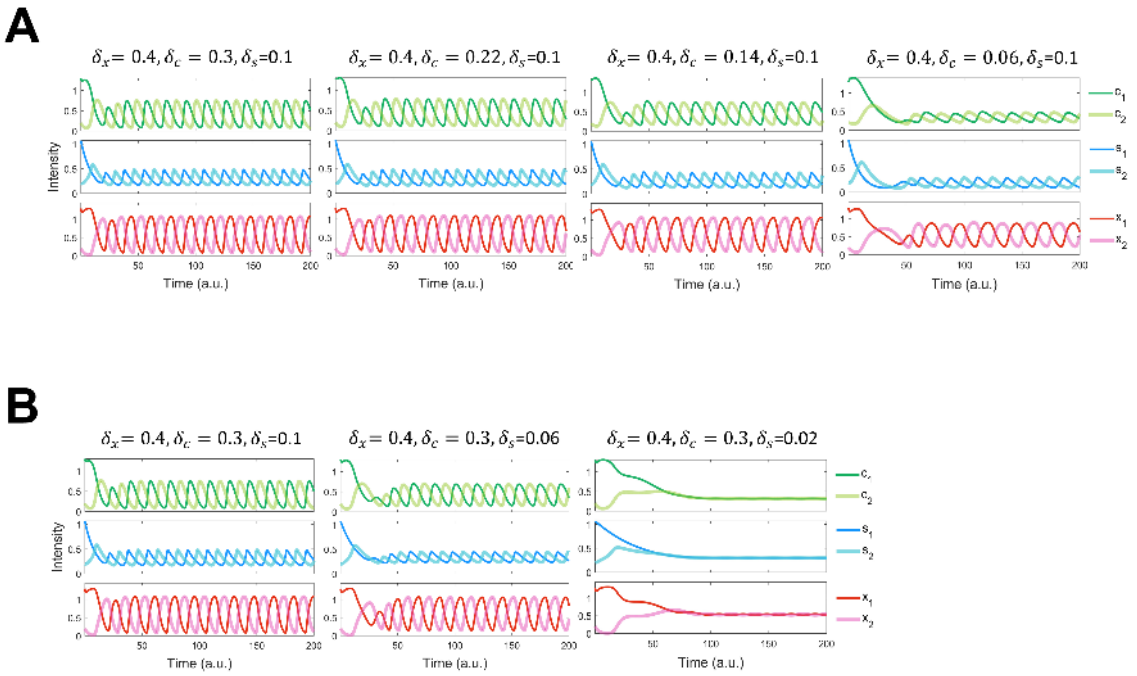

Figure S6. Bipolar dynamics preserved with varied detachment rates of active Cdc42 and Scd1. A. Bipolar dynamics after reducing the detachment rate of Cdc42 to 20% of the wild-type detachment rate. **B.** Protein dynamics upon reducing the detachment rate of Scd1 to 20% of the wild-type rate. The black dashed line is average concentration of Scd1 at the oscillatory dynamics tip**.**

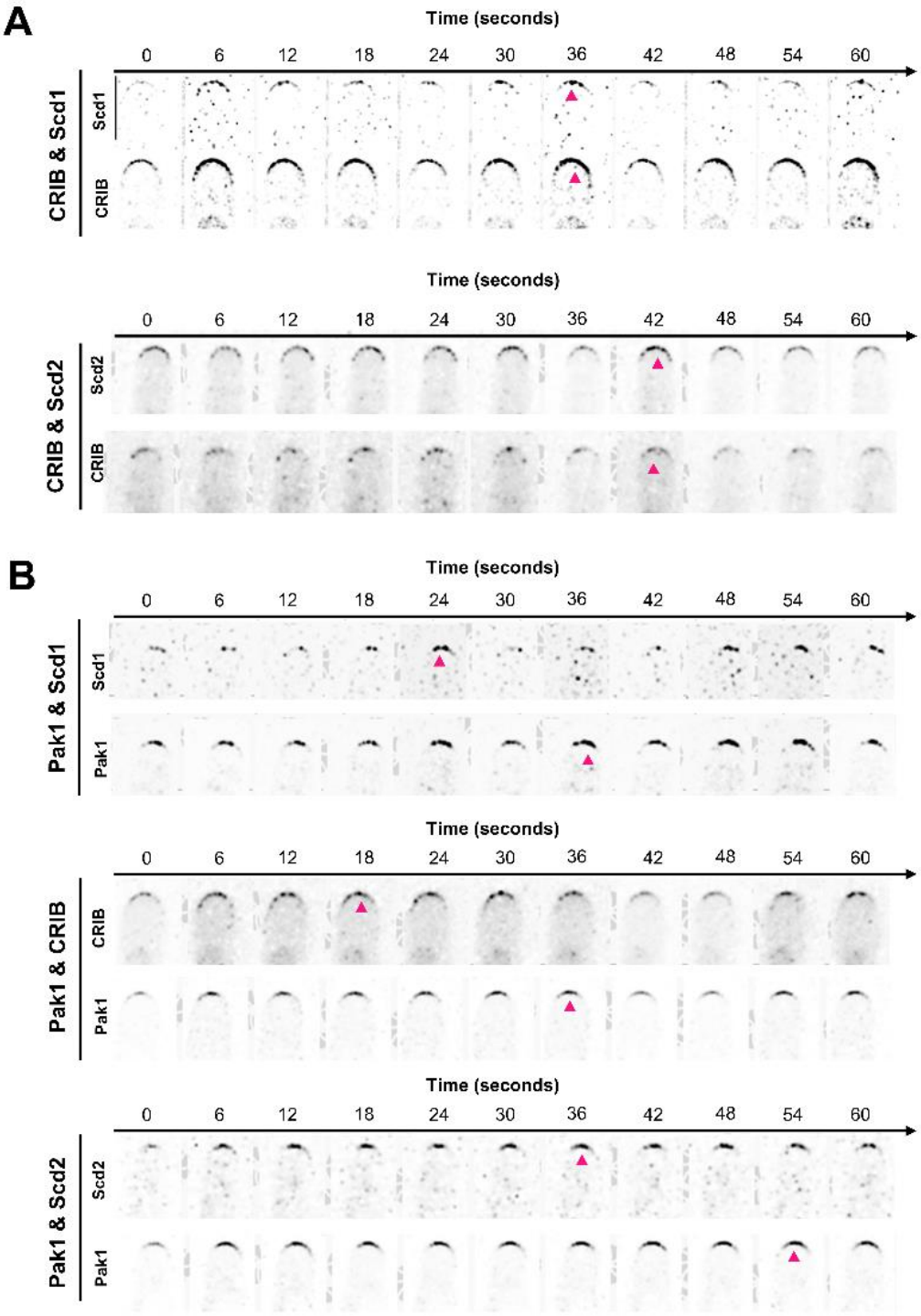

Figure S7. Montages of phase shift between pairs of polarity proteins. A. Montage of phase shift between Scd1-tdTomato and Cdc42 activity (CRIB-3xGFP) and between Scd2-mCherry and CRIB-3xGFP). Arrows denote peaks in intensity. **B.** Montage of phase shift between Pak1-mEGFP and the positive feedback proteins: Scd1-tdTomato, active Cdc42 (CRIB-mCherry), and Scd2-mCherry. Arrows indicate peaks in intensity. Montages clarified and denoised, made in NIS elements. Scale bar 5 μm.

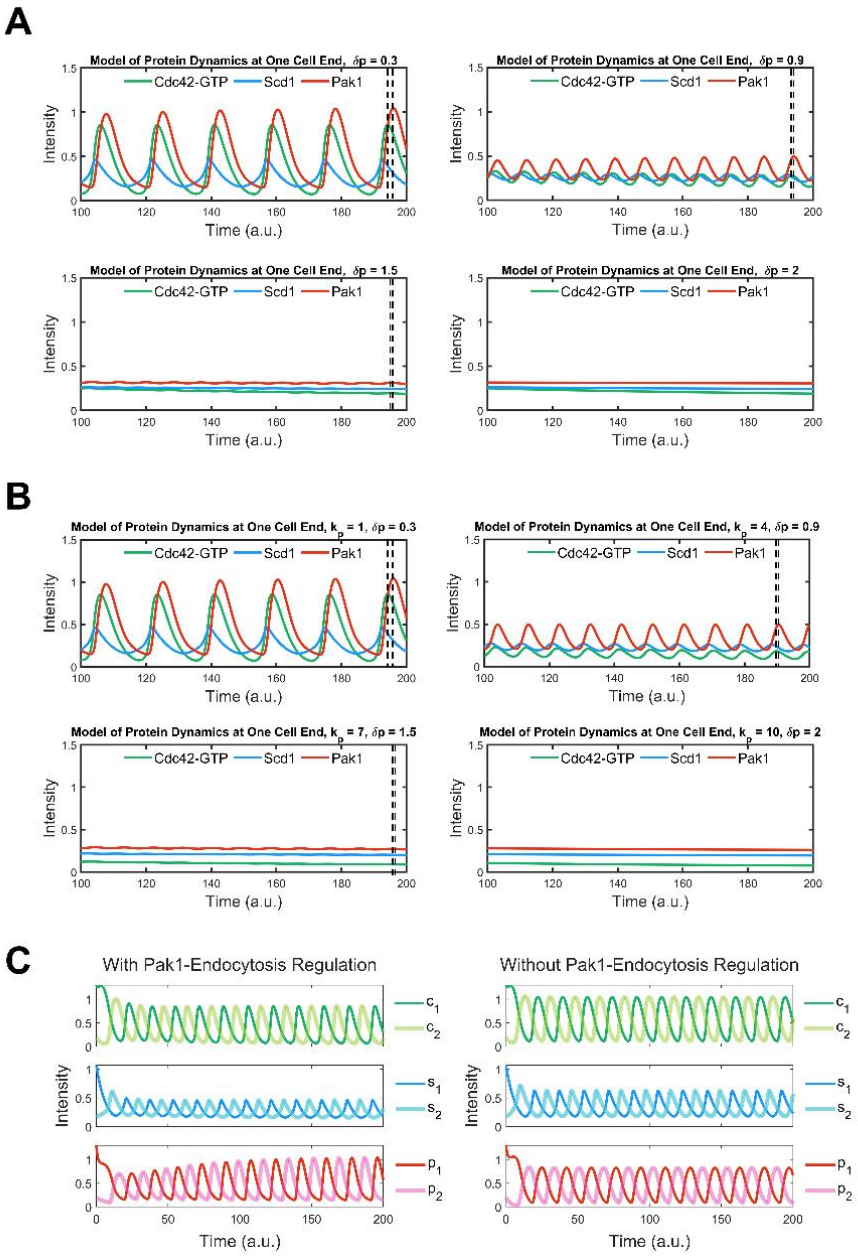

Figure S8. Reduction and elimination of phase shift between Cdc42-GTP and Pak1 with increased Pak1 attachment/ detachment rate constants in the model. A. Incrementally increasing the detachment rate constant of Pak1 (δ_p) from 0.3 to 2 leads to a gradual reduction in the phase shift between Cdc42-GTP and Pak1. As δ_p nears 2, this shift becomes less pronounced, culminating in a dampened oscillation that eventually subsides. **B.** A simultaneous elevation of both the attachment rate constant (k_p) from 1 to 10 and δ_p from 0.3 to 2 induces a progressive decrease in the phase shift between Cdc42-GTP and Pak1. This shift declines as the pair (k_p, δ_p) reaches (10, 2), whereupon the oscillation is increasingly attenuated and ultimately extinguished. The separation between the dashed black lines illustrates the phase discrepancy between Cdc42-GTP and Pak1. First figure is Wild type. **C.** A comparison between model results with and without Pak1-endocytosis regulation.

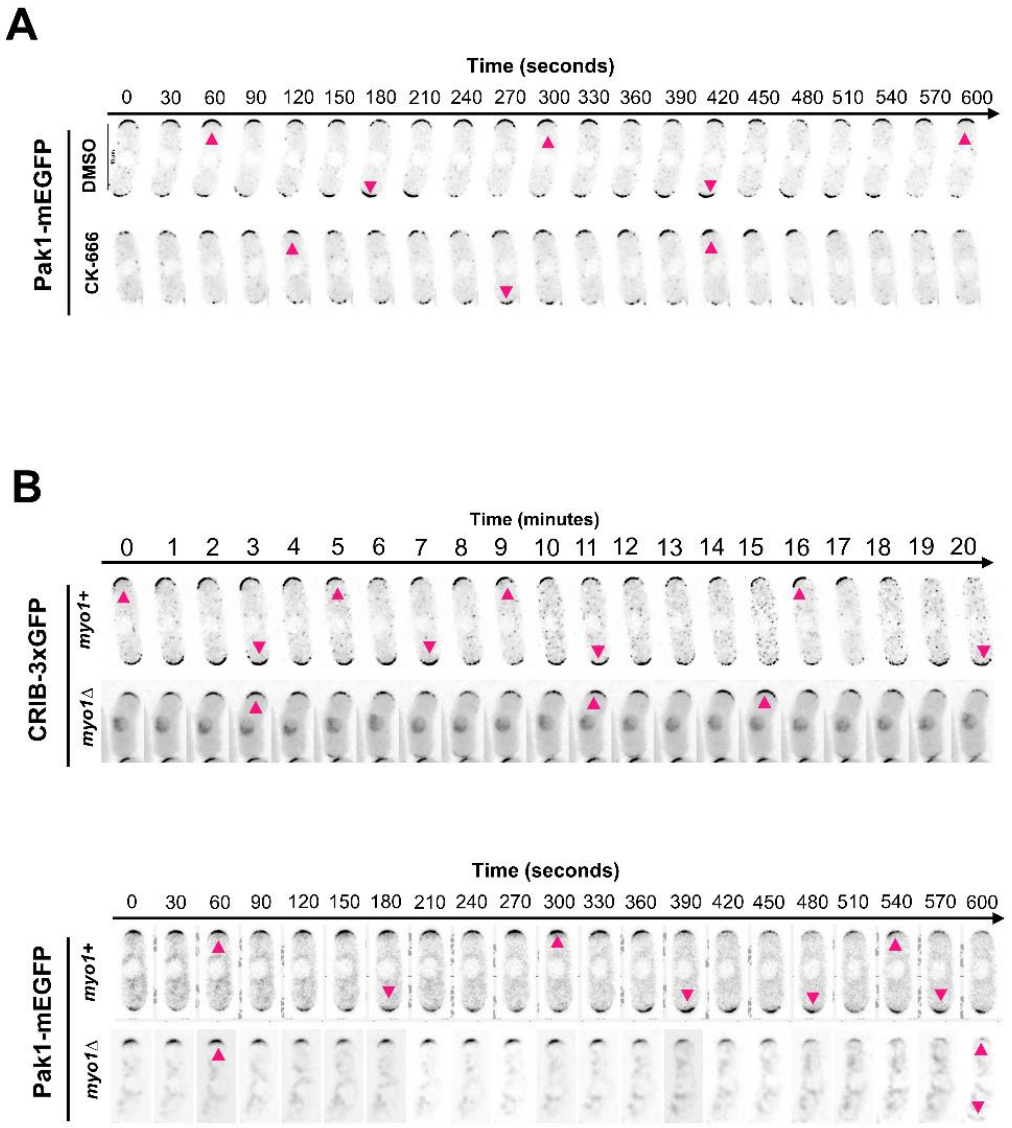

Figure S9. Pak1-mEGFP and CRIB-GFP dynamics under different conditions. A. Pak1-mEGFP dynamics in DMSO and CK-666 treated cells. Red arrows indicate peaks of fluorescence intensity at that cell end. **B.** Dynamics of CRIB-GFP and Pak1-mEGFP were observed in *myo1*+ and *myo1*Δ cells. Red arrows indicate peaks of fluorescent intensity at that cell end. Montages clarified and denoised, made in NIS elements. Scale bar 10µm.

Mathematical Modeling

Model 1: Based on the Xu-Jilkine model [63,64], this model employs reaction-diffusion equations to delineate the regulatory network, yet it is founded on networks that are distinct from those of the original. The network in the present model encompasses active molecules such as Cdc42-GTP and Scd1 at the cell tips, in addition to the diffusion of their inactive counterparts, Cdc42-GDP and Scd1, throughout the cytoplasm.

In the model, the total amounts of Cdc42(C_{total}) and Scd1(S_{total}) are conserved (constant), encompassing both cytoplasmic and tip-localized Cdc42 and Scd1. The two cell tips engage in competition for the acquisition of Cdc42 and Scd1. Here, $C(x,t)$ represents the inactive Cdc42 in the cytoplasm, and $S(x,t)$ denotes the cytoplasmic Scd1. The terms $c_i(t)$ and $s_i(t)$, where $i = 1, 2$, correspond to the active Cdc42 and the accumulated Scd1 at the tips, respectively. L is the length of cell cytoplasm. The volume of each tip, V_i (with $i = 1, 2$), is assumed to be one unit:

$$\sum_{i=1}^{2} c_i V_i + \int_0^L C(x,t)\,dx = C_{total} \qquad (1)$$

$$\sum_{i=1}^{2} s_i V_i + \int_0^L S(x,t)\,dx = S_{total} \qquad (2)$$

The diffusion part in the cytoplasm derived from (1) and (2) is:

$$\frac{\partial C}{\partial t}(x,t) = D_C \frac{\partial^2 C}{\partial x^2}(x,t) \qquad (3)$$

$$\frac{\partial S}{\partial t}(x,t) = D_S \frac{\partial^2 S}{\partial x^2}(x,t). \qquad (4)$$

D_C and D_S are diffusion coefficients of Cdc42-GDP and Scd1, respectively.

The reaction part at tips is

$$\frac{dc_i}{dt}(t) = k^c(s_i(t))C(L_i,t) - \delta_c c_i(t), \quad i = 1,2 \qquad (5)$$

$$\frac{ds_i}{dt}(t) = k^s(c_i(t))S(L_i,t) - \delta_s s_i(t), \quad i = 1,2 \qquad (6)$$

$$k^c(s_i(t)) = \frac{k_c s_i(t)^{n_{sc}}}{s_i(t)^{n_{sc}} + {K_{sc}}^{n_{sc}}} \quad (7)$$

$$k^s\big(c_i(t)\big) = \frac{k_s c_i(t)^{n_{cs}}}{(c_i(t)^{n_{cs}} + {K_{cs}}^{n_{cs}})\left(1+\left(\frac{c_i(t)}{K_{as}}\right)^{n_{as}}\right)}. \quad (8)$$

c_i, g_i and p_i are active Cdc42, Scd1, and Pak1 at two tips. δ_C is the detachment rate constant for molecule Cdc42-GTP. δ_S is the detachment rate constant for molecule Scd1. One time unit is one minute.

Model 2: The structural design of Model 2 closely resembles that of Model 1. The network includes Cdc42-GTP, protein X (Pak1), and Scd1 at the tips, as well as the diffusion of inactive molecules like Cdc42-GDP, protein X (Pak1), and Scd1 within the cytoplasm. Pak1 is described as protein X at first. In model 2, the detachment term for Pak1, denoted as X, is given by $\delta_x x_i(t)$. Following identification of X as Pak1, which can promote the endocytosis, the detachment term is updated to $\delta_p(k_o + f\big(p_i(t)\big))p_i(t)$. k_o represents other elements in the cell which can also promote endocytosis.

The diffusion part:

$$\frac{\partial C}{\partial t}(x,t) = D_C \frac{\partial^2 C}{\partial x^2}(x,t) \quad (9)$$

$$\frac{\partial S}{\partial t}(x,t) = D_S \frac{\partial^2 S}{\partial x^2}(x,t) \quad (10)$$

$$\frac{\partial P}{\partial t}(x,t) = D_P \frac{\partial^2 P}{\partial x^2}(x,t) \quad (11)$$

D_C, D_S and D_P are diffusion coefficients of Cdc42-GDP, Scd1, and Pak1, respectively.

The equations at tips for the second model are:

$$\frac{dc_i}{dt}(t) = k^c(s_i(t))C(L_i,t) - \delta_c c_i(t), \quad i = 1,2 \quad (12)$$

$$\frac{ds_i}{dt}(t) = k^s(c_i(t), p_i(t))S(L_i,t) - \delta_s s_i(t), \quad i = 1,2 \quad (13)$$

$$\frac{dp_i}{dt}(t) = k^p\big(c_i(t)\big)P(L_i,t) - \delta_p(k_o + f\big(p_i(t)\big))p_i(t), \quad i = 1,2 \quad (14)$$

$$k^c(s_i(t)) = \frac{k_c s_i(t)^{n_{sc}}}{s_i(t)^{n_{sc}} + K_{sc}{}^{n_{sc}}} \quad (15)$$

$$k^s(c_i(t), p_i(t)) = \frac{k_s c_i(t)^{n_{cs}}}{(c_i(t)^{n_{cs}} + K_{cs}{}^{n_{cs}})(1 + (\frac{p_i(t)}{K_{ps}})^{n_{ps}})} \quad (16)$$

$$k^p(c_i(t)) = \frac{k_p c_i(t)^{n_{cp}}}{c_i(t)^{n_{cp}} + K_{cp}{}^{n_{cp}}} \quad (17)$$

$$f(p_i(t)) = \frac{p_i(t)^{n_{pe}}}{p_i(t)^{n_{pe}} + K_{pe}{}^{n_{pe}}} \quad (18)$$

c_i, g_i and p_i are active Cdc42, Scd1, and Pak1 at two tips. δ_C and δ_S are the same in Model1, δ_p is the detachment rate constant for molecule Pak1. f(p) describes that Pak1 promotes endocytosis.

The inclusion of activation of endocytosis by Pak1 locally (Eq 18) does not change the general behaviors of the model significantly, e.g. the bipolarity and anti-correlated oscillation. Nonetheless, comparing two versions of Model 2 (without Pak1-dependent endocytosis regulation: $f(p_i(t)) \equiv 1$, and with Pak1-dependent endocytosis regulation: Eq 18), we observed some minor differences, including larger amplitude of Pak1 oscillation, and smaller amplitudes of Cdc42-GTP and Scd1 oscillations with the inclusion of Pak1-dependent endocytosis regulation (**Fig.S4C**).

Model 3: Incorporating another negative feedback loop into the Cdc42-GTP regulatory network, we seek to provide an explanation for bipolarity in the absence of Pak1. However, the specific details of this second feedback loop are unknown. As a result, we made the assumption that active Cdc42 can inhibit itself, either directly or indirectly. Eq 12 is changed to:

$$\frac{dc_i}{dt}(t) = k^c(s_i(t), c_i(t))C(L_i, t) - \delta_c c_i(t), \quad i = 1,2 \quad (12a)$$

and Eq 15 is changed to:

$$k^c(s_i(t), c_i(t)) = \frac{k_c s_i(t)^{n_{sc}}}{s_i(t)^{n_{sc}} + K_{sc}{}^{n_{sc}}} \, e^{\frac{-c_i(t)}{a1}} \quad . \quad (15a)$$

Here $a1$ is a constant describing the strength of the second negative feedback loop.

Comparison of oscillatory dynamics between Model 1 and Model 2: In MATLAB, Sobol parameter spaces are defined for each model, with each model having 100,000 sample points in its parameter space. The objective is to detect oscillatory dynamics by counting peaks and measuring the differences in amplitude between neighboring peaks. The parameter sets that lead to oscillatory dynamics are counted and used to calculate the percentage of occurrences of oscillatory dynamics. (Range of parameters are in **table S1**)

Table S2. Parameter values of the wild-type model2, including parameters in model2-1.

Parameter	Description	Value (Model-X)	Value (Model-Pak1)	Unit	Range for oscillation search
D_C	Diffusion of Cdc42-GDP in cytoplasm	5	5	a.u. length/s	(0,10)
D_S	Diffusion of Scd1 in cytoplasm	5	5	a.u. length/s	(0,10)
D_P	Diffusion of Pak1 in cytoplasm	5	5	a.u. length/s	(0,10)
k_c	Activation rate constant of Cdc42 at tips	1.5	1.7		(0,2)
n_{sc}	Cooperativity of active Cdc42 self-regulation	4.5	5		(0,6)
K_{sc}	Threshold of Cdc42 activation by Scd1	0.545	0.5	a.u	(0,1)
δ_c	Detachment rate constant of active Cdc42	0.3	0.3	/min	(0,1)
k_s	Accumulation rate constant of Scd1 at tips	1.5	1.5		(0,2)
n_{cs}	Cooperativity of Scd1 by active Cdc42	1	1		(0,4)
K_{cs}	Threshold of Scd1 accumulation by active Cdc42	1	1	a.u.	(0,2)
K_{ps}	Threshold of Scd1 inhibition by Pak1	0.085	0.1	a.u.	(0,1)
n_{ps}	Cooperativity of Scd1 by Pak1	3	3		(0,6)
δ_s	Detachment rate constant of Scd1	0.1	0.1	/min	(0,1)
k_p	Attachment rate constant of Pak1 at tips	2	1		(0,2)
n_{cp}	Cooperativity of Pak1 by active Cdc42	3	3		(0,6)
K_{cp}	Threshold of Pak1 attachment by active Cdc42	0.5	1	a.u.	(0,2)
δ_p	Detachment rate constant of Pak1	0.4	0.3	/min	(0,2)
a1	Strength constant of second negative signaling pathway		0.5		
n_{pe}	Cooperativity of endocytosis/patches by Pak1		3		
K_{pe}	Threshold of endocytosis by Pak1		0.3	a.u.	
k_o	Cooperativity of endocytosis/patches by other elements		0.2		

* a.u. is an arbitrary unit of concentration.
** a.u. length is an arbitrary unit of length.

Modified parameters for mutants and Model3 were labeled above their corresponding figures.

MATLAB CODE

```
%Below is code for WT, CK666 is decreasing detachment of Pak1

time=1000;
tspan = [0:0.1:time];
tsteps=time/0.01;
hx = 0.1;
L = 1;
xspan = 0:hx:L;
n = numel(xspan);

%initial condition
C0 = 0.15*ones(n,1);
G0 = 0.1*ones(n,1);
P0= 0.1*ones(n,1);
cgp = [1.3;0.2;1.07;0.2;1.3;0.2];

u0 = [C0;G0;P0;cgp];

% parameters
Dc=3;
Dg=3;
Dp=3;

k0=1.7;
nsc=5;
ksc=0.5;
deltac=0.3;

k_on=1.5;
ncs=1;
kcs=1;
kps=0.1;
nps=3;
deltas=0.15;

kpa=1;
ncp=3;
kcp=1;
deltap=0.3;
npe=3;
kpe=0.3;

p = [Dc;Dg;k0;nsc;ksc;deltac; k_on;ncs;kcs;kps;nps;deltas;kpa;ncp;kcp;deltap;Dp;as;npe;kpe];
% solve
[T ,Y] = ode15s(@(t,u) ode_solve(t,u,p,n,hx),tspan,u0);

y1=real(round(Y(:,end-5),4));% round a decimal to 4 digits
y11=real(round(Y(:,end-4),4));
y2=real(round(Y(:,end-3),4));
```

```
y22=real(round(Y(:,end-2),4));
y3=real(round(Y(:,end-1),4));
y33=real(round(Y(:,end),4));
y_cyto1=real(round(Y(:,n+1),4));
y_cyto2=real(round(Y(:,2*n),4));
figure;
set(gcf, 'Position', [100, 100, 600, 270]);
% Plot only the first graph
ax1 = axes; % Use axes for a single plot
plot(ax1,T,y1,'color',[0.1 0.7 0.4],'linewidth',2.5);
hold on;
plot(ax1,T,y2,'color',[0.1010 0.6 1],'linewidth',2.5);
hold on;
%}
plot(ax1,T,y3,'color',[0.9 0.2 0.1],'linewidth',2.5);

% Set the thickness of the plot boundary
set(ax1, 'LineWidth', 2); % Increase this value for a thicker boundary

% Add title
title(['Model of Protein Dynamics at One Cell End, k_79 = ' num2str(kpa) ', \deltap = '
num2str(deltap)],'FontSize',18);
% Adjust legend
h = legend('Cdc42-GTP', 'Scd1', 'Pak1', 'Location', 'Best', 'Orientation', 'horizontal', 'Box', 'off');
set(h, 'FontSize', 15);
set(gca, 'FontSize', 12);

% Adjust title and labels
xlabel('Time (a.u.)', 'FontSize', 17);
ylabel('Intensity', 'FontSize', 17);
xlim([100 200]);
ylim([0 1.5])
% Save the figure as SVG
print(gcf,'myPlot.jpg','-djpeg','-r600');

function F = ode_solve(t,u,p,n,hx)
c1 = u(3*n+1);
c2 = u(3*n+2);
g1 = u(3*n+3);
g2 = u(3*n+4);
pa1= u(3*n+5);
pa2=u(3*n+6);

Dc = p(1);
Dg = p(2);
k0 = p(3);
nsc=p(4);
ksc=p(5);
deltac=p(6);
k_on = p(7);
ncs=p(8);
```

```
kcs=p(9);
kps=p(10);
nps=p(11);
deltas=p(12);
kpa=p(13);
ncp=p(14);
kcp=p(15);
deltap=p(16);
Dp=p(17);
as=p(18);
npe=p(19);
kpe=p(20);

kplus = @(x) k0*x^nsc/(x^nsc+ksc^nsc);
kon = @(y,z) k_on*(y^ncs+0)/(kcs^ncs+y^ncs).*1/(1+as*(z/kps)^nps);
kp = @(y) kpa*y^ncp/(kcp^ncp+y^ncp);
ep = @(z) (0.2+(z^npe)/(z^npe+kpe^npe));

rc = Dc/(hx^2);
rg = Dg/(hx^2);
rp=Dp/(hx^2);

F(1) = rc*(-(2+2*hx*kplus(g1)/Dc).*u(1) + 2*u(2) + 2*hx*deltac*c1/Dc);   %DCDt(1)
F(2:n-1) = rc*(u(1:n-2) - 2*u(2:n-1) + u(3:n));% DCDt(2:n-1)
F(n) = rc*(2*u(n-1) - (2+2*hx*kplus(g2)/Dc).*u(n) + 2*hx*deltac*c2/Dc);

F(n+1) = rg*(-(2+2*hx*kon(c1,pa1)/Dg).*u(n+1) + 2*u(n+2) + 2*hx*deltas*g1/Dg);   %DGDt
F(n+2:2*n-1) = rg*(u(n+1:2*n-2) - 2*u(n+2:2*n-1) + u(n+3:2*n));
F(2*n) = rg*(2*u(2*n-1) - (2+2*hx*kon(c2,pa2)/Dg).*u(2*n) + 2*hx*deltas*g2/Dg);

F(2*n+1) = rp*(-(2+2*hx*kp(c1)/Dp).*u(2*n+1) + 2*u(2*n+2) + 2*hx*deltap*pa1/Dp);   %DGDt
F(2*n+2:3*n-1) = rp*(u(2*n+1:3*n-2) - 2*u(2*n+2:3*n-1) + u(2*n+3:3*n));
F(3*n) = rp*(2*u(3*n-1) - (2+2*hx*kp(c2)/Dp).*u(3*n) + 2*hx*deltap*pa2/Dp);

F(3*n+1) = kplus(g1).*u(1) - deltac*c1;
F(3*n+2) = kplus(g2).*u(n) - deltac*c2;
F(3*n+3) = kon(c1,pa1).*u(n+1) - deltas*g1;
F(3*n+4) = kon(c2,pa2).*u(2*n) - deltas*g2;
F(3*n+5) = kp(c1).*u(2*n+1)-deltap*ep(pa1)*pa1;
F(3*n+6) = kp(c2).*u(3*n)-deltap*ep(pa2)*pa2;
F = F(:);
end
```

CHAPTER IV

MODEING SUBTYPE DYNAMICS AND HETEROGENEITY IN SMALL CELL LUNG CANCER USING ORDINARY DIFFERENTIAL EQUATIONS

This chapter is still on progress:

Author: Ziyi Liu, Darren R. Tyson, Tian Hong

I was responsible for the conceptualization, validation, formal analysis, investigation, visualization, methodology, software development, and draft of the manuscript.

Abstract

Small Cell Lung Cancer (SCLC) is characterized by rapid progression and notable heterogeneity, presenting significant challenges for effective treatment. There are at least four subtypes (ASCL1, NEUROD1, POU2F3, YAP1) of SCLC with different expression patterns and cellular phenotypes. The diversity of the subtypes and the transitions among them contribute to SCLC progression, but the underlying mechanisms are not well understood. In this study, we developed a framework based on ordinary differential equations (ODEs) to model the formation of SCLC subtypes, centering at a few key transcription factors of SCLC subtypes. We developed an automated parameter space analysis of ODEs, which enables the identification of different states based on the levels of selected genes. We fitted the model to the data, and our model successfully captured the main SCLC subtypes, the stepwise dynamics of SCLC progression, and the coexistence of subtypes under the same conditions. Additionally, the model predicted stable intermediate expression of ASCL1, which is consistent with single-cell transcriptome data. This approach allows us to map out a detailed landscape of SCLC subtype dynamics, providing a deeper understanding of the mechanisms driving tumor heterogeneity and progression.

Introduction

Small cell lung cancer (SCLC) is a highly aggressive form of lung cancer, make up about 15% of lung cancer cases[1], it characterized by significant heterogeneity marked by ASCL1, NEUROD1, POU2F3, and YAP1[2-4], rapid invasion, a high rate of recurrence following treatment, and a tendency for early metastasis[5,6]. SCLC often presents with paraneoplastic syndromes[7] and is associated with a poor prognosis due to its rapid progression and limited treatment options[8], and the 5-year relative survival rate for SCLC is approximately 3.5%[9]. Despite its clinical relevance, the mechanisms underlying these novel characteristics of SCLC remain poorly understood. It is believed that SCLC originates from neuroendocrine cells in the bronchus[10], with known contributing factors including RB1 and TP53 mutations[5,11-13]. c-MYC (MYC) is an oncogene overexpressed in many cancers[14,15]. In SCLC, approximately 30% of tumors overexpress MYC[3,16], and it's expression varies across different subtypes[4,17], leading to increased cancer cell proliferation, enhanced metastasis and aggressiveness, reprogramming of neuroendocrine fate, and resistance to therapy[13,16,18].

While factors such as epigenetic regulation[19], immune system interactions[20,21], and epithelial-mesenchymal transition (EMT)[22] are also implicated in SCLC, our focus is not on these mechanisms. Instead, we concentrate on biomarkers derived from various datasets that can identify different SCLC subtypes, which represents the first step in our workflow (**Fig. 17**), we focused on 4 subtypes including A2, A, N, Y[3,4,20,21]. The second part of our workflow involves using SCLC and EMT transcription factors (TFs) to derive a large regulatory network based on the TRRUST database[23]. One key question: Are there existing core nodes and feedback loops among them that underlie the heterogeneity and plasticity of SCLC? Boolean and ordinary differential equation (ODE) models built to explain heterogeneity often use highly complex

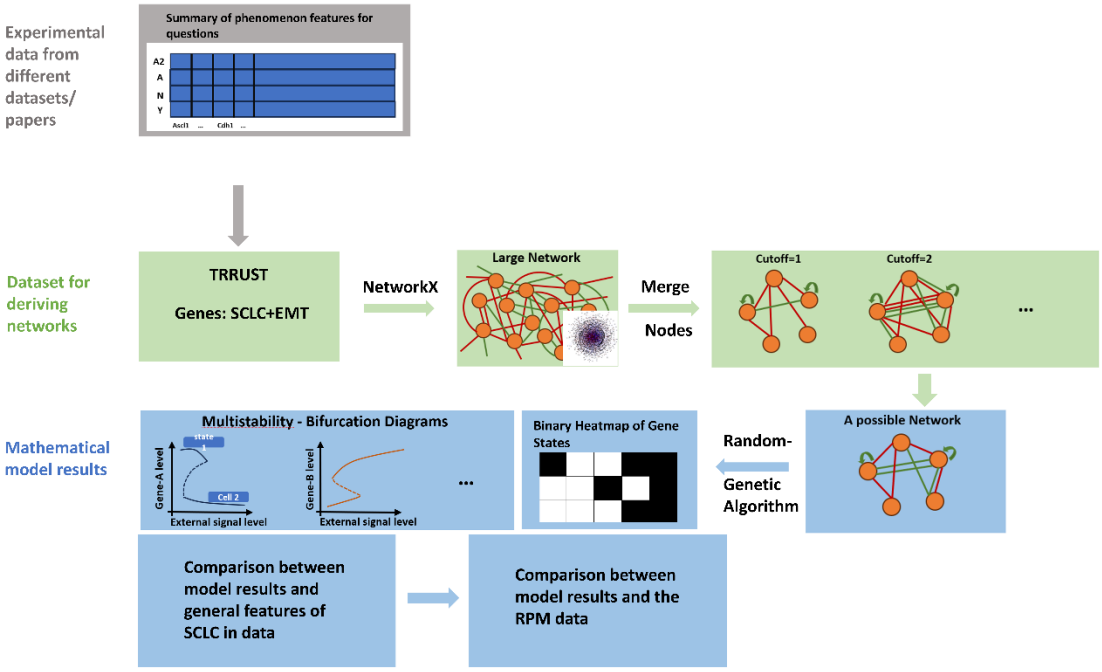

Figure 17. Workflow

identification of critical regulatory mechanisms. To address this, we select several key TFs of SCLC—specifically ASCL1, NEUROD1, YAP1, and MYC—as core nodes to construct a simplified network. Other nodes will be merged into promotion and repression effects. The third part of our workflow involves choosing one of the sub-networks from the simplified network, constructing ordinary differential equations (ODEs), and conducting a parameter space search and analysis to identify different states based on the TF levels. We will then compare the model results with general subtypes from various datasets and specific single-cell transcriptome data[18].

Results

To illustrate the complexity of progression of SCLC, a figure is created for categorizing factors involved into two networks **(Fig.18A**). The internal network consists of factors with differential expression among SCLC subtypes, which are unique to SCLC (not generally exists in other cancers) and likely contribute to its specific characteristics[4]. The second network is the external network which includes the mutants, epigenetic changes, EMT, microenvironment and other factors. While the interactions between these two networks and their effects on signaling pathways and heterogeneity of SCLC are largely unknown, this study primarily focuses on the internal network induced using NetworkX[24] (**Fig.18B (i)**) (materials and methods).

ASCL1, NEUROD1, and YAP1 were selected as core nodes, while MYC acts as a dysregulated signal. HES1 and ZEB1 were included in constructing the simplified network by merging other nodes into the signaling pathways as promoters or repressors. The simplified networks are categorized based on the largest number of merged nodes in a single signaling pathway: a cutoff of 0 indicates direct interactions between nodes (**Fig. 18B(ii)**), a cutoff of 1 allows for one merged node (**Fig. 18B(iii)**), and a cutoff of 2 allows for two merged nodes (**Fig. 18B(iv)**). To identify the simplest networks with multi-steady states, we focused on the cutoff=2 network due

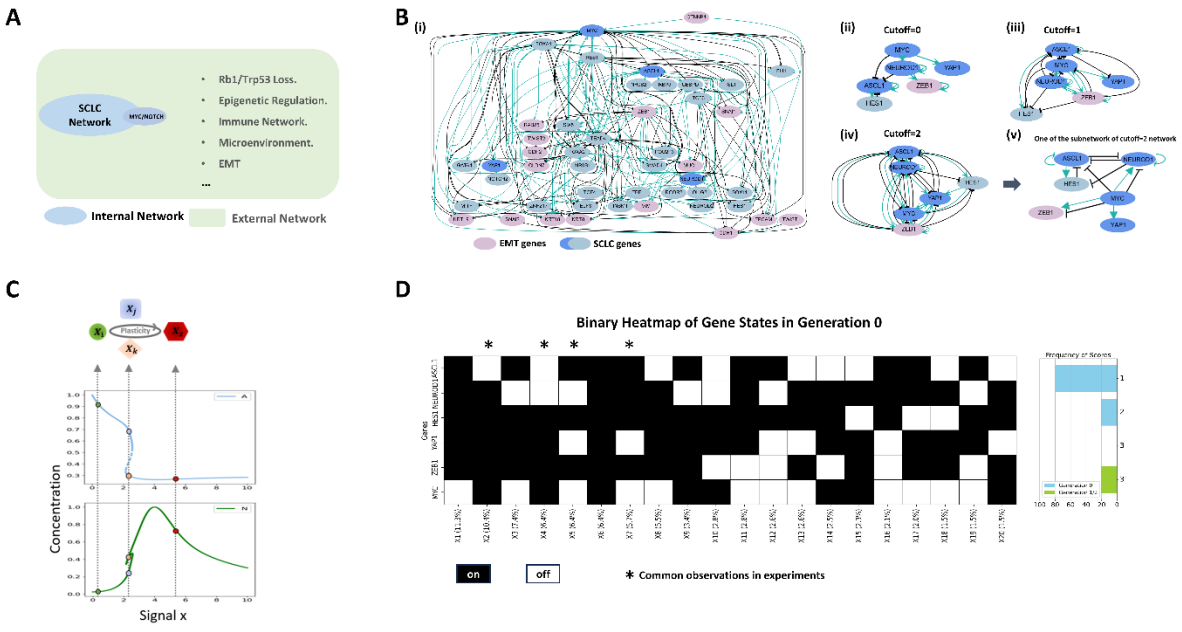

Figure 18. The simplified network based on ASCL1-NEUROD1 feedback captures the main SCLC states with coexistence. A. The assumption is that internal and external networks define the features of SCLC, encompassing both the general features common to many cancers and the unique features specific to SCLC. The external network interact and disrupts the internal network, transforming it into a cancerous network and revealing novel features of SCLC. **B. (i)** The large direct network for SCLC nodes combined with EMT nodes. Green arrow is promotion, black arrow is repression. **(ii-iv)** Key genes (ASCL1, NEUROD1, YAP1) associated with different SCLC states are selected for the simplified network. Different cutoffs represent varying numbers of intermediate nodes within the arrows of the network. A cutoff of 2 is chosen as the minimal network capable of forming multiple steady states using only the key SCLC genes. **(v)** A subnetwork derived from the cutoff = 2 network, selected for further analysis. **C.** The bifurcation diagram illustrates the formation of multiple SCLC subtypes, with coexistence and transitions driven by changes in signaling which isn't defined. **D.** Heatmaps of the 20 most frequent numerical states from 60,000 random parameter sets calculating by Random-Genetic algorithm. The heatmap is a binary representation of the normalized levels of each gene across different states. The thresholds are 0.25 for nodes (0-1) and 2.5 for the signal MYC (0-10). The bar plot on the right indicates that single steady states occur more frequently than multi-steady states. With a 20% chance of transitioning from 2-steady states to 3-steady states due to small perturbations in parameters. *Labels the general observations of SCLC subtypes.

to the feedback loops between ASCL1 and NEUROD1, selecting a sub-network from it for analysis (**Fig. 18B(v)**).

Simplified Network Reveals SCLC States

An example of a bistability bifurcation diagram in response to increasing MYC-NOTCH signaling is presented in **Fig. 18C**. In this diagram, the blue line represents the normalized concentration of ASCL1, while the green line represents the normalized concentration of NEUROD1. The solid lines indicate steady states. The diagram illustrates three stages with four distinct cell states, denoted by grey arrows. Different colors correspond to specific cell states, labeled as Xi, Xj, Xk, and Xz, with their respective colors indicated by circles in the bifurcation diagram.

To analyze the parameter space regarding the overall distribution of states, heatmaps were generated for the 20 most frequent numerical states derived from 60,000 random parameter sets calculated using a Random-Genetic algorithm with signal MYC as the x axis of the bifurcation diagram (Materials and Methods). A bifurcation diagram and a fitness score were computed for each parameter set at generation 0. The algorithm then advanced these parameter sets to higher generations, such as generation 1 and 2, introducing mutations
to the parameter values in search of daughter parameter sets that exhibit greater coexistence states, provided their fitness scores are greater than or equal to 2 relatives to the original parameter set.

The top heatmap presents a binary representation of the normalized levels of each gene in the subnetwork across different states (**Fig. 18D**), revealing that eight states have a frequency exceeding 5%, with four of them marked with an asterisk (*) as fitting normal observations in SCLC. The bottom heatmap illustrates the frequency of states across varying numbers of

coexisting steady states. The bar plot on the left indicates that single steady states occur more frequently than multi-steady states. Notably, no three-steady-state multistability was observed in generation 0; however, there is a 20% chance of transitioning from two-steady states to three-steady states due to small perturbations in the parameters.

Gene Expression Levels Across Subtypes: ASCL1 Bistable States

To fit the simplified network from **Fig. 18B(v)** to specific time series scRNA data from RPM mice[18], we expanded the network by incorporating EMT and SCLC nodes, including CDH1, VIM, and REST, based on the cutoff=2 simplified network (**Fig. 19A(i)**). Differential expression analysis revealed significant variations among subtypes: ASCL1 exhibited the highest expression in A2, a medium level in A/N, and the lowest in Y subtypes. A/N also showed the highest MYC levels, while YAP1, HES1, and REST were most highly expressed in the Y subtype. For EMT nodes, CDH1 had the lowest expression in Y, second lowest in A/N, and the highest in A2. In contrast, the mesenchymal genes ZEB1 and VIM were elevated in A/N and Y subtypes but low in A2, indicating the role of EMT in SCLC progression. Blank spaces in **Fig. 19A(ii)** denote no significant differences in gene levels between the two target genes. Changes in gene levels across different time points and subtypes are illustrated in **Fig. 19A(iii)**.

The percentage of cell numbers for each subtype at each time point demonstrates that different SCLC subtypes can coexist on the same day, illustrating the evolution from neuroendocrine (NE) to non-NE states from day 4 to day 21 (**Fig. 19B(i)**). ASCL1 expression across subtypes reveals a significant difference between A2 and A/N. Additionally, the group of cells with above-mean ASCL1 levels in the A/N subtype significantly differs from A2, with a p-value of 7e-26. This, combined with the coexistence of A2 and A/N on days 4 and 7, indicates the presence of bistable states for ASCL1.

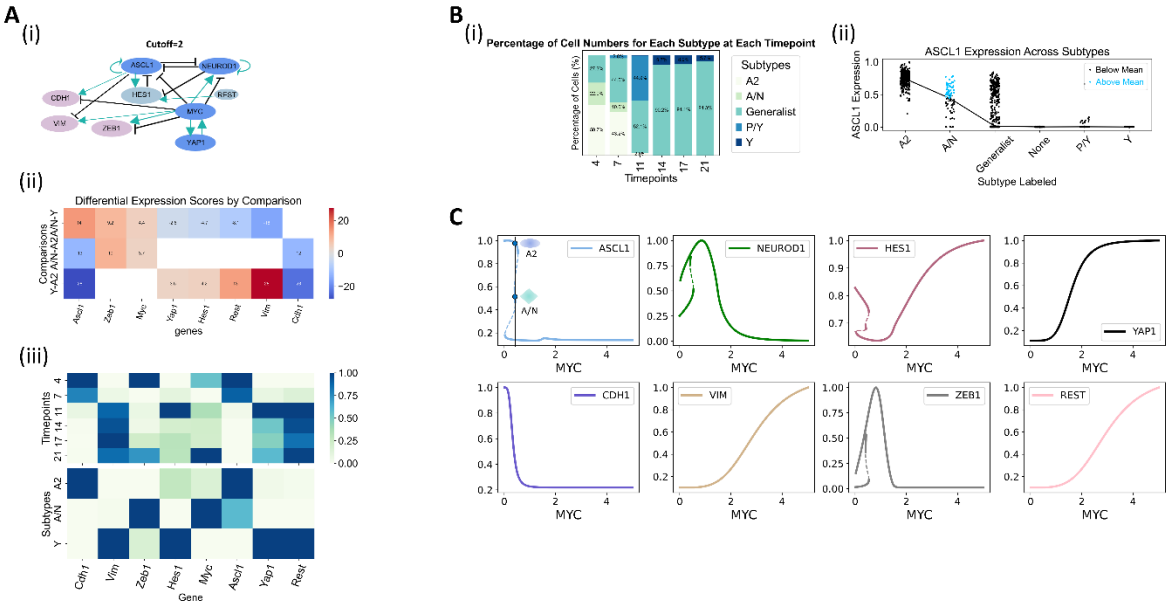

Fig. 3

Figure 19. A simple network captured gene expression levels across different subtypes, including the coexistence of two different ASCL1 levels in the A2 and A/N subtypes, and the NE-to-non-NE transition in the RPM mice data. A. (i) The simple network based on the ASCL1-NEUROD1 feedback loop in Fig2 includes ASCL1, NEUROD1, ZEB1, YAP1, HES1, REST, VIM, and CDH1. (ii) The genes, as nodes in the network, show significant differential expression among different subtypes through differential expression analysis. The blank spaces indicate no significant difference in gene levels when comparing the two target genes. (iii) The gene levels change across different time points and subtypes. **B. (i)** Percentage of cell numbers for each subtype for each timepoint. **(ii)** ASCL1 expression across different subtypes shows a significant difference between A2 and A/N in this subfigure and in Figure 3A(ii). Furthermore, the group of cells with above-mean ASCL1 levels in the A/N subtype is significantly different from A2, with a p-value of 7e-26, indicating the existence of bistable states of ASCL1. **C.** The bifurcation diagram identified by random-genetic algorithms, using a fitness function defined by the features of the RPM mice data, captures the gene expressions and dynamics of the RPM mice data and shows the coexistence of three states within the same environment, consistent with the RPM data. The two deep blue dots indicate the coexistence of the A2 and A/N subtypes.

Materials and methods

Gene Data Collection and Network Construction

Small Cell Lung Cancer (SCLC) and epithelial-to-mesenchymal transition (EMT) genes were chosen based on their differential expression profiles among different SCLC subtypes [4,22]. Transcriptional regulatory relationships were obtained from the TRRUST database[23]. The curated gene sets were analyzed for their roles in regulatory networks, and the gene interaction network was constructed and visualized using the NetworkX library. The simplified networks were generated by merging nodes into activation or repression pathways, with the cutoff number indicating the number of intermediate nodes that merged.

Mathematical Modeling

We used ordinary differential equations (ODE) to model the dynamics of the simplified network (**Fig.18B(v)**). Numerical bifurcation analysis was performed using roadrunner []. The kinetics of the varies genes in **Fig.18B(v)** are described by the differential equations

$$\frac{dA}{dt} = k_{0A} + K_A \frac{(\frac{A}{K_{AA}})^{n_{AA}}}{1+(\frac{A}{K_{AA}})^{n_{AA}}} \left(\frac{1}{1+(\frac{N}{K_{NA}})^{n_{NA}}} + \frac{1}{1+(\frac{S1}{K_{S1A}})^{n_{S1A}}} + \frac{1}{1+(\frac{H}{K_{HA}})^{n_{HA}}} \right) - r_{dA}A \quad (1)$$

$$\frac{dN}{dt} = k_{0N} + K_N \left(\frac{(\frac{N}{K_{NN}})^{n_{NN}}}{1+(\frac{N}{K_{NN}})^{n_{NN}}} + \frac{(\frac{S1}{K_{S1N}})^{n_{S1N}}}{1+(\frac{S1}{K_{S1N}})^{n_{S1N}}} \right) \left(\frac{1}{1+(\frac{A}{K_{AN}})^{n_{AN}}} + \frac{1}{1+(\frac{S1}{K_{S1\_N}})^{n_{S1\_N}}} \right) - r_{dN}N \quad (2)$$

$$\frac{dY}{dt} = k_{0Y} + K_Y \frac{(\frac{S1}{K_{S1Y}})^{n_{S1Y}}}{1+(\frac{S1}{K_{S1Y}})^{n_{S1Y}}} - r_{dY}Y \quad (3)$$

$$\frac{dZ}{dt} = k_{0Z} + K_Z \frac{(\frac{S1}{K_{S1Z}})^{n_{S1Z}}}{(1+(\frac{S1}{K_{S1Z}})^{n_{S1Z}})(1+(\frac{S1}{K_{S1\_Z}})^{n_{S1\_Z}})} - r_{dZ}Z \quad (4)$$

$$\frac{dH}{dt} = k_{0H} + K_H \frac{(\frac{A}{K_{AH}})^{n_{AH}}}{(1+(\frac{A}{K_{AH}})^{n_{AH}})(1+(\frac{N}{K_{NH}})^{n_{NH}})} - r_{dH}H \quad (5)$$

Table S3. Parameter values of SCLC.

Parameter	Description	Unit	Range
k_{0A}	Basal production rate of ASCL1	a.u./min	(0,1)
K_A	Dependent production rate constant of ASCL1		(0,6)
K_{AA}	Threshold of ASCL1 self-production	a.u.	(0,6)
n_{AA}	Cooperativity of ASCL1 self-production		(0,7)
K_{NA}	Threshold of ASCL1 by NEUROD1	a.u.	(0,6)
n_{NA}	Cooperativity of ASCL1 by NEUROD1		
S1	Concentration of MYC1	a.u.	(0,10)
K_{S1A}	Threshold of ASCL1 by MYC	a.u.	(0,6)
n_{S1A}	Cooperativity of ASCL1 by MYC		(0,7)
K_{HA}	Threshold of ASCL1 by HES1	a.u.	(0,6)
n_{HA}	Cooperativity of ASCL1 by HES1		(0,7)
r_{dA}	Degradation rate constant of ASCL1	/min	(0,6)
k_{0N}	Basal production rate of NEUROD1	a.u./min	(0,1)
K_N	Dependent production rate constant of NEUROD1		(0,6)
K_{NN}	Threshold of NEUROD1 self-production	a.u.	(0,6)
n_{NN}	Cooperativity of NEUROD1 self-production		(0,7)
K_{S1N}	Activation threshold of NEUROD1 by MYC	a.u.	(0,6)
n_{S1N}	Activation cooperativity of NEUROD1 by MYC		(0,7)
K_{AN}	Threshold of NEUROD1 by ASCL1	a.u.	(0,6)
n_{AN}	Cooperativity of NEUROD1 by ASCL1		(0,7)
K_{S1_N}	Repression threshold of NEUROD1 by MYC	a.u.	(0,6)
n_{S1_N}	Repression cooperativity of NEUROD1 by MYC		(0,7)
r_{dN}	Degradation rate constant of NEUROD1	/min	(0,6)
k_{0Y}	Basal production rate of YAP1	a.u./min	(0,1)
K_Y	Dependent production rate constant of YAP1		(0,6)
K_{S1Y}	Threshold of YAP1 by MYC	a.u.	(0,6)
n_{S1Y}	Cooperativity of YAP1 by MYC		(0,7)
r_{dY}	Degradation rate constant of YAP1	/min	(0,6)
k_{0Z}	Basal production rate of ZEB1	a.u./min	(0,1)
K_Z	Dependent production rate constant of ZEB1		(0,6)
K_{S1Z}	Activation threshold of ZEB1 by MYC	a.u.	(0,6)
n_{S1Z}	Activation cooperativity of ZEB1 by MYC		(0,7)
K_{S1_Z}	Repression threshold of ZEB1 by MYC	a.u.	(0,6)
n_{S1_Z}	Repression cooperativity of ZEB1 by MYC		(0,7)
r_{dZ}	Degradation rate constant of ZEB1	/min	(0,6)
k_{0H}	Basal production rate of HES1	a.u./min	(0,1)
K_H	Dependent production rate constant of HES1		(0,6)
K_{AH}	Threshold of HES1 by ASCL1	a.u.	(0,6)
n_{AH}	Cooperativity of HES1 by ASCL1		(0,7)
K_{NH}	Threshold of HES1 by NEUROD1	a.u.	(0,6)
n_{NH}	Cooperativity of HES1 by NEUROD1		(0,7)
r_{dH}	Degradation rate constant of HES1	/min	(0,6)

* a.u. is an arbitrary unit of concentration.

Here, MYC is set as a signal (S1) to simplify the network.

Random-Genetic Algorithm

This algorithm, used for numerical simulation, is divided into two parts. The first part involves performing numerical bifurcation analysis with a signal as the x-axis for each random parameter set; here, MYC is selected as an example, this step filters out parameter sets where the MYC signal, or another signal, does not affect the dynamics of other nodes in the network, reflecting unrealistic biological scenarios. Fitness scores are assigned to each parameter set based on the number of multi-steady states. Nodes are assigned on (1) or off (-1) states, forming a state vector (a, n, h, y, z, m), with each letter of the network representing a 1 or -1 value. A binary heatmap was produced by generating 60,000 random parameter sets, each potentially resulting in multiple node state configurations.

The second part uses a genetic algorithm with two aims. The first is to search for multiple steady states, specifically identifying whether three or more steady states exist in the network. A fitness score is assigned to each random parameter set based on the coexistence number calculated by the fitness function. If the fitness score exceeds 1, a group of offspring (e.g., offspring = 200) is generated by applying a mutation function, which introduces small random changes to the parameters. The fitness function is then applied to each offspring, and the process is repeated to search for coexisting states. The second aim is to find parameter sets that fit specific data features. Using RPM mice data [], the algorithm inputs the features into the fitness function and searches for parameter sets that best fit the biological features (**Fig. 19C**).

Single Cell RNA Sequence Analysis

Single-cell RNA sequencing data from GSE149180 (RPM mouse tumor time course), which includes four subtypes: A2, A/N, Y, and P[18]. We focused on the first three subtypes. The analysis, performed in Python, included differential expression scores by comparing A2-Y, A2-A/N, and

Y-A/N, heatmaps showing gene expression levels across different time points and subtypes, coexistence of various SCLC subtypes at the same time points, and details of gene expression patterns across subtypes.

Discussion

A simple network can capture the four subtypes of small cell lung cancer

Understanding the formation of subtypes in small cell lung cancer (SCLC) is critical for advancing both diagnostic and therapeutic strategies. The biological heterogeneity within SCLC complicates treatment and impacts patient prognosis, making it essential to identify and characterize the mechanisms driving subtype formation[25,26]. By explaining how these subtypes emerge and persist, we can improve personalized treatment approaches and ultimately enhance outcomes in SCLC management. Research into the formation of these subtypes has the potential to uncover key regulatory pathways and targetable vulnerabilities[27]. Several existing models have aimed to simulate the emergence of SCLC subtypes[4,28]. While effective in capturing complex biological interactions, many of these models rely on intricate and highly detailed networks that are difficult to interpret and utilize in clinical or experimental settings. The complexity of these networks can limit their accessibility and hinder their broader application for predictive or therapeutic purposes. Simplifying such models without compromising accuracy is a necessary step toward more practical solutions.

In our work, we have developed a streamlined mathematical model that distills the underlying regulatory network into several core nodes. Despite this simplification, the model accurately captures the formation and maintenance of various SCLC subtypes, including ASCL1-high, NEUROD1-low, YAP1-low; ASCL1-low, NEUROD1-high, YAP1-high; ASCL1-low, NEUROD1-low, YAP1-high; and ASCL1-high, NEUROD1-high, YAP1-low[4,29]. This reduced

complexity makes our model more intuitive and easier to apply, while still preserving the essential dynamics of the system. Our approach demonstrates that it is possible to capture the key aspects of SCLC subtype formation through a more accessible framework, offering a balance between precision and usability for future research and clinical translation.

While the model successfully captures the levels of ASCL1, NEUROD1, and YAP1, there are still issues concerning the levels of ZEB1 and HES1 in the current model. Specifically, HES1 and ZEB1 remain persistently active in the most frequent cell states, which is inconsistent with biological observations. This could be due to the threshold settings or the inefficiency of the regulatory signaling pathways in the selected simplified network. It is possible that some critical signaling pathways related to these two genes are missing. Therefore, it is essential to explore alternative simplified networks, as indicated in **Fig. 18B(iv)**, and to summarize the key network structures that can effectively capture these subtypes in future work.

Model predicts multiple steady states in small cell lung cancer

In many biological systems, the presence of multiple steady states is linked to regulatory networks with feedback loops, where the system can settle into different stable configurations depending on initial conditions or external signals[30-33]. This phenomenon, known as multi-stability, is frequently observed in systems involving cell differentiation, gene expression, and signal transduction pathways[34-37].

In our model, the negative feedback loop between ASCL1 and NEUROD1 is capable of producing multiple steady states, a fundamental property of nonlinear systems governed by ordinary differential equations (ODEs)[38,39]. These steady states suggest the co-existence of multiple levels of core genes across different SCLC subtypes, and the model's predicted bistable

states of ASCL1 levels align with RPM mice data, indicating that A2 and A/N subtypes can coexist at the same time points within the same microenvironment[18].

While MYC signaling is important in SCLC, genes such as NOTCH, BCL2, REST, and FGFR1 also play significant roles in this system[40-45]. Our model framework and random-genetic algorithm are flexible, allowing construct simplified networks that incorporate these genes, clarifying the key regulatory pathways and structures surrounding them within the SCLC system.

Acknowledgements

Ziyi Liu: Conceptualization, Formal analysis, Methodology, Software, Investigation, Validation, Visualization, Writing - original draft

Darren R. Tyson: Conceptualization

Tian Hong: Conceptualization, Funding acquisition

Declaration of Interests

The authors declare no competing or financial interests.

References

1 Howlader, N. *et al.* SEER cancer statistics review, 1975–2012. *National Cancer InstituteFrontiers in Oncology* (2014).

2 Schwendenwein, A. *et al.* Molecular profiles of small cell lung cancer subtypes: Therapeutic implications. *Molecular Therapy - Oncolytics* **20**, 470-483 (2021). https://doi.org/10.1016/j.omto.2021.02.004

3 Rudin, C. M. *et al.* Molecular subtypes of small cell lung cancer: a synthesis of human and mouse model data. *Nat Rev Cancer* **19**, 289-297 (2019). https://doi.org/10.1038/s41568-019-0133-9

4 Wooten, D. J. *et al.* Systems-level network modeling of Small Cell Lung Cancer subtypes identifies master regulators and destabilizers. *PLoS Comput Biol* **15**, e1007343 (2019). https://doi.org/10.1371/journal.pcbi.1007343

5 Gazdar, A. F., Bunn, P. A. & Minna, J. D. Small-cell lung cancer: what we know, what we need to know and the path forward. *Nature Reviews Cancer* **17**, 725–737 (2017). https://doi.org/https://doi.org/10.1038/nrc.2017.87

6 Zugazagoitia, J. & Paz-Ares, L. Extensive-Stage Small-Cell Lung Cancer: First-Line and Second-Line Treatment Options. *J Clin Oncol* **40**, 671-680 (2022). https://doi.org/10.1200/JCO.21.01881

7 Sato, Y. *et al.* Paraneoplastic neurological syndrome and its impact on the treatment outcomes of small-cell lung cancer: A single-center retrospective analysis. *Thorac Cancer* (2024). https://doi.org/10.1111/1759-7714.15472

8 van Meerbeeck, J. P., Fennell, D. A. & De Ruysscher, D. K. Small-cell lung cancer. *Lancet* **378**, 1741-1755 (2011). https://doi.org/10.1016/S0140-6736(11)60165-7

9 Institute, U. S. N. C. *Small cell carcinoma of the Lung and Bronchus: Surveillance, Epidemiology, and End Results (SEER) Relative Survival Rates by Time Since Diagnosis*, <https://seer.cancer.gov> (2016).

10 Semenova, E. A., Nagel, R. & Berns, A. Origins, genetic landscape, and emerging therapies of small cell lung cancer. *Genes Dev* **29**, 1447-1462 (2015). https://doi.org/10.1101/gad.263145.115

11 Peifer, M. *et al.* Integrative genome analyses identify key somatic driver mutations of small-cell lung cancer. *Nat Genet* **44**, 1104-1110 (2012). https://doi.org/10.1038/ng.2396

12 Arriola, E. *et al.* Genetic changes in small cell lung carcinoma. *Clin Transl Oncol* **10**, 189-197 (2008). https://doi.org/10.1007/s12094-008-0181-1

13 George, J. *et al.* Evolutionary trajectories of small cell lung cancer under therapy. *Nature* **627**, 880-889 (2024). https://doi.org/10.1038/s41586-024-07177-7

14 Madden, S. K., de Araujo, A. D., Gerhardt, M., Fairlie, D. P. & Mason, J. M. Taking the Myc out of cancer: toward therapeutic strategies to directly inhibit c-Myc. *Mol Cancer* **20**, 3 (2021). https://doi.org/10.1186/s12943-020-01291-6

15 Dhanasekaran, R. *et al.* The MYC oncogene - the grand orchestrator of cancer growth and immune evasion. *Nat Rev Clin Oncol* **19**, 23-36 (2022). https://doi.org/10.1038/s41571-021-00549-2

16 George, J. *et al.* Comprehensive genomic profiles of small cell lung cancer. *Nature* **524**, 47-53 (2015). https://doi.org/10.1038/nature14664

17 Borromeo, M. D. *et al.* ASCL1 and NEUROD1 Reveal Heterogeneity in Pulmonary Neuroendocrine Tumors and Regulate Distinct Genetic Programs. *Cell Rep* **16**, 1259-1272 (2016). https://doi.org/10.1016/j.celrep.2016.06.081

18 Ireland, A. S. *et al.* MYC Drives Temporal Evolution of Small Cell Lung Cancer Subtypes by Reprogramming Neuroendocrine Fate. *Cancer Cell* **38**, 60-78 e12 (2020). https://doi.org/10.1016/j.ccell.2020.05.001

19 Khan, P. *et al.* Epigenetic landscape of small cell lung cancer: small image of a giant recalcitrant disease. *Semin Cancer Biol* **83**, 57-76 (2022). https://doi.org/10.1016/j.semcancer.2020.11.006

20 Rudin, C. M., Brambilla, E., Faivre-Finn, C. & Sage, J. Small-cell lung cancer. *Nat Rev Dis Primers* **7**, 3 (2021). https://doi.org/10.1038/s41572-020-00235-0

21 Gay, C. M. *et al.* Patterns of transcription factor programs and immune pathway activation define four major subtypes of SCLC with distinct therapeutic vulnerabilities. *Cancer Cell* **39**, 346-360 e347 (2021). https://doi.org/10.1016/j.ccell.2020.12.014

22 Groves, S. M. *et al.* Involvement of Epithelial-Mesenchymal Transition Genes in Small Cell Lung Cancer Phenotypic Plasticity. *Cancers (Basel)* **15** (2023). https://doi.org/10.3390/cancers15051477

23 Han, H. *et al.* TRRUST: a reference database of human transcriptional regulatory interactions. *Sci Rep* **5**, 11432 (2015). https://doi.org/10.1038/srep11432

24 Hagberg, A. & Conway, D. Networkx: Network analysis with python. (2020).

25 Jin, Y. *et al.* Understanding SCLC heterogeneity and plasticity in cancer metastasis and chemotherapy resistance. *Acta Biochim Biophys Sin (Shanghai)* **55**, 948-955 (2023). https://doi.org/10.3724/abbs.2023080

26 Megyesfalvi, Z. *et al.* Clinical insights into small cell lung cancer: Tumor heterogeneity, diagnosis, therapy, and future directions. *CA: A Cancer Journal for Clinicians* **73**, 620-652 (2023). https://doi.org/https://doi.org/10.3322/caac.21785

27 Wang, W. Z., Shulman, A., Amann, J. M., Carbone, D. P. & Tsichlis, P. N. Small cell lung cancer: Subtypes and therapeutic implications. *Semin Cancer Biol* **86**, 543-554 (2022). https://doi.org/10.1016/j.semcancer.2022.04.001

28 Chauhan, L., Ram, U., Hari, K. & Jolly, M. K. Topological signatures in regulatory network enable phenotypic heterogeneity in small cell lung cancer. *Elife* **10** (2021). https://doi.org/10.7554/eLife.64522

29 Udyavar, A. R. *et al.* Novel Hybrid Phenotype Revealed in Small Cell Lung Cancer by a Transcription Factor Network Model That Can Explain Tumor Heterogeneity. *Cancer Res* **77**, 1063-1074 (2017). https://doi.org/10.1158/0008-5472.CAN-16-1467

30 Smith, H. Oscillations and multiple steady states in a cyclic gene model with repression. *J Math Biol* **25**, 169-190 (1987). https://doi.org/10.1007/BF00276388

31 Fridlyand, L. E. & Phillipson, L. H. Mechanisms of glucose sensing in the pancreatic beta-cell: A computational systems-based analysis. *Islets* **3**, 224-230 (2011). https://doi.org/10.4161/isl.3.5.16409

32 Laurent, M. & Kellershohn, N. Multistability: a major means of differentiation and evolution in biological systems. *Trends Biochem Sci* **24**, 418-422 (1999). https://doi.org/10.1016/s0968-0004(99)01473-5

33 Europa, A. F., Gambhir, A., Fu, P. C. & Hu, W. S. Multiple steady states with distinct cellular metabolism in continuous culture of mammalian cells. *Biotechnol Bioeng* **67**, 25-34 (2000). https://doi.org/10.1002/(sici)1097-0290(20000105)67:1<25::aid-bit4>3.0.co;2-k

34 Huang, S. Reprogramming cell fates: reconciling rarity with robustness. *Bioessays* **31**, 546-560 (2009). https://doi.org/10.1002/bies.200800189

35 Tsuchiya, M., Giuliani, A. & Brazhnik, P. From Cell States to Cell Fates: Control of Cell State Transitions. *Methods Mol Biol* **2745**, 137-162 (2024). https://doi.org/10.1007/978-1-0716-3577-3_9

36 Enver, T., Pera, M., Peterson, C. & Andrews, P. W. Stem cell states, fates, and the rules of attraction. *Cell Stem Cell* **4**, 387-397 (2009). https://doi.org/10.1016/j.stem.2009.04.011

37 Li, C. J. *et al.* MicroRNA governs bistable cell differentiation and lineage segregation via a noncanonical feedback. *Mol Syst Biol* **17**, e9945 (2021). https://doi.org/10.15252/msb.20209945

38 Ye, Y., Kang, X., Bailey, J., Li, C. & Hong, T. An enriched network motif family regulates multistep cell fate transitions with restricted reversibility. *PLoS Comput Biol* **15**, e1006855 (2019). https://doi.org/10.1371/journal.pcbi.1006855

39 Brackston, R. D., Lakatos, E. & Stumpf, M. P. H. Transition state characteristics during cell differentiation. *PLoS Comput Biol* **14**, e1006405 (2018). https://doi.org/10.1371/journal.pcbi.1006405

40 Lim, J. S. *et al.* Intratumoural heterogeneity generated by Notch signalling promotes small-cell lung cancer. *Nature* **545**, 360-364 (2017). https://doi.org/10.1038/nature22323

41 Li, W. *et al.* Characteristics of Notch signaling pathway and its correlation with immune microenvironment in SCLC. *Lung Cancer* **167**, 25-33 (2022). https://doi.org/10.1016/j.lungcan.2022.03.019

42 Ikegaki, N., Katsumata, M., Minna, J. & Tsujimoto, Y. Expression of bcl-2 in small cell lung carcinoma cells. *Cancer Res* **54**, 6-8 (1994).

43 Kreisler, A. *et al.* Regulation of the NRSF/REST gene by methylation and CREB affects the cellular phenotype of small-cell lung cancer. *Oncogene* **29**, 5828-5838 (2010). https://doi.org/10.1038/onc.2010.321

44 Redin, E. *et al.* SMARCA4 controls state plasticity in small cell lung cancer through regulation of neuroendocrine transcription factors and REST splicing. *J Hematol Oncol* **17**, 58 (2024). https://doi.org/10.1186/s13045-024-01572-3

45 Ferone, G. *et al.* FGFR1 Oncogenic Activation Reveals an Alternative Cell of Origin of SCLC in Rb1/p53 Mice. *Cell Rep* **30**, 3837-3850 e3833 (2020). https://doi.org/10.1016/j.celrep.2020.02.052

CONCLUSION

This dissertation explores how complex cellular behaviors and organismal functions arise from regulatory networks. To address this, we developed mathematical models for three biological systems, each showing distinct regulatory challenge. In Chapter II, we modeled the shoot apical meristem (SAM) in plants, revealing mechanisms that maintain stem cell homeostasis. Chapter III investigates cell polarity in fission yeast, highlighting feedback loops in Cdc42 regulation and its link with actin-mediated endocytosis. In Chapter IV, we modeled subtype formation in Small Cell Lung Cancer (SCLC), capturing tumor heterogeneity through key transcription factors. These studies demonstrate how regulatory networks drive complex biological processes across different systems.

We developed a multicellular model to understand the regulatory network controlling the shoot apical meristem (SAM) patterning in plants (Chapter II), focusing on two-axis control of WUS expression through signals from both the middle and peripheral SAM regions. Our model demonstrated how peripheral signals, like EPFL, interact with central signals, such as CLV3, to maintain WUS localization within the organizing center, ensuring stable stem cell maintenance. This approach revealed the importance of paradoxical feedback loops between WUS and CLV3, which contribute to both stable expression and spatial organization of distinct cell types within the SAM. Additionally, we identified tradeoffs in the regulatory network, suggesting evolutionary pressures that balance multiple patterning features essential for robust SAM function. Although simplified, our model provides critical insights into the SAM regulatory network's spatial and temporal dynamics and lays the groundwork for more complex models that incorporate growth and three-dimensional structure to better reflect real SAM behavior.

To elucidate the dynamics of Cdc42 regulation in *Schizosaccharomyces pombe* (Chapter III), we developed a PDE model focused on the role of feedback loops in maintaining cell polarity and oscillatory activation at each cell end. Our model demonstrated that at least one intermediate node is involved in the negative regulation of active Cdc42 and that actin-mediated endocytosis is essential for periodic reactivation of Cdc42, as shown by experimental data. This process removes the inhibitory effect of Pak1, allowing the recruitment of Cdc42 activators such as Scd1. These findings reveal that inhibiting endocytosis leads to Pak1 accumulation, which disrupts Cdc42 dynamics and results in monopolar growth. Combining the analysis of experimental data from both Pak1 mutants and CK-666 conditions, our model predicted that additional molecules, beyond Pak1, likely play a role in the negative regulation of active Cdc42. Interestingly, the model predicts phase shifts between Cdc42 and Pak1, highlighting a temporal delay in Pak1's inhibitory feedback and underscoring the complexity of self-organizing processes in cell polarity. While this model captures the spatiotemporal regulation of Cdc42, it provides a foundation for future studies to explore additional regulatory elements that may influence cell polarity and bipolar growth under varied physiological conditions.

To understand the formation of subtypes in small cell lung cancer (SCLC) (Chapter IV), we simplified the SCLC regulatory network and developed mathematical models to capture the formation and persistence of distinct subtypes, focusing on core regulatory nodes such as MYC, ASCL1, NEUROD1, and YAP1. This streamlined network successfully represents the four main SCLC subtypes, providing a practical framework that balances accuracy with accessibility. While the model captures essential subtype dynamics, it shows inconsistencies with the levels of HES1 and ZEB1, suggesting that additional regulatory pathways might be needed to refine subtype representation. The model also predicts multiple steady states, aligning with the phenomenon of

multi-stability observed in SCLC subtypes A/N and A2 in RPM mice scRNA data, where ASCL1 and NEUROD1 feedback loops create bistable states. These findings illustrate the potential of simplified networks to uncover critical regulatory pathways in SCLC, and our approach could be extended to incorporate other key genes, like NOTCH and REST, for a more comprehensive understanding of SCLC heterogeneity and progression.

VITA

Ziyi Liu was born in Xiaobo, Hunan Province, near the Dongting Lake, an area rich with ponds and rivers. She received her Bachelor of Science in Condensed Matter Physics from the Southern University of Science and Technology in 2019. She then pursued her doctoral studies at the University of Tennessee, Knoxville, where she earned her PhD in Genome Science and Technology (GST) under the advisement of Dr. Tian Hong in 2024.

In high school, Ziyi developed a love for literature and manga, started capturing and recording her dreams. In college, she began illustrating memories of her dreams but found it wasn't enough to satisfy her curiosity about the 'seeing' colors, shapes, 'hearing' sounds, 'feeling' emotions in dreams, and the mechanisms behind memory formation and recall. This curiosity led her to explore some neuroscience, which ultimately inspired her shift to the biological sciences for her PhD. While her current research doesn't directly involve studies on the brain and memory, the researches and questions on cancer, plants, and yeast remains fascinating.